UNIVERSITY OF CALIFORNIA
RIVERSIDE

Global Ocean Circulation Changes and Ocean Heat Uptake in a Warming Climate

A Dissertation submitted in partial satisfaction
of the requirement for the degree of

Doctor of Philosophy

in

Earth and Planetary Sciences

by

Shouwei Li

June 2023

Dissertation Committee:

Dr. Wei Liu, Chairperson
Dr. Robert J. Allen
Dr. Richard A. Minnich

The Dissertation of Shouwei Li is approved:

_____

_____

_____

Committee Chairperson

University of California, Riverside

ACKNOWLEDGEMENTS

First of all, I want to express my sincere appreciation to the consistent guidance and mentorship from my advisor Dr. Wei Liu. Thanks for his great suggestion on my research and the advice and resources in support of my academic goals and ambitions. The wonderful academic environment he creates enables me to finish this work and grow up as a researcher. I am really proud to be a part of his group at UC Riverside.

I also would like to thank my committee member, Dr. Robert J. Allen, who is also my graduate advisor and collaborator. Dr Allen is always available for a discussion not only about my research but also other questions I have as a graduate student. Thanks to his timely feedback and invaluable time. Meanwhile, I would like to thank my other committee member, Dr Richard A. Minnich, for his insightful advice and feedback on this dissertation and being patient in helping me with writing.

I also wish to thank Xianglin Ren, Yu-Chi Lee, Antony Thomas and David Duarte in Wei's group, for their advice and help during the special time. Besides, I want to thank Xiaofan Ma and Changlin Chen, who are the visiting scholars in Wei's group. Thanks for their helpful suggestions within and out of academia when I was new as a Ph.D. student.

Lastly, I want to dedicate this dissertation to my mother, Geying Luo, and my father Jian Li. Thanks for bringing me to the world and being my harbor. And I hope I can make you proud of me.

Chapter 2 of this dissertation consists of a reprint of the material from the following publication: Li S, Liu W, Lyu K, Zhang X (2021) The effects of historical ozone changes on Southern Ocean heat uptake and storage. Clim. Dyn., 22, 1-7 and a part of the rewritten of the material from the following publication: Liu W, Hegglin MI, Checa-Garcia R, Li S, Gillett NP, Lyu K, Zhang X, Swart NC (2022) Stratospheric ozone depletion and tropospheric ozone increases drive Southern Ocean interior warming. Nat. Clim. Change, 12, 365–372.

Chapter 3 of this dissertation, in full, is a rewritten of the material from the in-revision publication: Li S, Liu W, Allen RJ, Shi JR, Li L (2023) Anthropogenic aerosol and greenhouse gas driven ocean heat uptake and redistribution (in revision).

Chapter 4 of this dissertation, in full, is a reprint of the material from the following publication: Li S, Liu W (2022) Impacts of Arctic sea ice loss on global ocean circulations and interbasin ocean heat exchanges. Clim. Dyn., 59, 2701–2716.

To my mother, Geying Luo, and my father, Jian Li.

ABSTRACT OF THE DISSERTATION

Global Ocean Circulation Changes and Ocean Heat Uptake in a Warming Climate

by

Shouwei Li

Doctor of Philosophy, Graduate Program in Earth and Planetary Sciences
University of California, Riverside, June 2023
Dr. Wei Liu, Chairperson

Oceans play a dominant role in modulating Earth's energy imbalance since the industrial age by absorbing and storing the excessive heat. In this dissertation, I utilize observation data sets and climate model simulations to investigate the global ocean circulation changes and ocean heat uptake (OHU) in a warming climate.

I first explore the effects of historical ozone changes on Southern Ocean heat uptake and storage. I find that ozone-induced interior warming contributes to about 22% of the historical Southern Ocean warming over 1958-2005, with heat is taken between 50-58°S but mainly stored at low latitudes due to ocean circulation anomaly induced equatorward heat redistribution. I then distinguish the different roles of troposphere ozone increases and stratosphere ozone depletion on OHU. I show that both ozone changes contribute to Southern Ocean interior warming but with distinct physical

mechanisms: the former causes a subsurface warming in the Southern Ocean primarily via the deepening of isopycnals, while the latter via spiciness changes along isopycnals.

Meanwhile, I also quantify the effects of anthropogenic aerosols and greenhouse gases in modulating oceanic heat since the industrial age. I show that, in response to anthropogenic aerosols, OHU diminishes in the subpolar Atlantic, and the Southern Ocean imports heat from the Indo-Pacific but exports heat into the Atlantic, which is comparable to OHU changes. Anthropogenic greenhouse gases, on the contrary, promote the OHU in the subpolar Atlantic and allow the Southern Ocean to import heat from the Atlantic but export heat to the Indo-Pacific. Nevertheless, interbasin heat exchange is far smaller than OHU changes.

Finally, I explore the effects of Arctic sea ice loss on global ocean circulations and ocean heat redistribution. I find that Arctic sea ice loss enhances OHU in the subpolar North Atlantic while changes in ocean heat storage is timescale-dependent. Within a decade, the Atlantic meridional overturning circulation (AMOC) is little altered such that most of the taken heat is locally stored in the Atlantic. On a multidecadal to centennial timescale, the AMOC decelerates the redistribution of heat to other basins through interbasin ocean heat exchanges, and therefore leads to global ocean warming.

Contents

List of Figures

List of Tables

Chapter 1

Introduction

With a high heat capacity and majority covering of the earth's surface, oceans play an essential role in the earth's climate system. According to the Fifth Assessment Report of the Intergovernmental Panel on Climate Change (IPCC), more than 90% of GHGs induced energy imbalance is absorbed by the ocean over recent decades (Rhein et al. 2013), prescribing as the form of enhanced surface heat fluxes as well as ocean heat uptake. Therefore, exploring the changes in OHU and ocean circulations is of vital importance in understanding climate change in the past and making reliable predictions for the future.

The Southern Ocean exhibits the strongest OHU increase among global oceans during the past few decades [Sen Gupta et al. (2009); Frölicher et al. (2015)], along with a rapid subsurface warming and a large ocean heat content increase [Gille (2002); Cai et al. 2010]. Multiple previous studies have been

adopted to understand the mechanism of Southern Ocean warming in which greenhouse gases (GHGs) has been suggested as the dominant forcing. For instance, an early study notice that the latitudes where the heat enters the ocean are different from the heat storage (Manabe et al. 1991), highlighting the importance of meridional ocean heat transport which is determined by both the Eulerian mean circulation and eddies [Gregory (2000); Griffies et al. (2015)]. Later studies further suggest that, enhanced Eulerian mean heat transport [Kuhlbrodt and Gregory (2012); Marshall et al. (2014)], weakened eddy-induced heat transport (Morrison et al. 2013), or the amplification of the two processes (Morrison et al. 2016) can act to modify the heat redistribution and consequently the storage within the Southern Ocean in a warming climate with GHGs increase. Besides, by adopting a simple model, Church et al. (1991) suggests that heat penetrates into the Southern Ocean mostly due to subduction along constant density surfaces and in a way similar to a passive tracer, which is also supported by Gregory et al. (2016) and Garuba and Klinger (2016). However, other studies argue that the ocean heat uptake can vary significantly with changes in the ocean circulation and therefore cannot be viewed solely as a passive process. Recently, by decomposing the effects of directing warming and wind changes under increased atmospheric CO_2 concentrations, Liu et al. (2018) shows that, the latter could explain about 20% of the ocean heat storage maximum in the Southern Ocean, indicative of the

important role of wind changes in Southern Ocean heat uptake, redistribution and storage.

Besides the GHGs increase, ozone changes are suggested to be another important forcing agent in driving the Southern Hemisphere climate change. Nevertheless, different from the GHGs, the effects of ozone forcing on altering the Southern Ocean heat anomaly are probably achieved by wind changes. For instance, in response to stratospheric ozone depletion, Southern Hemisphere westerly winds are poleward intensified as well as positive phase of SAM [Swart and Fyfe (2012); Marshall (2003)]. And ozone induced wind changes are even stronger than that due to GHGs (Polvani et al. 2011). Meanwhile, modified by the surface winds, the meridional overturning circulations show poleward intensification along with subsurface warming in the Southern Ocean interior due to ozone changes, which explains more than 30% of the historical warming (Solomon et al. 2015). However, it is still not clear the mechanism by which the ocean heat uptake, redistribution and storage are altered in response to stratospheric ozone depletion. Meanwhile, besides the depletion in the stratosphere, ozone concentrations also exhibit distinct changes in the troposphere with an increasing trend as a result of anthropogenic emissions of ozone precursors [e.g., Young et al. (2018); Stevenson et al. (2013)]. The climate impact of tropospheric ozone increases on Southern Ocean is also unclear. A detailed analysis of the effects and

mechanism of the ozone changes on Southern Ocean warming is discussed in Chapter 2.

Out of the Southern Ocean, the Atlantic plays the second role in absorbing the added heat with GHGs still dominating the OHU. However, different from that in the Southern Ocean where the effects of GHGs are amplified by the ozone changes, GHGs induced OHU increases are significantly compensated by aerosol-induced OHU decreases in the Atlantic [Ma et al. (2020); Shi et al. (2018)]. Changes in the AMOC play an essential role in this process. Specifically, GHGs increase weakens the AMOC, resulting in reduced northward ocean heat transport in the Atlantic basin along with SST cooling in the North Atlantic subpolar region [Shi et al. (2018); Liu et al. (2020)]. Therefore, the enhanced atmosphere-ocean surface temperature contrast will alter the turbulent feedback thus enhance the OHU there [Hausmann et al. (2016); Zhang and Cooke (2020)]. On the contrary, in response to aerosol changes, AMOC strength is enhanced since the 20th century compared with the preindustrial level, accompanied by strengthened northward ocean heat transport and SST warming over the North Atlantic subpolar region [Ma et al. (2020); Hassan et al. (2022)]. Therefore, aerosol changes act to weaken the OHU there which significantly compensate the GHG-induced OHU increase.

Besides the regional changes in the Atlantic basin, the AMOC can also play a role in modifying the ocean heat content in ocean basins via interbasin heat exchanges as a part of global conveyor belt (Garuba and Klinger 2016). Triggered by a perturbation in the North Atlantic Deep Water formation to decelerate the AMOC, the subsequent signals propagate in form of an equatorward Kelvin wave along the western boundary in the Atlantic [Kawase (1987); Johnson and Marshall (2002); Zhang (2010)], which further travel across the equator eastwardly and propagate poleward along the eastern boundary [e.g., Cessi et al. (2004); Huang et al. (2000); Sévellec and Fedorov (2013); Sun et al. (2020)]. At the basin boundary with the Southern Ocean, the Kelvin wave leads to abnormal meridional geostrophic transport with opposite signs in the Indo-Pacific and Atlantic Oceans by altering the zonal difference of interface depth, hence resulting in an abnormal northward ocean circulation (Sun et al. 2020). Also, the Indonesian Throughflow (ITF), which connects the Indian Ocean and Pacific in the tropics, also become weaker in response to AMOC weakening due to a decreased pressure gradient between the Indian Ocean and Pacific (Sun and Thompson 2020), which further adjusts the interbasin exchange between the Pacific and Indian Oceans [e.g., Hu and Sprintall (2017); Lee et al. (2015)]. In the Southern Hemisphere, an AMOC weakening can poleward shift the westerly winds and further alter the Deacon Cell in the Southern Ocean (Chen et al. 2019). As a result, it is necessary to

understand the effects of GHGs and aerosol on ocean heat anomaly based on a global scale, including both the regional ocean heat uptake and also the interbasin heat exchanges associated with ocean circulation changes. The mechanisms are investigated in Chapter 3.

Chapter 3 also highlights the teleconnection between Northern and Southern Hemisphere middle-high latitudes. In other words, the effects of forcing in the North Atlantic are not locally constrained but can lead to global climate change by modifying the AMOC strength. As an example, Arctic sea ice loss, which occurs in Northern Hemisphere polar region, can lead to rapid warming over the entire Northern Hemisphere high latitudes in a slab ocean model [Chiang and Bitz (2005); Deser et al. (2015)]. However, Arctic sea ice loss also acts to modify AMOC strength concurrently via both haline [Jungclaus et al. (2005); Sévellec and Fedorov (2015)] and thermal (Levermann et al. 2007) processes. Therefore, when ocean dynamics are considered, the effect of Arctic sea ice loss can extend to the tropics or even Antarctic, prompting a global warming except the low stratosphere in high latitudes in both hemispheres [Deser et al. (2015); Liu and Fedorov (2019)].

Nevertheless, the effects of Arctic sea ice loss on global ocean circulation and heat anomalies can not be well simulated by previous studies adopting GHGs warming or hosing experiments. On one hand, in GHGs warming experiment, changes in Arctic sea ice and the AMOC happen concurrently due

to GHGs increase such that it is hard to disentangle their effects on global ocean heat uptake and redistribution. More importantly, the effect of ocean circulation change on global ocean heat content anomalies could be overwhelmed by direct surface warming (Garuba and Klinger 2016). On the other hand, in hosing experiment, the freshwater discharges are usually discussed in the context of paleo-climate (Yang et al. 2015a), which may cause as s stronger AMOC weakening than Arctic sea ice loss (McManus et al. 2004). In Chapter 4, we adopt another method by altering the sea ice/snow reflectivity and emissivity parameters to explore the impacts of Arctic sea ice loss on global ocean circulations, heat uptake and redistribution.

Chapter 2

The effects of historical ozone changes on Southern Ocean heat uptake and storage

Abstract

Atmospheric ozone concentrations have dramatically changed in the last five decades of past century. Herein we explore the effects of historical ozone changes that include stratospheric ozone depletion on Southern Ocean heat uptake and storage, by comparing CESM1 large ensemble simulations with fixed-ozone experiment. During 1958-2005, the ozone changes contribute to about 50% of poleward intensification of the Southern Hemisphere westerly

winds in historical simulations, which intensifies the Deacon Cell and residual meridional overturning circulation, thus contributing to heat redistribution in the Southern Ocean. Heat budget analysis shows that, in response to historical ozone changes, heat is taken up between 50-58°S mainly through changes in sensible heat flux, shortwave radiation flux, and the flux due to seasonal sea ice formation and melt. A major part of the absorbed heat, however, is redistributed equatorward primarily through Eulerian mean ocean heat transport such that ocean heat storage peaks at lower latitudes, around 44°S. The ozone-induced interior warming contributes to about 22% of the historical Southern Ocean warming over 1958-2005. Poleward of 62°S where a subsurface temperature inversion occurs, shoaling isopycnals lead to warming and salinification in the upper ocean. To the north of 50°S, the deep-reaching warming and freshening that correspond to the ocean heat storage maximum are primarily set by the deepening of isopycnals. The large-scale patterns of isopycnal shoaling (deepening) at high (middle) latitudes are consistent with the overlying negative (positive) wind stress curl anomalies related to the poleward intensification of westerly winds, suggesting that the wind changes play an important role in the Southern Ocean heat redistribution under the ozone forcing.

2.1 Introduction

Earth's climate is largely regulated by the ocean. Associated with ongoing global warming, most of the excess heat is taken and stored in the ocean (Rhein et al. 2013), especially over the Southern Ocean [Sen Gupta et al. (2009); Frölicher et al. (2015); Shi et al. (2018)]. Observations show that the Southern Ocean has experienced a rapid subsurface warming during the past several decades [e.g., Gille (2002); Cai et al. 2010; Purkey and Johnson (2010); Durack et al. (2014); Roemmich et al. (2015); Liu et al. (2016)], along with a large increase in ocean heat content [Levitus et al. (2012); Durack et al. (2014); Llovel and Terray (2016); Cheng et al. (2017)] as a result of a variety of ocean heat uptake and transport processes (Zanna et al. 2019). It has been estimated that the Southern Ocean accounts for 60% – 90% of the global ocean heat content increase since 2006 (Sallée 2018). Therefore, changes in the Southern Ocean could potentially have significant consequences for the global climate [e.g., Gregory et al. (2001); Winton et al. (2010); Rose et al. (2014); Shi et al. (2020)].

The Southern Ocean temperature change has been attributed to both GHGs increase and stratospheric ozone depletion [Marshall et al. (2014); Previdi and Polvani (2014)]. Sigmond et al. (2011) and Swart et al. (2018) suggested that the observed warming in the interior Southern Ocean since the mid-twentieth century is primarily driven by human-induced GHGs increase

while the influence of stratospheric ozone depletion is relatively weak. On the other hand, Solomon et al. (2015) reported that more than 30% of subsurface warming in the Southern Ocean can be caused by ozone depleting substances in their model simulations. Moreover, the Southern Ocean responses to GHGs increase and ozone depletion are featured with distinct patterns, implying that different mechanisms and processes might be at play under each forcing in shaping the warming patterns and regulating the ocean heat uptake and storage.

The processes related to Southern Ocean heat uptake and storage under GHGs concentrations increases have been extensively explored. For example, Manabe et al. (1991) noticed the difference between the locations where heat enters the Southern Ocean at the surface and where heat is stored in the interior ocean and inferred meridional ocean heat transport to explain this difference. Later studies [e.g., Gregory (2000); Griffies et al. (2015)] showed that the Southern Ocean warming is determined by a balance between a northward/downward heat transport by Eulerian mean circulation and a southward/upward heat transport by eddies. This balance, moreover, is subject to changes under global warming in several possible ways: a reduction of southward/upward eddy-induced heat transport [Gregory (2000); Dalan et al. (2005); Hieronymus and Nycander (2013); Morrison et al. (2013)], an increase of northward/downward advective heat transport by Eulerian mean circulation

[Cai et al. (2010); Kuhlbrodt and Gregory (2012); Marshall et al. (2014); Bryan et al. (2014); Exarchou et al. (2015)], or a combination of both (Morrison et al. 2016). Meanwhile, Marshall et al. (2015) and He et al. (2019) found that the background ocean circulation in the Southern Ocean strongly influences the large-scale patterns of ocean heat uptake and storage. Similarly, both Gregory et al. (2016) and Garuba and Klinger (2016) showed that heat is taken up largely as a passive tracer in the Southern Ocean, which supports a simple model proposed by Church et al. (1991) that heat penetrates into the Southern Ocean mostly due to subduction along constant density surfaces and in a way similar to a passive tracer. On the other hand, Banks and Gregory (2006) and Xie and Vallis (2012) suggested that the ocean heat uptake can vary significantly due to changes in the ocean circulation and therefore cannot be viewed solely as a passive process. Their results are consistent with those from the fixed and free ocean circulations in Winton et al. (2013) and also those from eddy-resolved climate model simulations in Chen H. et al (2019). Recently, Liu et al. (2018) showed that, under increased atmospheric CO_2 concentrations, the wind-induced meridional ocean heat redistribution could contribute about 20% to the ocean heat storage maximum in the Southern Ocean.

Unlike the GHGs-induced ocean warming in which winds play a secondary role, the effect of ozone forcing on Southern Ocean heat uptake and storage could be mainly through the changes in the surface wind forcing and

the Southern Annular Mode (SAM, c.f. Marshall 2003). Observations show that the Southern Hemisphere westerly winds have shifted poleward and strengthened over the past several decades (Swart and Fyfe 2012) and the SAM (Marshall 2003) has meanwhile shifted toward a positive phase [Thompson and Solomon (2002); Hande et al. (2012)]. These wind and SAM changes have been attributed primarily to the ozone depletion in the Antarctic lower stratosphere [e.g., Gillett and Thompson (2003)] and secondarily to increasing GHGs [e.g., Fyfe (2006)]. Particularly, the ozone-induced poleward-intensified winds strengthen and displace the meridional overturning circulation (MOC) in the Southern Ocean (Solomon et al. 2015). According to the role of GHGs-driven poleward-intensified winds in Southern Ocean warming (Fyfe et al. 2007), ozone-driven wind changes may also prompt anomalous downward Ekman pumping to the north of the Antarctic Circumpolar Current (ACC), helping to enhance the downwelling of warm surface water there. Though this wind effect potentially serves as one leading mechanism explaining the interior Southern Ocean warming under ozone forcing [Sigmond and Fyfe (2010); Sigmond et al. (2011); Bitz and Polvani (2012); Smith et al. (2012)], the detailed mechanisms explaining how the ozone-induced MOC change alters Southern Ocean redistribution remain unclear. In this context, a more detailed Southern Ocean MOC and heat budget analysis is needed. Moreover, parallel to stratospheric ozone depletion, tropospheric

ozone has been found in a rising trend during the past several decades [Zhang et al. (2016); Yeung et al. (2019)]. It remains unclear how the combined stratospheric ozone depletion and tropospheric ozone increase affect the Southern Ocean heat uptake, redistribution and storage.

Another view to understand the Southern Ocean heat uptake and redistribution is through changes in the Southern Ocean ventilation and water masses [Waugh et al. (2013); Waugh et al. (2019); Shi et al. (2020)]. Subsurface ocean temperature and salinity changes at depth levels can be decomposed into spiciness and heave components, i.e., changes on isopycnal surfaces and changes due to movements of isopycnals, respectively [e.g., Bindoff and McDougall (1994)]. Bindoff and McDougall (1994) further proposed three physical processes: pure warming, pure freshening, and pure heave, to explore possible connections between subsurface ocean changes and different types of air-sea fluxes. These three processes have different signatures in temperature and salinity changes at depth levels and their spiciness and heave components. From this perspective, Böning et al. (2008) attributed the observed Southern Ocean warming and freshening trends during past decades to changes in surface heat and freshwater fluxes. Lyu et al. (2020) further showed that under anthropogenic climate change, the equatorward and downward subductions of surface heat and freshwater inputs in the high-latitude Southern Ocean can lead to cooling and freshening spiciness changes on density surfaces within the

Subantarctic Mode Water (SAMW) and Antarctic Intermediate Water (AAIW). Meanwhile, they suggested that both the wind forcing and the subduction of heat contribute to the deepening of isopycnals and enhanced warming in the midlatitude Southern Ocean. Gao et al. (2018) highlighted the role of wind forcing and reported that wind-driven thickening of the SAMW could explain most of the Southern Ocean warming over the Argo period since 2006. Given that stratospheric ozone depletion has been identified to play an important role in strengthening and shifting surface winds, it is interesting to explore how historical ozone changes affects Southern Ocean heat storage from the perspective of heave and spiciness decomposition and changes in the Southern Ocean ventilation and water masses.

In this study, we use climate model experiments with fixed ozone forcing to isolate and assess the effects of historical ozone changes on Southern Ocean heat uptake, redistribution and storage. Unlike previous detection and attribution analyses [e.g., Swart et al. (2018)], this study focuses on the mechanisms of historical ozone changes on modulating the Southern Ocean MOC, heat budget, and ventilation.

2.2 Climate model experiments and historical datasets

2.2.1 CESM1 large ensemble simulations and fixed-ozone experiment

We use the Community Earth System Model (CESM) version 1 (Hurrell et al. 2013) from the National Center for Atmospheric Research (NCAR) that includes the Community Atmosphere Model version 5 [CAM5, e.g., Neale et al. (2012)], the Community Land Model version 4 [CLM4, Lawrence et al. (2012)], the sea ice component version 4 [CICE4, Holland et al. (2012)] and the Parallel Ocean Program version 2 [POP2, Smith et al. (2010)] including ocean biogeochemical (BGC) model, and henceforth is called CESM1-CAM5-BGC. The model has a finite-volume dynamical core with a nominal 1° atmosphere and land horizontal grid (1.25° × 0.9° longitude by latitude) with 26 atmospheric layers in the vertical, and a nominal 1° ocean and ice horizontal grid with 60 ocean layers in the vertical. Since the ocean model is not eddy-resolved, it employs a variable coefficient in the Gent-McWilliams eddy parameterization [Gent and McWilliams (1990), hereafter GM], which allows the model to simulate an appropriate ocean response to wind change as indicated by eddy-resolving models (Gent and Danabasoglu 2011). For tracers, such as temperature, the horizontal diffusion follows the Redi isoneutral diffusion operator by GM parameterization and the vertical diffusion (mixing) follows the K-profile parameterization [KPP, c.f. Large et al. (1994)].

We use large ensemble simulations with the CESM1-CAM5-BGC, which consists of 42 members with all historical forcing prescribed as the Coupled Model Intercomparison Project phase 5 (CMIP5) standard historical experiment from 1920 to 2005 (except the first member is from 1850 to 2005). These ensemble members are generated by adding random round-off level perturbations in atmospheric initial conditions (Kay et al. 2015). We refer to these CESM1 large ensemble historical simulations as HIST hereafter. Meanwhile, we use an accompanying experiment with HIST in which all forcings are prescribed as historical integrations except atmospheric ozone concentrations (including both stratospheric and tropospheric concentrations) are fixed at their 1955 levels [HIST_fixedO_3; c.f., Landrum et al. (2017)]. HIST_fixedO_3 includes 8 ensemble members spanning 1955 to 2005, which were also generated by adding random round-off level perturbations to the atmospheric initial conditions. We calculate the difference between HIST and HIST_fixedO_3 ensemble averages (HIST minus HIST_fixedO_3) during 1958-2005 to examine the effect due to historical ozone changes.

2.2.2 CanESM5 and associated Ozone single-forcing simulations

CanESM5 is a fully coupled climate model participating in CMIP6 (Swart et al. 2019). The atmosphere component is the Canadian Atmosphere Model (CanAM5), which employs a spectral dynamical core with a T63

truncation (an approximate 2.8-degree horizontal resolution) and a hybrid sigma-pressure coordinate with 49 vertical layers up to about 1 hPa. The land component incorporates the Canadian Land Surface Scheme (CLASS) and the Canadian Terrestrial Ecosystem Model (CTEM). The ocean component is a modified version of the Nucleus for European Modelling of the Ocean model (NEMO), which includes ocean biogeochemistry represented by the Canadian Model of Ocean Carbon (CMOC) and employs a ~1-degree horizontal resolution and 45 vertical levels. The Louvain-la-Neuve sea-Ice Model version 2 (LIM2) also operates within the NEMO framework.

The ozone single-forcing experiments with CanESM5 are akin to their historical simulations but forced by stratospheric ozone variations only. The CanESM5 prescribes the ensemble mean monthly mean three-dimensional stratospheric ozone concentrations as simulated in its historical runs but has fixed three-dimensional long-term monthly mean tropospheric ozone concentrations from its preindustrial control runs. In particular, grid cells are categorized tropospheric when they have an ozone concentration below 100 ppbv (parts per billion by volume) in the climatology of the preindustrial control run. Albeit the tropopause height may alter with climate change, several studies [Stevenson et al. (2013); Checa-Garcia et al. (2018)] suggest that the tropopause choice only has a marginal effect on radiative forcing. To examine the ozone impacts on Southern Ocean interior warming during the

second half of the twentieth century, we adopt 10 ensemble members of ozone single-forcing (stratospheric ozone only) experiments from CanESM5.

Besides the 10-ensemble stratospheric ozone only experiment, CanESM5 also provides a 10-ensemble member historical total ozone-only experiment in which the model prescribes the monthly mean three-dimensional ozone concentrations from the historical simulation through the depth of the atmosphere. We adopt the simulations of this pair of ozone experiments to isolate and quantify the effects of stratospheric and tropospheric ozone on Southern Ocean interior warming.

2.2.3 Historical surface wind and ocean temperature datasets

To evaluate the performance of CESM1-CAM5-BGC in simulating historical surface wind changes, we use three atmospheric reanalysis products: ERA-20CM (Hersbach et al. 2015) from the European Centre for Medium-Range Weather Forecasts (ECMWF), the Japanese 55-year Reanalysis [JRA-55, Kobayashi et al. (2015)] and the NCEP/NCAR Reanalysis Project version 1 [NCEP/NCAR-R1, Kalnay et al. (1996)]. The ERA-20CM includes 10 ensemble members with a horizontal resolution of approximately 125 km (spectral truncation T159) on 91 vertical levels over 1899-2010 and we use the ensemble mean values. The JRA-55 has the TL319 (0.5º) horizontal resolution on 60

vertical levels from 1958 to the present. The NCEP/NCAR-R1 has a horizontal resolution of about 2.5° on 17 vertical pressure levels from 1948 to the present.

To evaluate the CESM1-CAM5-BGC simulation of historical Southern Ocean warming, we use two objectively analyzed ocean datasets, EN4 version 2.1 (EN.4.2.1) ocean temperature analysis (Good et al. 2013) and the Institute of Atmospheric Physics (IAP) ocean temperature analysis (Cheng et al. 2017), and two ocean reanalysis products, the German contribution to the Estimating the Circulation and Climate of the Ocean project version 3 (GECCO3) ocean synthesis (Köhl 2020) and the Ocean Reanalysis System 4 [ORAS4, Balmaseda et al. (2013)] from ECMWF. The EN4.2.1 ocean temperature analysis follows a bias correction scheme by Gouretski and Reseghetti (2010), which is a quasi-globally covered (83°S to 89°N) at a horizontal resolution of 1°, with 42 vertical levels from surface down to 5350 m and spanning from 1900 to the present. The IAP ocean temperature analysis has a global ocean coverage of 1° horizontal resolution on 41 vertical levels from the surface down to 2000 m, and a monthly resolution from 1940 to the present. The GECCO3 is based on the MITgcm (Massachusetts Institute of Technology general circulation model), with a nominally 0.4° resolution eddy-permitting horizontal resolution and 40 vertical levels, spanning from 1948 to 2018. The ORAS4 has a global ocean coverage of 1° horizontal resolution, with 42 vertical levels from the surface down to 5350 m and spanning from 1958 to 2015.

2.2.4 MOC

We examine the Southern Ocean MOC in CESM1-CAM5-BGC simulations. The Eulerian-mean MOC ($\bar{\psi}$) is calculated by integrating the meridional velocity v zonally and vertically:

$$\bar{\psi}(y,z) = \oint \int_{z}^{0} v\, dz'\, dx \tag{2.1}$$

where x, y and z are the zonal, meridional and vertical coordinates. This representation of the MOC is largely made up of the wind-driven Ekman circulation known as the Deacon Cell (Döös and Webb 1994). Similarly, the eddy-induced MOC (ψ^*) is calculated as:

$$\psi^*(y,z) = \oint \int_{z}^{0} v^*\, dz'\, dx \tag{2.2}$$

where v^* is eddy-induced velocity. In the POP2 ocean model, it is in form of a bolus velocity derived from the GM parameterization. In the Southern Ocean, there is a partial compensation between Eulerian-mean and eddy-induced MOCs [e.g., Marshall and Radko (2003)], yielding a residual MOC (ψ_{res}):

$$\psi_{res} = \bar{\psi} + \psi^* \tag{2.3}$$

2.3 Results

2.3.1 Evaluation of model historical simulations

We evaluate CESM1-CAM5-BGC by comparing its historical simulations with observations. We first examine the Southern Ocean warming

during 1958-2005. To minimize the observational uncertainties, we obtain the zonal mean ocean temperature trends during 1958-2005 as the average of the four datasets, i.e., the EN4, IAP, GECCO3 and ORAS4 (Figure A1). There was a robust warming tongue (>0.02 K/decade) in the Southern Ocean extending as deep as 900 m between 40°S and 50°S (Figure 2.1a). This deep warming tongue is well simulated by CESM1-CAM5-BGC large ensemble historical simulation (HIST) as seen from its ensemble mean (Figure 2.1b). The warming magnitude in observations seems slightly smaller than that in the ensemble mean of HIST. One factor to explain the difference is that the internal variability has been mostly eliminated in the HIST ensemble mean but still exists in observations.

We also compare the 1958-2005 trend of annual and zonal mean near-surface zonal winds between HIST and three atmosphere reanalysis datasets: ERA-20CM, JRA-55 and NCEP/NCAR-R1. We find a poleward intensification of near-surface westerly winds over the Southern Ocean in both the average of atmosphere reanalysis and the ensemble mean of HIST (Figure 2.1c,d,e). There are some minor differences between HIST and reanalysis, for example, the average of atmosphere reanalysis shows a slightly larger surface-wind intensification but a weaker southward shift than the ensemble mean of HIST. These differences could be related to internal variability of westerly winds as represented by inter-member spread of HIST, and also, the uncertainty within

atmosphere reanalysis due to weak observational constraints prior to satellite-era when surface wind observations were sparse over the Southern Ocean (Figure 2.1e). To summarize, our results suggest that CESM1-CAM5-BGC can reasonably simulate multiple key features of the observed historical changes in the Southern Ocean, such as the Southern Ocean warming and the poleward intensification of westerly winds. These results hence warrant further exploration of ozone effects on the Southern Ocean heat uptake and storage using CESM1-CAM5-BGC.

2.3.2 Climate responses due to historical ozone forcing

We first examine zonal mean atmospheric responses to ozone forcing during 1958-2005 based on differences between the ensemble averages of HIST and HIST_fixedO_3. The stratospheric ozone depletion causes a strong stratospheric cooling to the south of 30°S (Ramaswamy et al 2001), which is accompanied by a weak warming in the lower stratosphere and upper troposphere in the tropics [Polvani et al. (2011); Figure A2a]. This temperature response increases the meridional temperature gradient at tropopause levels between polar region and Southern Hemisphere midlatitudes (Haigh 1994), which explains the poleward intensification of Southern Hemisphere westerly winds from the perspective of increased baroclinic instability (Figure A2b). The wind response to ozone forcing is particularly strong during austral summer

(not shown), which is consistent with results from previous studies based on different climate models or different CAM versions [e.g., Polvani et al. (2011); Seviour et al. (2017); Son et al. (2010); Son et al. (2018)].

The atmospheric wind response, much to stratospheric ozone depletion, extends down to the ocean surface and consequently modulates ocean circulation. Over the Southern Ocean, surface westerly wind stress strengthens at the southern flank of the ACC but weakens to the north of the ACC (Figure 2.2a). Averaged zonally, the zonal wind stress response shows a dipole-like pattern, with negative (positive) anomalies to the north (south) of 48°S (Figure 2.2b). Positive wind stress anomalies peak around 60°S, with a maximum of about 0.0045 N/m2 contributing to about half of historical wind-stress changes. This poleward intensified wind stress shifts the Deacon Cell ($\bar{\psi}$) in the Southern Ocean poleward and strengthens the cell by about 0.8 Sv (1 Sv = $10^6 m^3/s$) at its maximum (Figure 2.3a). The eddy-driven circulation (ψ^*) is also strengthened due to increased isopycnal tilting and baroclinicity (Figure 2.3b), which partially offsets the wind-driven Deacon Cell. Consequently, the residual MOC (ψ_{res}) generally follows the changes in the Deacon Cell, producing a poleward-intensified MOC in the Southern Ocean (Figure 2.3c).

Besides altering atmospheric winds and ocean circulation, historical ozone forcing also induces changes in air-sea surface heat flux. The Southern Ocean gains heat (positive anomalous net surface heat flux) around 49°S-61°S

between 60°E and 105°E in the Indian Ocean sector, between 150°E and 155°W in the Pacific sector and across the whole Atlantic sector (Figure 2.4a). In particular, the ocean takes up heat primarily via positive sensible heat flux anomalies within 49°S-57°S (Figure 2.4b, green) and primarily via positive shortwave radiation flux anomalies within 57°S-61°S (Figure 2.4b, red). Meanwhile, the Southern Ocean loses heat (negative anomalous net surface heat flux) over 39°S-49°S and 61°S-72°S (Figure 2.4b, black).

Note here: (1) Shortwave radiation flux dramatically increases to the south of around 55oS [Figure 4d, red, also c.f. Solomon et al. (2015)], which results from a compensation between a reduced shortwave reflection (Figure 2.4d, coral) associated with receding Antarctic sea ice via ice-albedo feedback and an amplified shortwave reflection (Figure 2.4d, gold) by increased clouds (mainly by the high clouds, Figure A3). A similar compensation pattern was also found in Grise et al. (2013). However, the shortwave warming (Figure 2.4b, red) is partially compensated by enhanced longwave cooling (Figure 2.4b, blue), whilst plus the cooling from other heat flux components, the Southern Ocean loses heat in 61°S-72°S. (2) Changes in sensible heat flux generally resemble the pattern of the net surface heat flux change characterized by an enhancement to the north of 61°S while weakening to the south (Figure 2.4b, green), which are associated with changes in surface westerly winds and air-sea temperature contrast (Zhang and Cooke 2020). In response to ozone forcing,

air-sea temperature contrast exhibits a positive peak within 46°S-63°S where the relative warmer atmosphere allows heat to enter the ocean through sensible heat fluxes (Figure 2.4c and Figure 2.4f, dark red). Meanwhile, surface wind speed increases to the south of 48°S, which also helps amplify the sensible heat fluxes (Figure 2.4e and Figure 2.4f, light blue). (3) Latent heat cooling generally occurs across all the latitudes in the Southern Ocean (Figure 2.4b, purple). To the south of 48°, the increased surface wind speed promotes the latent heat cooling. (4) Historical ozone changes induce an annual mean retreat of Antarctic sea ice (Figure A6) as consistent with Sigmond and Fyfe (2010) and Sigmond and Fyfe (2013). This receding Antarctic sea ice cover is potentially related to decreased sea ice growth during austral fall-winter and increased melt during austral spring-summer, and the latter is associated with an off-continent sea ice migration at high latitudes and a poleward migration at midlatitudes during austral summer (Bitz and Polvani 2012). It has also been suggested that the intensified westerly winds could drive more warm upwelled water to the south of the ACC (Ferreira et al. 2015) and lead to a farther south ice edge throughout the year especially in austral winter (Shi et al. 2020). As a result, the meridional migration of sea ice induces positive heat flux anomalies within 49°S-61°S (Figure 2.4b, orange) but negative heat flux anomalies to the south of 61°S compensating the shortwave warming there.

2.3.3 Linking ocean heat uptake, transport and storage: an oceanic heat budget analysis

We analyze the Southern Ocean heat budget that links ocean heat uptake, transport and storage (Liu et al. 2018). Specifically, the zonally integrated full-depth oceanic heat budget is

$$\oint \int_{-H}^{0} \rho_0 C_P \frac{\partial \theta}{\partial t} dz' dx + \oint \int_{-H}^{0} \rho_0 C_P [\nabla \cdot (\mathbf{v}\theta + D)] dz' dx = \oint (NSHF) dx \quad (2.4)$$

where ρ_0 is seawater density, C_p is the specific heat of sea water, θ is potential temperature of sea water, $-H$ denotes the depth of ocean bottom. *NSHF* denotes net surface heat flux, which is the sum of radiative shortwave (SW) and longwave (LW) fluxes, turbulent sensible (SH) and latent (LH) heat fluxes and heat flux due to snow/sea ice formation and melt (IMS). ∇ and $\mathbf{v}$ are three-dimensional gradient operator and velocity, and $\mathbf{v} = \bar{\mathbf{v}} + \mathbf{v}^*$. D denotes diffusion and other sub-grid processes.

Based on Eq. (2.4), we define the ocean heat content (OHC) as

$$OHC = \oint \int_{-H}^{0} \rho_0 C_P \theta \, dz' dx \quad (2.5)$$

and the OHC tendency as ocean heat storage, i.e.,

$$OHS = \frac{\partial}{\partial t} OHC = \frac{\partial}{\partial t} \oint \int_{-H}^{0} \rho_0 C_P \theta \, dz' dx \quad (2.6)$$

and ocean heat uptake as:

$$OHU = \oint (NSHF) dx \quad (2.7)$$

and the meridional ocean heat transport as

$$OHT = \oint \int_{-H}^{0} \rho_0 C_p \left(\bar{\mathbf{v}}\theta + \mathbf{v}^*\theta + D \right) dz' dx = \overline{OHT} + OHT^* + OHT^d \qquad (2.8)$$

where $\overline{OHT} = \oint \int_{-H}^{0} \rho_0 \ C_p \bar{\mathbf{v}} \theta dz' dx$, $OHT^* = \oint \int_{-H}^{0} \rho_0 \ C_p \mathbf{v}^* \theta dz' dx$ and $OHT^d = \oint \int_{-H}^{0} \rho_0 \ C_p D dz' dx$. Eq. (2.8) shows that meridional ocean heat transport (OHT) can be induced by Eulerian-mean flow ($\overline{\text{OHT}}$), eddies (OHT*) and diffusion (OHT^{d}).

Therefore, the heat budget by Eq. (2.4) can be written as

$$OHS = OHU - \frac{\partial}{\partial y} OHT \qquad (2.9)$$

which indicates that ocean heat storage is determined by heat uptake from atmosphere-ocean interface and heat redistribution by ocean circulation via meridional gradient of ocean heat transport.

We start with analyzing the ozone effect in modifying OHT and its gradient during 1958-2005 based on differences between the ensemble averages of HIST and HIST_fixedO_3. The poleward-intensified Deacon Cell in the Southern Ocean causes a dipole-like pattern in $\overline{\text{OHT}}$ change, with an anomalous poleward $\overline{\text{OHT}}$ to the north of 48°S and an anomalous equatorward $\overline{\text{OHT}}$ between 48°S-61°S (Figure 2.5a, red). This $\overline{\text{OHT}}$ change is partially canceled by the change in OHT* due to the eddy compensation in MOC (Figure 2.5a, orange). Besides, changes in diffusive heat transport also show a dipole-like pattern with an anomalous equatorward OHT^{d} to the north of 48°S and an anomalous poleward OHT^{d} in 48°S-66°S (Figure 2.5a, blue). The latter

anomalous poleward OHT^d becomes dominant in the response of meridional heat transport to the south of 57°S. As a result of the changes in all these ocean heat transport components, OHT shows an anomalous convergence ($\frac{\partial}{\partial y}$OHT<0) to the south of 60°S peaking around 63°S, an anomalous divergence ($\frac{\partial}{\partial y}$OHT >0) within 51°S-60°S peaking around 56°S and an anomalous convergence ($\frac{\partial}{\partial y}$OHT <0) to the north of 51°S (Figure 2.5a, black).

The anomalous convergence and divergence of OHT well correspond to the pattern of net surface heat flux change. For example, while the Southern Ocean takes heat from the atmosphere at surface between 51°S-60°S (Figure 2.5b, blue), about half of this absorbed heat is redistributed to higher and lower latitudes in the interior ocean by ocean circulation and diffusion processes appearing as an anomalous divergence of oceanic meridional heat transport (Figure 2.5b, red). The residual heat is stored locally (OHS >0) (Figure 2.5b, black). To summarize, in response to historical ozone changes, heat is stored in the Southern Ocean to the north of 65°S as a result of ocean heat uptake and redistribution. The increased OHS peaks at around 44°S where the wind-induced Ekman downwelling happens [Fyfe et al. (2007); Cai et al. (2010); Liu et al. (2018); Lyu et al. (2020)].

It is evident that subsurface warming due to atmospheric ozone changes mainly occurs in the upper 1000 m over the Southern Ocean (Figure 2.6e),

which shows a pattern generally similar to that of historical warming (Figure 2.6a) but with a smaller magnitude while other forcings such as the well-mixed GHGs could be dominant (Figure 2.6c). Besides the subsurface warming, atmospheric ozone changes also induce salification to the south of 62°S and north of 46°S in the upper 800 m but freshening in 62°S-46°S that extends down to 2000 m (Figure 2.6f). These salinity changes are relatively weaker than those induced by other climate forcings (Figure 2.6b and 2.6d).

To further quantify the contribution of ozone-induced warming to the total historical warming in the Southern Ocean, we calculate the Southern Ocean OHC (within 35°S-70°S) from both HIST and HIST_fixedO_3. We find that the time-series of upper 2000-m OHC in HIST depicts a pronounced Southern Ocean warming during the past five decades, which is well consistent with observations (Figure 2.7a). The 1958-2005 OHC trends are similar between the HIST simulation and observations, which are 12.53±1.64 ZJ/decade (1 ZJ = 10^{21} joules) and 10.58±4.28 ZJ/decade, respectively. Below 2000 m, the 1958-2005 OHC trend in HIST is 2.77±0.82 ZJ/decade (Figure 2.7b). On the other hand, we find that the time-series of ozone-induced OHC is also in a robust warming trend over the Southern Ocean during 1958-2005 (Figure 2.7a). The 1958-2005 ozone-induced OHC trend is 2.78 ZJ/decade in the upper 2000 m and 0.61 ZJ/decade in the layers below 2000 m (Figure 2.7b). Integrated over the whole depth, the ozone-induced OHC trend accounts for about 22% of

the HIST OHC trend during 1958-2005, i.e., about one-fifth of the simulated historical warming in the Southern Ocean can be attributed to ozone changes.

From the ozone-induced warming over the interior Southern Ocean, it is also worth noting that a robust warming tongue extends downward and equatorward to the north of 60°S (Figure 2.6e), in a position as depicted by Morrison et al. (2016) between the Subantarctic Mode Water (SAMW) and Antarctic Intermediate Water (AAIW). This finding indicates that the ozone-induced subsurface warming could be potentially due to the alterations in the Southern Ocean water mass properties.

2.3.4 Decomposing temperature and salinity changes into heave and spiciness components

To further understand the Southern Ocean interior warming and heat storage from the perspective of the changes in Southern Ocean ventilation and water masses, we decompose the temperature and salinity changes at depth levels into the spiciness changes along isopycnals and heave-related changes due to the movements of isopycnals [Bindoff and McDougall (1994); Durack and Wijffels (2010)]. Similar decomposition has been widely applied to historical observations, reanalysis datasets and climate model simulations [e.g., Köhl (2014); Häkkinen et al. (2015); Desbruyères et al. (2017); Zhang and Yan (2017); Han and Yan (2018); Lyu et al. (2020); Clément et al. (2020); Wang

et al. (2021)]. Specifically, the spiciness reflects changes in the property of water mass due to subduction of surface temperature and salinity anomalies as well as modification by the interior mixing processes, whilst the heave of isopycnals could be related to wind-driven ocean circulation change or the subduction of added heat or freshwater at the surface (Lyu et al. 2020).

We first calculate neutral densities (Jackett and McDougall 1997) based on the ensemble-averaged temperature and salinity data over 1958-2005 from the HIST and HIST_fixedO_3. Then we derive spiciness changes due to ozone forcing as the differences of temperature and salinity trends during 1958-2005 on the same density surfaces between these two suites of simulations. The zonally averaged spiciness changes on density surfaces show enhanced warming (Figure 2.8a) and salinification (Figure 2.8b) trends toward the upper ocean at isopycnal outcrops except in polar region south of 70°S. To the north of 48°S, warming and salinification spiciness changes occur on the density surfaces between 25.3 and 26.7 kg/m^3, which are generally in the density ranges for the SAMW simulated by CMIP5 models (Sallée et al. 2013). As we remap the spiciness changes onto depth levels using the mean depth of each density surface, we find the major warming (> 0.3×10^{-2} K/decade) and salinification (> 0.4×10^{-3} psu/decade) trends extending equatorward and downward from surface layer at 65°S and occurring roughly in the upper 500 m to the north of 60°S (Figure 2.9c and Figure 2.9d). Meanwhile, cooling and

freshening spiciness changes exhibit along Antarctica continental shelf (Figure 2.9c and Figure 2.9d), which are likely related to the enhanced seasonal sea ice melt around the Antarctic resulting from a poleward migration of Antarctic sea ice in response to atmospheric ozone changes (Figure A6).

We further examine the heave component that is derived as the residual between the total change at depth level and the spiciness component. We find a subsurface warming tongue ($> 0.3 \times 10^{-2}$ K/decade) extending equatorward between 40°S-52°S and downward up to 1000 m depth (Figure 2.9e), which is associated with the deepening of isopycnals due to wind-driven downwelling forced by the positive wind stress curl anomalies (Figure 2.10). As a result, the enhanced warming in the midlatitude Southern Ocean (Figure 2.9a) could be attributed to both the spiciness and heave components, with the former (latter) dominating above (below) 300 m. To the south of 62°S where a vertical temperature inversion exists (the near-surface waters are cooler than the waters below, see contours in Figure 2.6a) due to seasonal melting/freezing and export of Antarctic sea ice (Marshall et al. 2014), negative surface wind stress curl anomalies drive a shoaling of isopycnals (Figure 2.10) and thus generate subsurface warming mainly between 100-300 m (Figure 2.9e). In 62°S-52°S where the vertical temperature inversion still exists but mainly occurs in the lower 100m, the isopycnal deepening driven by positive wind stress curl anomalies induces warming from the surface to 100m but cooling in 100-200

m (Figure 2.10 and Figure 2.9e). These wind-driven isopycnal movements resemble the case of a spin-up of the Southern Ocean MOC (Sen Gupta and England 2006). The meridional dipole-like changes of isopycnals (Figure 2.10) also induce dipole-like patterns of heave-driven salinity changes, with the freshening (salinification) trends to the north (south) of 62°S (Figure 2.9f), which explains much of the salinity response to atmospheric ozone changes in these latitudes (Figure 2.9b). Close to Antarctica, the warming and salinification heave changes largely compensate for the cooling and freshening spiciness changes in the lower 700m. Such compensation can be found in deep levels along the continental shelf of Antarctica (Figure 2.9c-f). Note that, owing to the slope of the isopycnals in the Southern Ocean, either a poleward (equatorward) shift or a downward (upward) shift of the isopycnals could result in similar changes. However, Lyu et al. (2020) have demonstrated that the heave-related changes are mainly due to the vertical rather than lateral movements of isopycnals.

It is worth noting that the ozone-driven heave of isopycnals is different from that under centurial climate change in future projections by CMIP5 models, considering that in latter the overall deepening of isopycnals is due to a large amount of added heat [Liu et al. (2018); Lyu et al. (2020)]. As such, the long-term GHGs warming could be strong enough to dominate over the wind-driven changes. In contrast, the downwelling (upwelling) at middle (high)

latitudes which are consistent with the sign of overlying wind stress curl anomalies (Figure 2.10) serves as important evidence that the wind forcing dominates changes in the ocean under the ozone forcing. This is further supported by our finding that the ozone forcing can not explain the cooling and freshening spiciness changes within the SAMW and AAIW (Figure 2.8), which has been widely observed and simulated under GHGs forcing [e.g., Durack and Wijffels (2010); Lyu et al. (2020)] as an indicator of the surface buoyancy forcing (Bindoff and McDougall 1994).

2.3.5 Stratospheric ozone depletion and tropospheric ozone increases drive Southern Ocean interior warming

Atmospheric ozone has experienced distinct changes in the stratosphere and troposphere during the second half of the twentieth century. Besides the ozone hole over Antarctica due to anthropogenic emissions of ozone-depleting substances [Farman et al. (1985); Rowland (1989); Solomon (1990); Fahey et al (2018)]. In contrast, ozone increases in the troposphere have been observed (Figure A7) as a result of anthropogenic emissions of ozone precursors such as methane, non-methane volatile organic compounds, carbon monoxide and nitrogen oxides [Young et al. (2018); Stevenson et al. (2013); Cooper et al. (2014); Yeung et al. (2019)]. However, ozone impacts on oceans, especially those due to tropospheric ozone changes, are relatively less well explored.

To quantify the impact of stratospheric and tropospheric ozone changes on Southern Ocean interior warming and investigate the mechanism, we further employ two ensembles of ozone single-forcing simulations performed with another climate model, CanESM5. The first CanESM5 ensemble is forced with historical changes in both stratospheric and tropospheric ozone while the second ensemble simulation is forced with historical integrations of solely stratospheric ozone changes (see Methods). The difference between the two ensemble simulations therefore isolates the effect of tropospheric ozone change.

We explore the spiciness and heave components of temperature response in the Southern Ocean in the two CanESM5 ensemble simulations during 1955-2000. We find the major spiciness warming (>0.01 K/decade) trends in response to total atmospheric ozone variations extending equatorward and downward from the surface layer at 60°S to about 600 m at 40°S (Figure 2.11a). The stratospheric ozone depletion is responsible for most of the ozone-induced warming trends in the upper 500 m (Figure 2.11c) while tropospheric ozone increases primarily account for the spiciness warming below (Figure 2.11e).

We further analyze the heave component of Southern Ocean temperature change. We find a subsurface warming region (>0.01 K/decade) extending equatorward between 36°S and 51°S and downward in 300-1100 m (Figure 2.11b) in response to atmospheric ozone changes, accompanying with

a cooling tongue to the north and in upper levels. This pair of warming and cooling anomalies has been linked to poleward intensified surface westerly winds and indicates the heat redistribution within the Southern Ocean [Liu et al. (2018); Cai et al. (2010)]. Specifically, stratospheric ozone depletion drives an intensification of surface westerly winds at and to the south of the Antarctic Circumpolar Current but a relaxation to the north (Figure 2.12c). The zonally averaged zonal wind change exhibits a dipole-like pattern, with positive and negative anomalies to the south and north of around 50°S. The resultant anomalous Ekman transport convergence and wind-driven downwelling produces a deepening of isopycnals in the latitudes around 50°S and hence heave changes of warming. While to the north of about 43°S, the weakening of surface westerlies decays, which prompts an anomalous Ekman transport divergence and wind-driven upwelling and thus leads to shallower isopycnals and cooling heave changes in these latitudes (Figure 2.11d).

Tropospheric ozone increases, on the other hand, engender different changes in surface winds from those due to stratospheric ozone depletion (Figure 2.12c). The zonally averaged surface zonal wind change also reflects a dipole-like pattern but located more northward, with positive and negative anomalies occurring to the south and north of around 42°S. This pattern indicates less poleward displaced surface westerlies than their counterparts driven by stratospheric ozone depletion. In the ocean, the wind-driven

compression produces isopycnals deepening in much lower latitudes, around 42°S, and warming heave changes there (Figure 2.11f). These heave-related warming changes are much stronger than those induced by stratospheric ozone depletion, which is likely due to the fact that oceanic thermocline is more strongly stratified at lower latitudes (Lyu et al. 2020), allowing the wind-driven downwelling more effectively to create warming heave changes.

2.4 Conclusion and discussion

In this study, we investigate the effects of historical ozone changes on Southern Ocean heat uptake and storage by comparing CESM1-CAM5-BGC historical simulations with fixed atmospheric ozone concentrations experiment. We find that atmospheric ozone changes, in particular the stratospheric ozone depletion, can contribute to about 50% of the intensification and poleward migration of Southern Hemisphere westerly winds during 1958-2005. These winds changes strengthen and shift the Deacon Cell and residual MOC in the Southern Ocean, and accordingly, act to redistribute oceanic heat across different latitudes. Our heat budget analysis shows that, in response to atmospheric ozone changes, heat enters the Southern Ocean mostly in 50-58°S via the changes of sensible heat flux, shortwave radiation flux and the flux due to seasonal sea ice formation and melt, and is carried to lower latitudes primarily through the changes in Eulerian mean oceanic heat transport. As a

result, ocean heat storage peaks around 44°S. In terms of a full-depth integrated OHC, the ozone induced warming contributes to about 22% of the historical warming over the Southern Ocean during the past five decades. Our further analysis of heave and spiciness changes suggests that the wind changes play an important role in the Southern Ocean temperature and salinity changes under ozone forcing. We find that historical ozone forcing leads to spiciness changes that warm and salify the upper ocean at isopycnal outcrops but cool and freshen along the Antarctica continental shelf. Meanwhile, they also result in isopycnals shoaling to the south of 62°S corresponding to warming and salinification trends. To the north of 50°S, the deep-reaching warming tongue is primarily determined by the isopycnals deepening owing to wind-driven downwelling.

We further isolate the effects of stratospheric ozone depletion and tropospheric ozone increases. We show that tropospheric ozone increases cause Southern Ocean subsurface warming primarily via the deepening of isopycnals. They give rise to an intensification of surface westerly winds over the Southern Ocean such that the wind-driven compression brings about isopycnal deepening around 42°S and prompts warming heave changes there. On the other hand, stratospheric ozone depletion promotes warming in the Southern Ocean mainly through spiciness changes along isopycnals in the upper 500m. In response to stratospheric ozone depletion, the net surface heat flux increases

but freshwater flux decreases over the Southern Ocean between 40°S and 60°S, contributing to the warming and saltening spiciness changes in the isopycnal outcropping regions of the Southern Ocean.

It merits attention that aforementioned results reflect a combined impact of the changes in both stratospheric and tropospheric ozone concentrations during the past five decades. While the separation of individual effects from stratospheric and tropospheric ozone changes on Southern Ocean heat uptake and storage warrants our future work, especially when considering the Antarctic ozone hole has recently begun to show signs of recovery owing to the effects of the Montreal Protocol. In particular, the stratospheric-ozone-driven Southern Hemisphere circulation change such as a poleward displacement of Southern Hemisphere westerly jets has seemed to be paused or even slightly reversed around the year 2000 (Banerjee et al. 2020). In future decades, the stratospheric ozone recovery is expected to continue, which could broadly affect the Earth system (Sigmond et al. 2011). For example, Smith et al. (2012) showed that future stratospheric ozone recovery will substantially mitigate Antarctic sea ice loss in the coming decades by diminishing summertime wind stress on the upper ocean at high-latitudes and generating cooler ocean temperatures. As such, it is plausible to anticipate that stratospheric ozone recovery will play an important role in future Southern

Ocean heat uptake and storage under various climate change scenarios [Shi et al. 2018; Chen C. et al. (2019); Ma et al. (2020)].

Besides, it is also worth noting the discrepancy between the observed and simulated Antarctic sea ice trends and its potential effects on Southern Ocean heat uptake. Since the satellite era, Antarctic sea ice extent has exhibited a slight but statistically significant increase over more than three decades [e.g., Comiso and Nishio (2008)], which has been attributed to a variety of factors such as the El Niño–Southern Oscillation (Stammerjohn et al. 2003), the Interdecadal Pacific Oscillation (IPO) (Meehl et al. 2016) and/or the Amundsen Sea Low (Turner et al. 2015), the Atlantic Multidecadal Oscillation (AMO) (Li et al. 2014), natural variability of Southern Ocean convection (Zhang et al. 2019) and pole-to-pole teleconnection (Liu and Fedorov 2019). In austral spring 2016, Antarctic sea ice extent has experienced an abrupt drop (Turner et al. 2017) due to a combination of tropically forced and internal Southern Hemisphere atmospheric variability [Stuecker et al. (2017); Meehl et al. (2019); Purich and England (2019)]. In contrast to the observed Antarctic sea ice changes, CESM1-CAM5-BGC simulates a negative trend of Antarctic sea ice extent since 1979 (Schneider and Deser 2018). Indeed, this discrepancy between the observed and model simulated historical Antarctic sea ice trend is a common issue in almost all the CMIP5 (Rosenblum and Eisenman 2017) and CMIP6 (Roach et al. 2020) models, which cannot be simply explained by

internal variability but might be related to models' response to external forcing [Schneider and Deser (2017); Chemke and Polvani (2020)]. Given that sea ice variations may influence ocean heat uptake close to the Antarctic (Bitz et al. 2006), improving model's simulation of the Antarctic sea ice changes would help to better simulate and understand the physical processes of Southern Ocean heat uptake and storage.

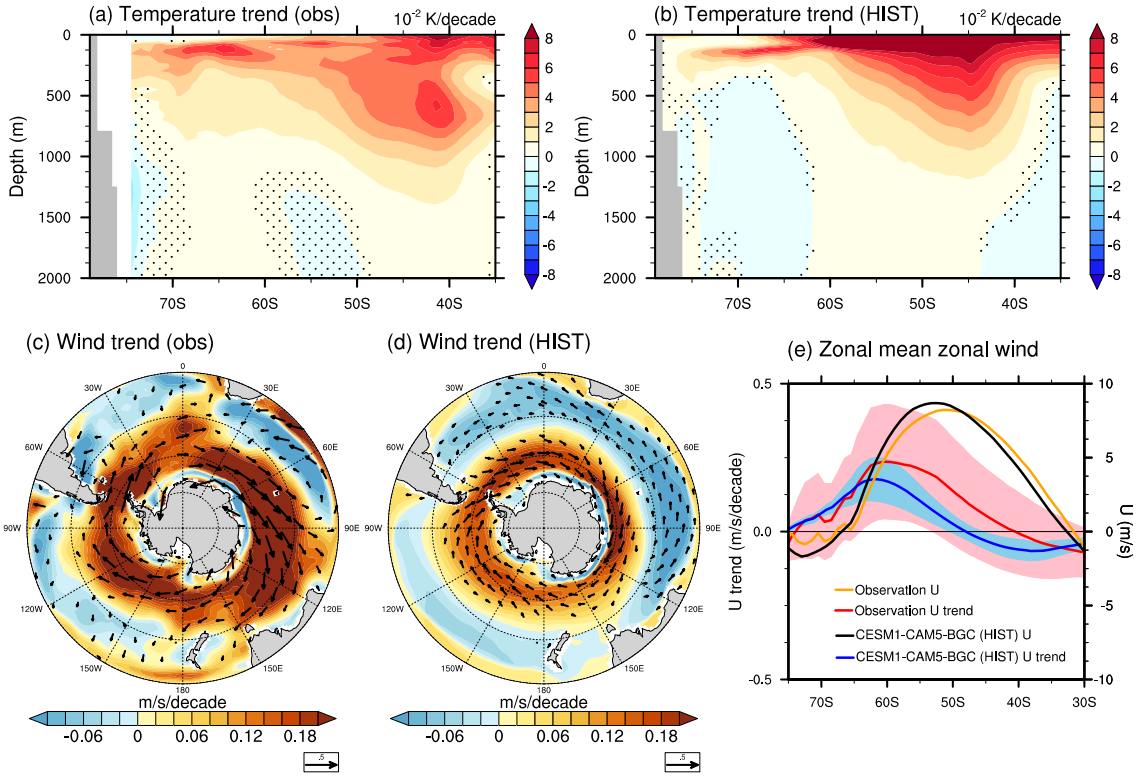

Figure 2.1 : (upper row) Annual and zonal mean ocean temperature trends (shading in 10^{-2} K/decade) during 1958-2005 in (a) the average of four observational datasets and (b) the ensemble mean of CESM1-CAM5-BGC historical large ensemble simulations (HIST). Stippling denotes where the trends are not statistically significant at the 95% confidence level. (bottom row) Trends of surface winds (vectors) and wind speed (shading) over ocean/sea ice at 992.5 hPa in (c) the average of three atmospheric reanalysis datasets and (d) the ensemble mean of HIST during 1958-2005. (e) Trends of zonally averaged zonal winds over ocean/sea ice at 992.5 hPa from atmospheric reanalysis (average, red; light red shading refers to one standard deviation), HIST (ensemble mean, blue; light blue shading refers to one standard deviation) during 1958-2005. The annual and zonal mean zonal winds over ocean/sea ice at 992.5 hPa from the average of atmospheric reanalysis (orange) and the ensemble mean of HIST (black) during 1958-2005 are superposed.

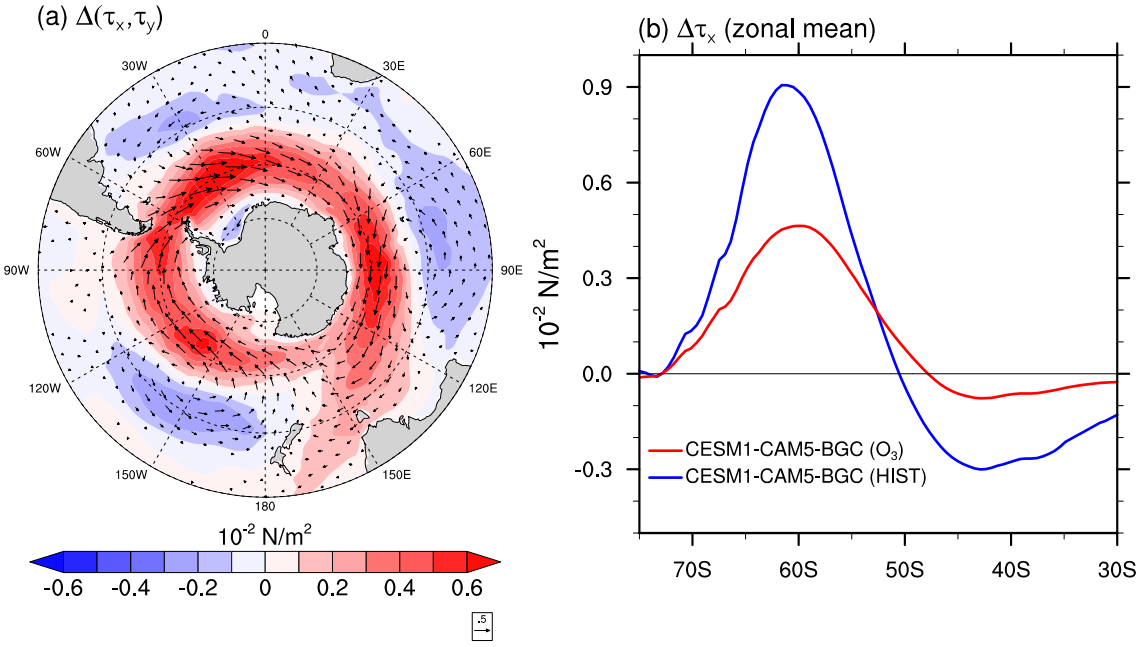

Figure 2.2: (a) Changes in annual mean surface wind stress (vector in 10^{-2} N/m^2) and zonal mean zonal wind stress (shading in 10^{-2} N/m^2) due to atmospheric ozone change during 1958-2005 in CESM1-CAM5-BGC. (b) Changes in zonally averaged zonal wind stress due to atmospheric ozone change (red) and in HIST (blue) during 1958-2005 in CESM1-CAM5-BGC. The change in HIST is calculated as the 1958-2005 average of the ensemble mean of HIST minus the 1850-1954 average of the first member for CESM1-CAM5-BGC HIST.

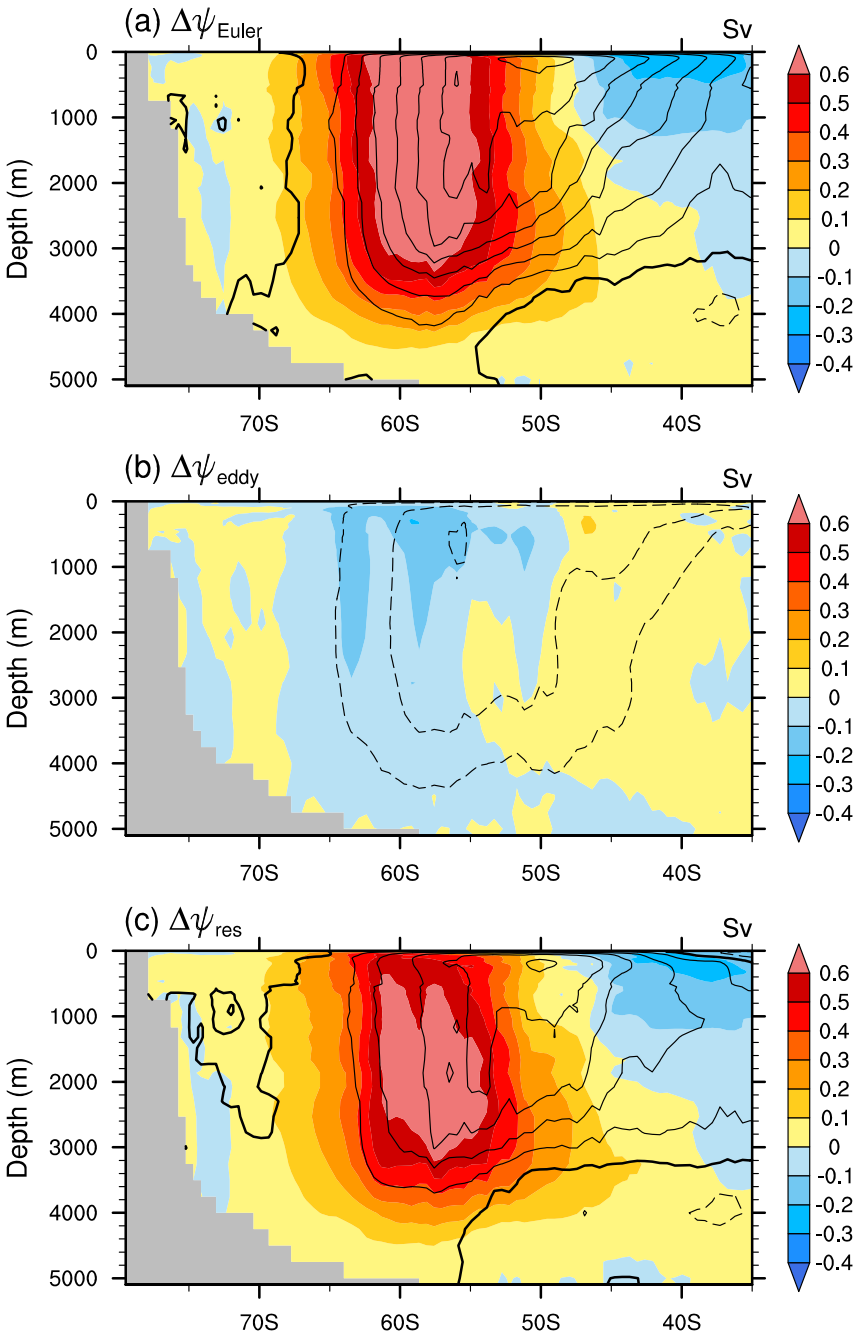

Figure 2.3: Changes in annual mean (a) Eulerian mean, (b) eddy-induced, and (c) residual MOCs (shading in Sv) due to atmospheric ozone change during 1958-2005 in CESM1-CAM5-BGC. Annual mean MOC climatology from HIST _fixedO_3 ensemble mean during 1958-2005 is shown in each panel [contours in Sv, with a contour interval of 5 Sv, zero contours thickened and solid (dashed) contours indicating positive (negative) values].

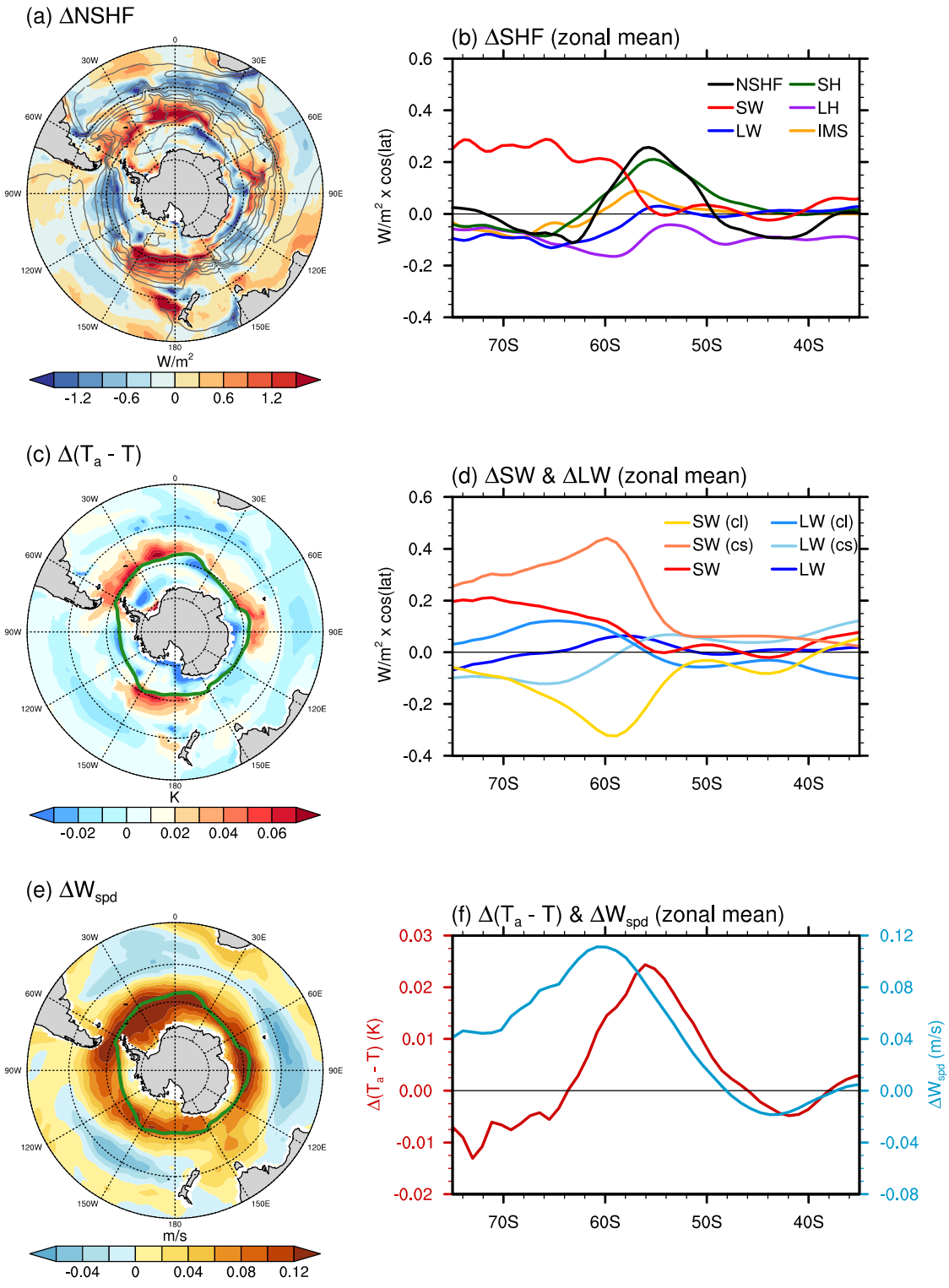
(a) ΔNSHF
W/m2
-1.2 -0.6 0 0.6 1.2
(b) ΔSHF (zonal mean)
NSHF SH
SW LH
LW IMS
W/m2 x cos(lat)
70S 60S 50S 40S
(c) Δ(Ta - T)
K
-0.02 0 0.02 0.04 0.06
(d) ΔSW & ΔLW (zonal mean)
SW (cl) LW (cl)
SW (cs) LW (cs)
SW LW
W/m2 x cos(lat)
70S 60S 50S 40S
(e) ΔWspd
m/s
-0.04 0 0.04 0.08 0.12
(f) Δ(Ta - T) & ΔWspd (zonal mean)
Δ(Ta - T) (K)
ΔWspd (m/s)
70S 60S 50S 40S

Figure 2.4: Changes in annual mean (a) net surface heat flux (NSHF), (c) air-sea surface temperature contrast (shading in K), (e) surface wind speed at 10 m (shading in m/s) in response to atmospheric ozone change during 1958-2005 in CESM1-CAM5-BGC. Changes in annual zonal mean of (b) net surface heat flux (NSHF; black), shortwave (SW; red) and longwave (LW; blue) radiation fluxes, sensible (SH; green) and latent (LH) heat fluxes and the flux due to snow/sea ice formation and melt (IMS; orange) weighted by cosine latitude, (d) downward shortwave (SW; red) and longwave (LW; blue), downward shortwave [SW (cs); coral] and longwave [LW (cs); sky blue] with clear sky, and downward shortwave [SW (cl); gold] and longwave [LW (cl); dodger blue] due to cloud effects, (f) air-sea surface temperature contrast (dark red) and surface wind speed at 10 m (light blue) in response to atmospheric ozone change during 1958-2005 in CESM1-CAM5-BGC. The averaged path of the ACC over 1958-2005 is superposed in (a) that is represented by the contours of annual mean barotropic stream function from the 1958-2005 averages of the ensemble means HIST_fixedO_3 (gray). Annual mean climatological sea ice edges (green) that are based on 15% sea ice fraction from HIST_fixedO_3 ensemble mean during 1958-2005 are superposed in (c) and (e).

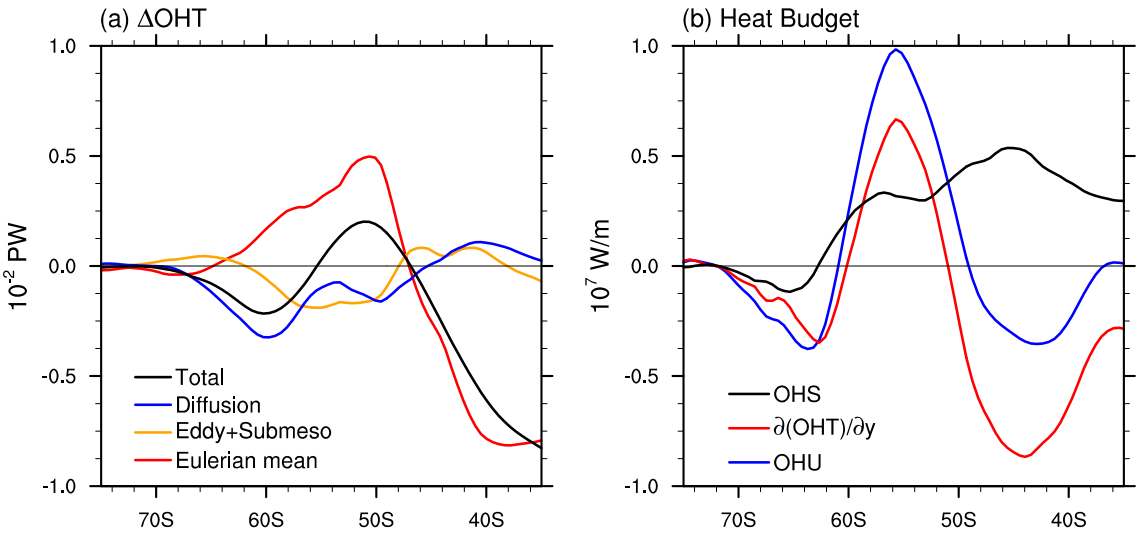

Figure 2.5: Changes in (a) annual mean total northward oceanic heat transport (black) and components induced by Eulerian mean flow (red), mesoscale and sub-mesoscale eddies (orange) and diffusion processes (blue) and (b) annual mean ocean heat budget terms (Eq. 2.9): *OHU* (blue), $\partial(OHT)/\partial y$ (red) and *OHS* (black) in the Southern Ocean due to atmospheric ozone change during 1958-2005 in CESM1-CAM5-BGC.

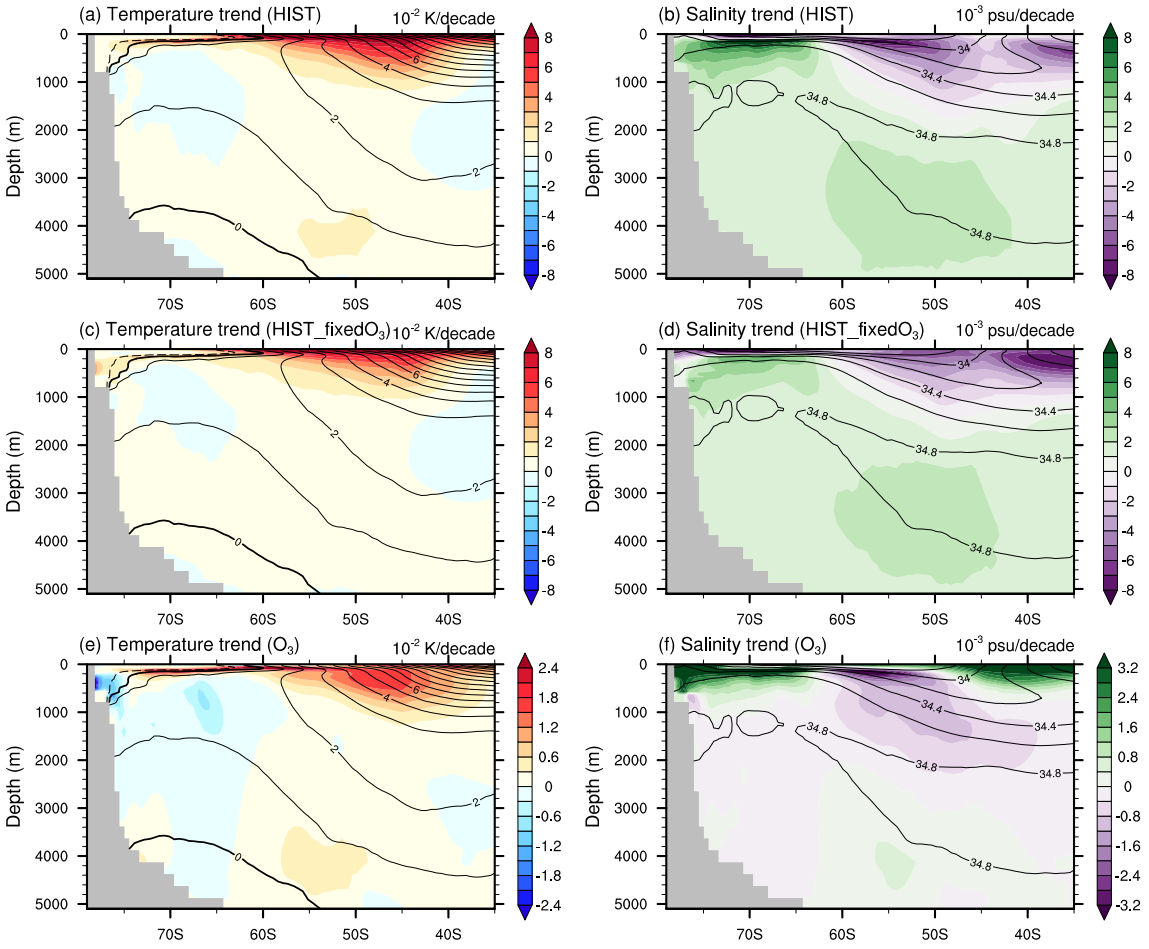

Figure 2.6: Left column: annual and zonal mean ocean temperature trends (shading in 10^{-2} K/decade) in the ensemble mean of (a) HIST and (c) HIST_fixedO_3 as well as those (e) due to the effect of atmospheric ozone change during 1958-2005 in CESM1-CAM5-BGC. The superposed contours denote the 1850-1954 average of zonal mean ocean temperature from the first member for CESM1-CAM5-BGC historical simulation. Right column: as in the left column but for ocean salinity trends.

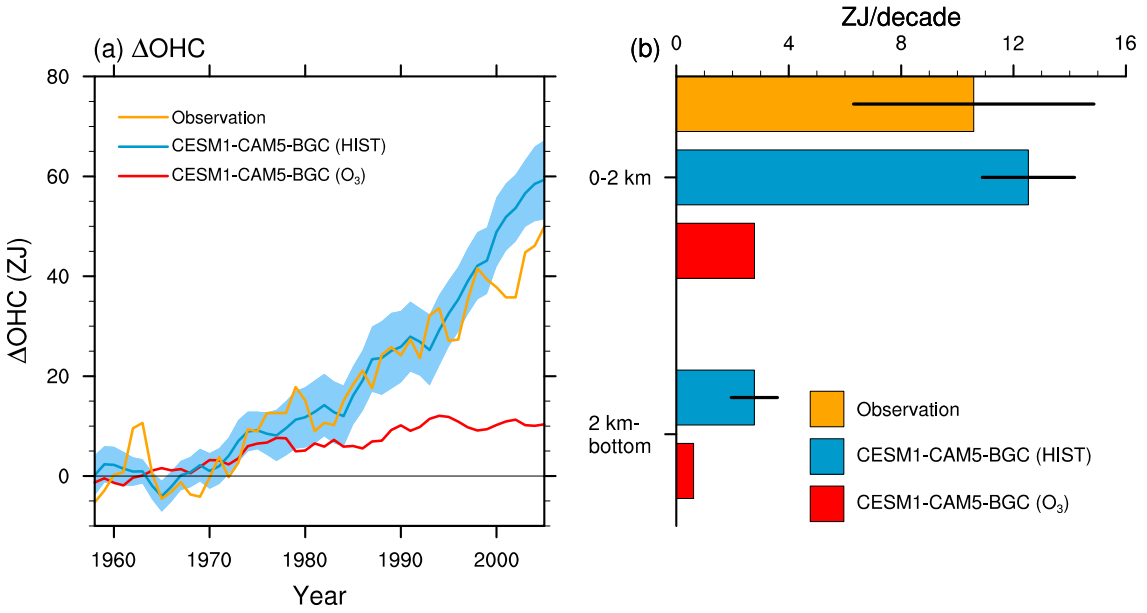

Figure 2.7: (a) Time series of annual mean ocean heat content (OHC) anomalies in the upper 2000 m in the Southern Ocean (35°S-70°S) during 1958-2005 from observations (the average of four observational datasets, orange) and HIST (ensemble mean, blue; light blue shading refers to one standard deviation) as well as those due to atmospheric ozone change in CESM1-CAM5-BGC (red). The anomalies are relative to 1958-1972 averages of individual observations/simulations. (b) The upper 2000 m OHC trends during 1958-2005 for the average of four observational datasets (orange), the ensemble mean of HIST (blue) and the ozone-driven part (red). Black lines indicate one standard deviation in observation datasets and HIST ensemble members, respectively. The 1958-2005 trend of OHC below 2000 m is also shown for the ensemble mean of HIST (blue) and the ozone-driven part (red).

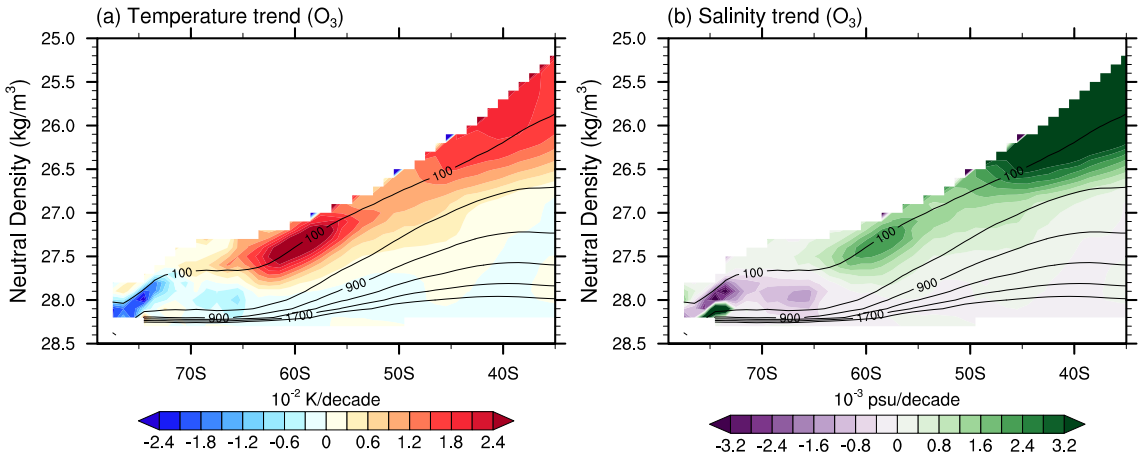

Figure 2.8: Spiciness changes of annual and zonal mean (a) temperature (shading in 10^{-2} K/decade) and (b) salinity (shading in 10^{-3} psu/decade) trends during 1958-2005 on density surfaces due to atmospheric ozone change in CESM1-CAM5-BGC. In each panel, the mean depth levels from HIST_fixedO_3 ensemble mean during 1958-2005 are superimposed as contours.

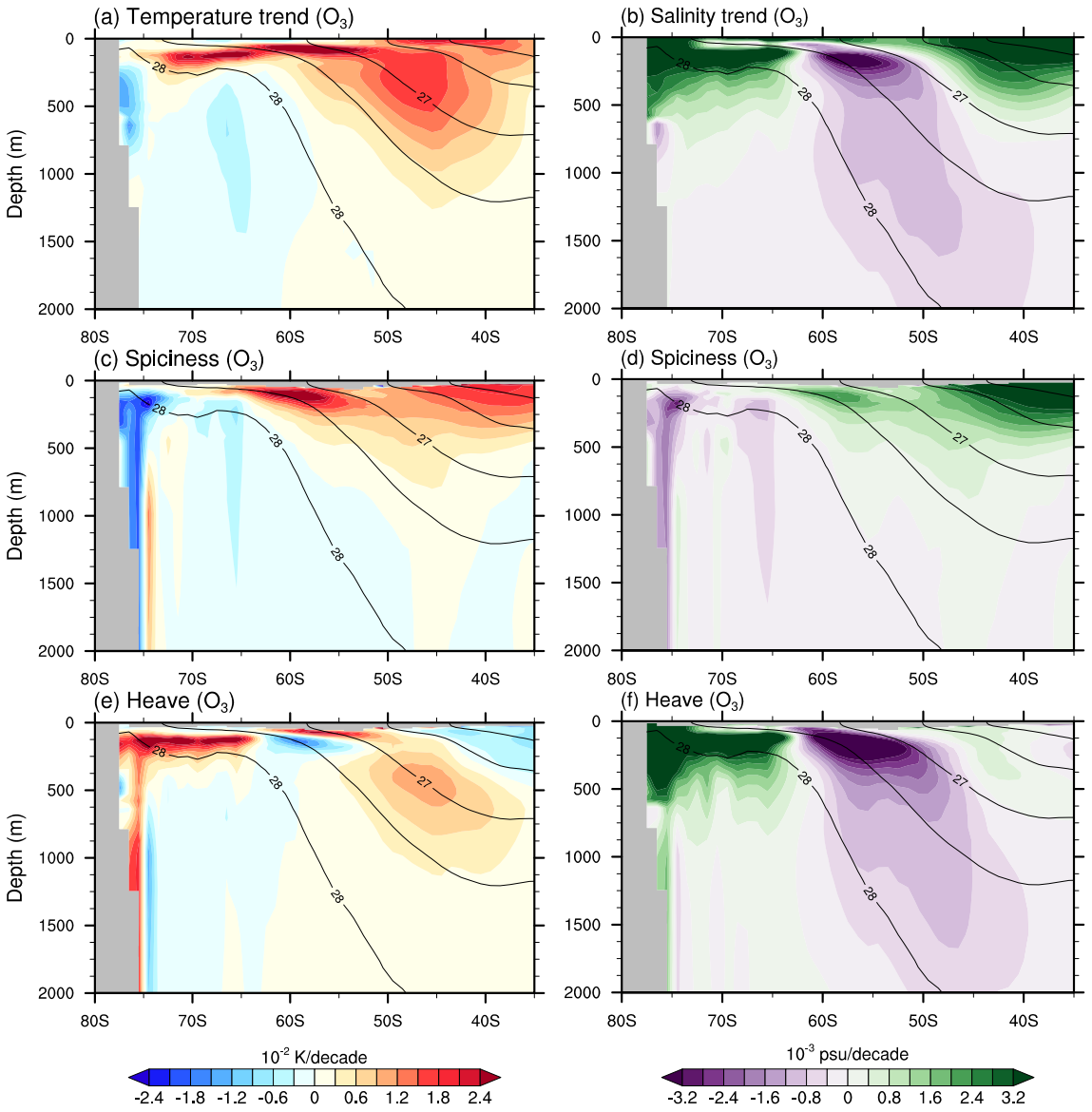

Figure 2.9: (left column) (a) Total, (c) spiciness and (e) heave changes of annual and zonal mean ocean temperature trends (shading in 10^{-2} K/decade) due to atmospheric ozone change in CESM1-CAM5-BGC. In each panel, the mean density surfaces from HIST_fixedO_3 ensemble mean during 1958-2005 are superimposed as contours. (right column) Similar to the left column but for changes of annual and zonal mean salinity trends (shading in 10^{-3} psu/decade).

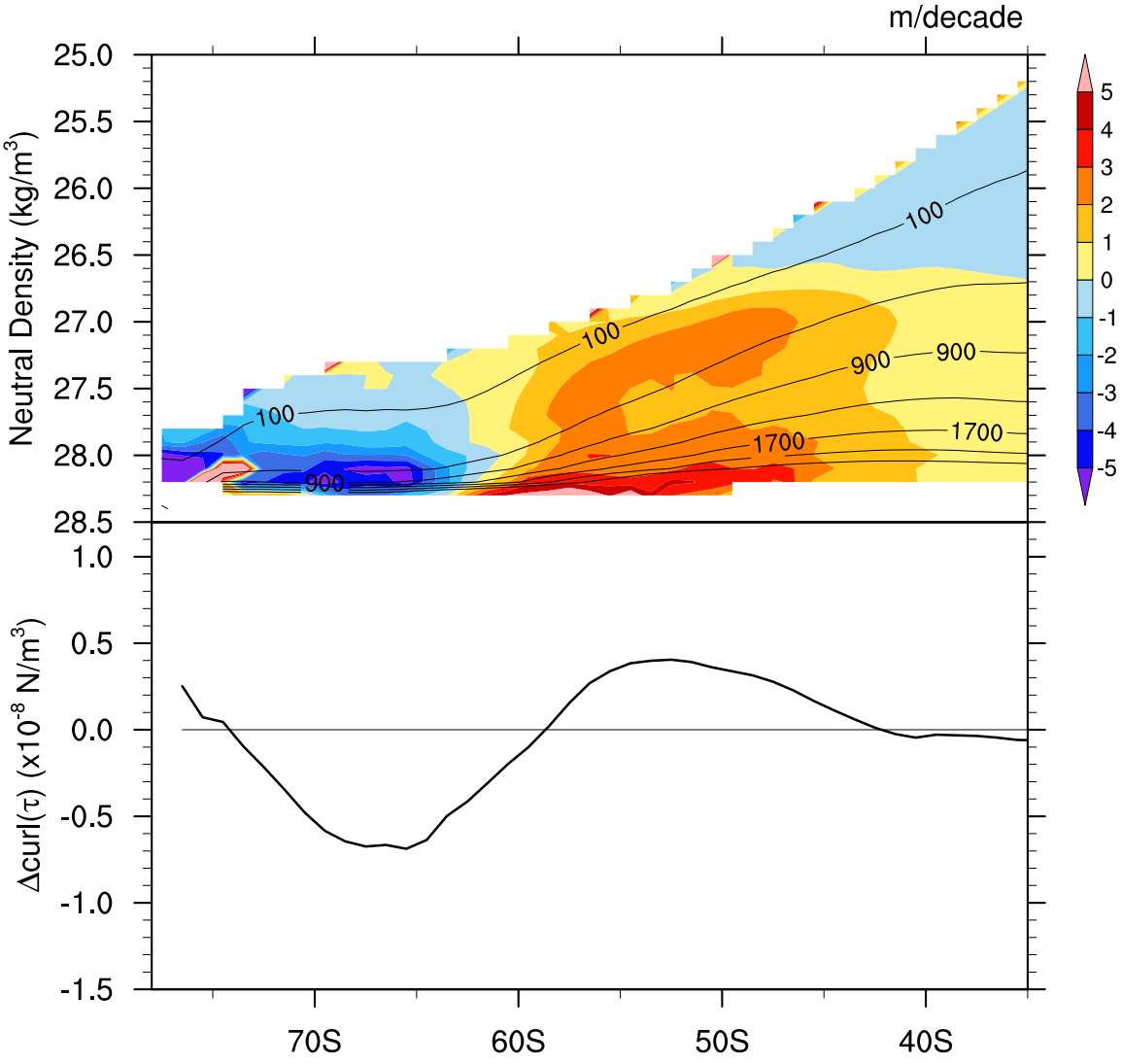

Figure 2.10: Changes in the depth of density surfaces (shading in m/decade, positive downward) during 1958-2005 due to atmospheric ozone change in CESM1-CAM5-BGC. The mean density surfaces from HIST_fixedO_3 ensemble mean during 1958-2005 are superimposed as contours. Changes in annual and zonal mean surface wind stress curl due to atmospheric ozone change are attached.

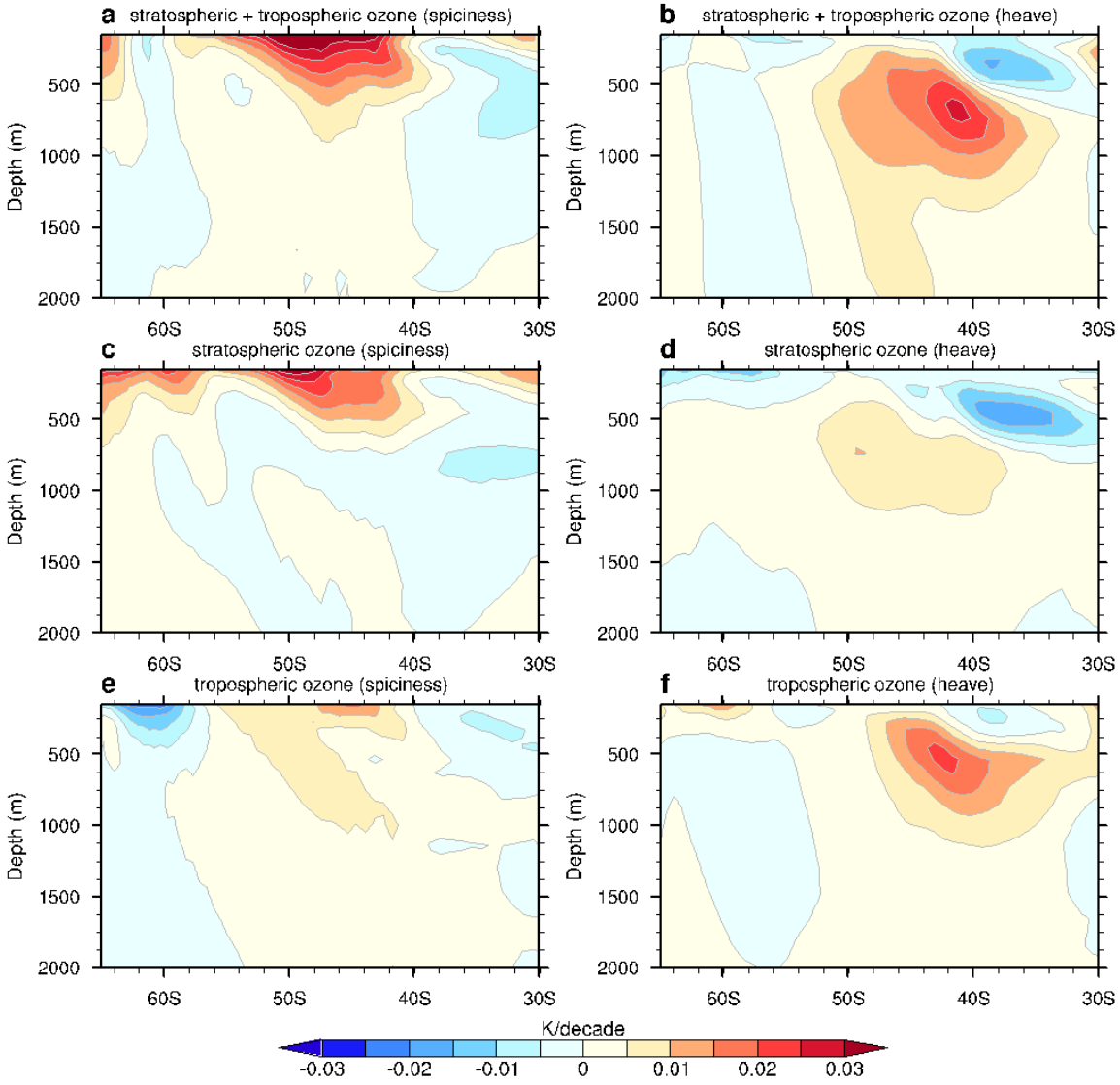

Figure 2.11: Spiciness and heave changes of ocean temperature in CanESM5 ozone experiments. (left column) Spiciness changes in annual and zonal mean ocean temperature trends during 1955-2000 (shading in K/decade) above 2000 m but below the mixed layer (~150 m) in the Southern Ocean for the ensemble means in CanESM5 (a) stratospheric and tropospheric ozone experiment and (c) stratospheric ozone only experiment as well as (e) the difference between the two indicating the effect of tropospheric ozone change. (right column) Same as the left column but for heave changes.

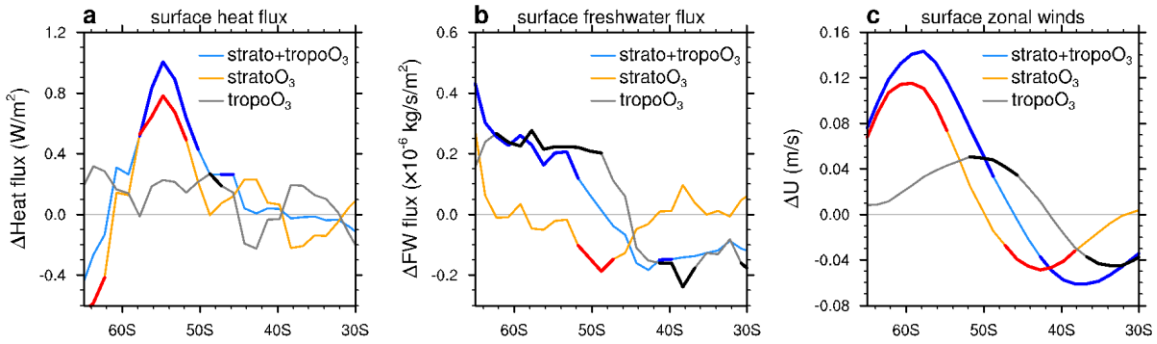

Figure 2.12: Spiciness and heave changes of ocean temperature in CanESM5 ozone experiments. (left column) Spiciness changes in annual and zonal mean ocean temperature trends during 1955-2000 (shading in K/decade) above 2000 m but below the mixed layer (~150 m) in the Southern Ocean for the ensemble means in CanESM5 (a) stratospheric and tropospheric ozone experiment and (c) stratospheric ozone only experiment as well as (e) the difference between the two indicating the effect of tropospheric ozone change. (right column) Same as the left column but for heave changes.

Chapter 3

Anthropogenic aerosol and greenhouse gas driven ocean heat uptake and redistribution

Abstract

Anthropogenic aerosols and greenhouse gases have played important roles in modulating oceanic heat since the industrial age. Here we isolate and quantify the effects of both forcers using climate model simulations. We show that, in response to anthropogenic aerosols, the Southern Ocean imports heat from the Indo-Pacific but exports heat into the Atlantic. Ocean heat uptake (OHU) diminishes in the subpolar Atlantic. Alterations in ocean circulation and temperature have a weak compensation in contributing to interbasin heat

exchange. Consequently, interbasin heat exchange is comparable to OHU changes, both of which are effective to modify the stored heat in the Atlantic and Indo-Pacific. Anthropogenic greenhouse gases, on the other hand, promote the OHU in the subpolar Atlantic and allow the Southern Ocean to import heat from the Atlantic but export heat to the Indo-Pacific. Ocean circulation-induced heat transport change is strongly offset by temperature-induced heat transport change, which is different from the scenario under aerosol forcing. Interbasin heat exchange, accordingly, is far smaller than OHU changes so that OHU primarily controls ocean heat storage. We further leverage observations to assess model's credibility in simulating oceanic heat variations and find that model results are within observation constraints when considering observation uncertainties.

3.1 Introduction

Anthropogenic aerosols and greenhouse gases are regarded as the two major forcers driving Earth's energy imbalance since the industrial age [Shindell et al. (2015); Von Schuckman et al. (2016)]. Most of the excessive energy has been absorbed by oceans through surface in the form of OHU, as reflected from the changes in the net surface heat flux. On multi-decadal or longer time scales, compared to the North Atlantic, the Southern Ocean has experienced larger OHU during the historical period [Frölicher et al. (2015);

Zanna et al. (2019)], especially since the middle of the twentieth century (Levitus et al. 2012), which at least can be attributed in part to the distinct anthropogenic aerosol and greenhouse gas impacts. It has been suggested that the rising greenhouse gases enhance the OHU over most of global oceans, whilst in the North Atlantic, greenhouse gas-induced OHU increases are heavily compensated by aerosol-induced OHU decreases, thus leaving marginal ocean heat content (OHC) changes in this ocean basin [Bilbao et al. (2019); Irving et al. (2019); Ma et al. (2020); Paynter et al. (2015); Shi et al. (2018)]. Over the recent decade, internal climate variability seems also to influence the regional OHU. The rapid and high heat gain of the Southern Ocean during 2005-2015 was indicated to result from a combined effect of anthropogenic warming and internal variability (Rathore et al. 2020). In the North Atlantic, a reversal of warming trend was found over 2005-2014 when compared to the previous decade, which could be related to a long-term freshening in the deep Labrador Sea (Robson et al. 2016).

Nevertheless, the heat taken by oceans in response to anthropogenic aerosols and greenhouse gases is not always stored locally, seeing that the concurrent ocean circulation changes modify ocean heat transports (OHTs) across individual basins as well as interbasin heat exchange. For example, anthropogenic greenhouse gas increases cause a weakened Atlantic Meridional Overturning Circulation (AMOC), and hence alter the meridional OHT in the

Atlantic [Gregory et al. (2016); Liu et al. (2020); Winton et al. (2013)] and the interbasin heat exchange between the Atlantic and Southern Oceans [Dias et al. (2020); Garuba and Klinger (2016); Sun et al. (2020)]. Meanwhile, an anomalous clockwise ocean circulation is generated in the Indo-Pacific through a geostrophic response to the AMOC slowdown [Garuba and Klinger (2016); Sun et al. (2020); Li and Liu (2022); Sun et al. (2022)], which largely accounts for the OHT change across the boundary between the Indo-Pacific and Southern Oceans [Garuba and Klinger (2016); Li and Liu (2022); Sun et al. (2022)].

Unlike greenhouse gases, the impacts of aerosols on global OHU, redistribution and storage have received less attention, and thus their patterns and the working physical processes remain unclear. Here we exploit historical aerosol and greenhouse gas single-forcing experiments (Gillett et al. 2016) with Coupled Model Intercomparison Projects Phase 5/6 (CMIP5/6) models to isolate and quantify the impacts of anthropogenic aerosols and greenhouse gases on global ocean heat uptake, redistribution and storage and explore the underlying physical mechanism under either forcer.

3.2 Methods

3.2.1 CMIP5 and CMIP6 model simulations

We adopt 10 CMIP5 models and 10 CMIP6 models (Table B1) that are forced only by historical anthropogenic aerosol (HIST-AER) or greenhouse gas (HIST-GHG) changes. The aerosol-only experiments with 10 CMIP5 models were identified as "historicalMisc" in the CMIP5. Here, we name them "HIST-AER" for the consistence with CMIP6 aerosol-only experiments. The other CMIP5 model is CESM1-CN, in the version of T31_gx3v7 (Li and Liu 2022). We force this model following the CMIP5 protocol to generate the HIST-AER and HIST-GHG simulations and produce three ensemble members for either simulation. Also, we employ the pre-industrial control and historical simulations with the 20 CMIP5/6 models (Table B1). For each model, we probe the last 500-year output of pre-industrial control (piControl) simulation and the ensemble mean of the historical simulation (HIST) over 1861-2005, a period during which data are available from all the models. Based on the ensemble means of these models, we also compute the multi-model mean and inter-model spread (one standard deviation). Besides, we construct a 8-model ensemble from the 20 CMIP5/6 models, since all the variables needed for the ocean heat budget analysis are available in these 8 models (CanESM5, CESM1-CN, CNRM-CM6-1, CSIRO-Mk3-6-0, GISS-E2-1-G, HadGEM3-GC31-LL, IPSL-CM6A-LR and NorESM2-LM, see Table B1).

The CMIP5/6 HIST-AER and HIST-GHG simulations display generally consistent patterns of OHU, OHS and North Atlantic cooling (warming) hole while also indicate some detailed differences (Figure B5-7). For example, compared to the CMIP5 models, the CMIP6 models simulate a larger reduction of OHU in the subpolar North Atlantic when driven by anthropogenic aerosols, and enhanced OHU in a more eastward location in the subpolar North Atlantic when driven by anthropogenic greenhouse gases (Figure B5). Zonally integrated OHU changes reveal that the CMIP6 models simulate a much larger aerosol-driven OHU decrease in the Northern Hemisphere oceans than the CMIP5 models (Figure B6), which is consistent with the stronger aerosol cooling in the former models. When we compare the zonally integrated aerosol- and greenhouse gas-driven OHU changes, we discover that aerosol-driven OHU decrease overweighs greenhouse gas-driven OHU increase between 40°N and 60°N during 1861-2005 in the CMIP6 models, which leads to an OHU decrease seen from the sum of the two OHU changes (Figure B6). The opposite is true for the CMIP5 models (Figure B6).

Additionally, we employ the SSP245 simulation and accompanying aerosol-only (SSP245-AER) and greenhouse-gas-only (SSP245-GHG) single forcing experiments with four CMIP6 models (CanESM5, GISS-E2-1-G, MIROC6 and NorESM2-LM, see Table B2) spanning from 2021 to 2100. We

examine the multi-model mean changes in these simulations relative to the preindustrial state.

3.2.2 Observational ocean temperature datasets

To evaluate the creditability of the CMIP5 and CMIP6 models in simulating historical oceanic heat changes, we construct a 6-member ensemble of observational datasets by including four objectively analyzed ocean datasets: the DePreSys ocean temperature analysis (Smith and Murphy 2007), the EN4 (version 4.2.2) ocean temperature analysis (Good et al. 2013), the Institute of Atmospheric Physics (IAP) ocean temperature analysis (Cheng et al. 2017) and the subsurface temperature analyses led by Ishii [version 7.3.1; Ishii et al. (2005)], and two ocean reanalysis products, the German contribution to the Estimating the Circulation and Climate of the Ocean project version 3 (GECCO3) ocean synthesis (Köhl 2020) and the Ocean Reanalysis System 4 [ORAS4; Balmaseda et al. (2013)] from European Centre for Medium-Range Weather Forecasts. The DePreSys ocean temperature analysis has a horizontal resolution of 1.25° with 20 vertical levels on a full-depth ocean and spans from 1950 to 2006. The EN4 ocean temperature analysis has a horizontal resolution of 1° with 42 vertical levels on a full-depth ocean and spans from 1900 to the present. There are four versions of EN4 data available: Gouretski and Reseghetti (2010) XBT corrections and Gouretski and Cheng (2020) MBT

corrections, Levitus et al. (2009) corrections, Cowley et al. (2013) XBT corrections and Levitus et al. (2009) MBT corrections, and Cheng et al. (2014) XBT corrections and Gouretski and Cheng (2020) MBT corrections. We use the average of the four versions to represent the EN4 data. The IAP ocean temperature analysis has a horizontal resolution of 1° with 41 vertical levels from surface down to 2000m and spans from 1940 to the present. The subsurface temperature analyses led by Ishii has a horizontal resolution of 1° with 28 vertical levels from surface down to 3000m and spans from 1955 to the present. The GECCO3 is based on the Massachusetts Institute of Technology general circulation model, which has a nominally 0.4° resolution horizontal resolution and 40 vertical levels on a full-depth ocean and spans from 1948 to 2018. The ORAS4 has a global ocean coverage of 1° horizontal resolution with 42 vertical levels on a full-depth ocean and spans from 1958 to 2017. We focus on the OHC during the period of 1960-2005 when data are available from all the observational datasets as well as the CMIP5/6 model historical simulations. We calculate the ensemble mean of the observational datasets and estimate the observation uncertainty using one standard deviation among the observational datasets.

3.2.3 Significance of observation and model simulation results

We conduct Student's t-test for the upper 2000m OHC trends during 1960-2005 in the Atlantic, Indo-Pacific and Southern Oceans to determine if there is a statistically significant difference between the means of the two groups: 6 observation datasets and 10 CMIP5 models, or 6 observation datasets and 10 CMIP6 models. We find the p-value is larger than 0.05 in any of the above tests, which indicates that there is no statistically significant difference in oceanic heat changes between observations and CMIP5/6 models at the 95% confidence interval.

3.2.4 Ocean heat budget analysis

We analyze the ocean heat budget in each ocean basin that links ocean heat uptake, transport and storage [Liu et al. (2020); Li and Liu (2022); Liu et al. (2018)]. The zonally integrated full-depth oceanic heat budget at certain latitude is

$$\int_{X_W}^{X_E}\int_{-H}^{0}\rho_0 C_P\frac{\partial\theta}{\partial t}dzdx+\int_{X_W}^{X_E}\int_{-H}^{0}\rho_0 C_P[\nabla\cdot(\boldsymbol{v}\theta+D)]dzdx=\int_{X_W}^{X_E}(SHF)dx \quad (3.1)$$

where X_W and X_E denote the longitudes of the western and eastern boundaries of the basin at certain latitude, ρ_0 is seawater density, C_P is the specific heat of sea water, θ is potential temperature of sea water, $-H$ denotes the depth of ocean bottom. SHF denotes the net surface heat flux. ∇ and $\boldsymbol{v}$ are three-dimensional gradient operator and velocity. $\boldsymbol{v}=\overline{\boldsymbol{v}}+\boldsymbol{v}^*$ where $\overline{\boldsymbol{v}}$ denotes

Eulerian-mean velocity and $\boldsymbol{v}^*$ denotes the sum of meso- and sub-mesoscale eddy-induced velocity. D denotes diffusion and other sub-grid processes.

Based on Eq. (3.1), we define ocean heat content (OHC) as:

$$OHC = \int_{X_W}^{X_E} \int_{-H}^{0} \rho_0 C_P \theta dz dx \tag{3.2}$$

and OHC tendency as ocean heat storage, i.e.,

$$OHS = \frac{\partial}{\partial t} OHC = \frac{\partial}{\partial t} \int_{X_W}^{X_E} \int_{-H}^{0} \rho_0 C_P \theta dz dx \tag{3.3}$$

and ocean heat uptake as:

$$OHU = \int_{X_W}^{X_E} (SHF) dx \tag{3.4}$$

and meridional ocean heat transport as:

$$OHT = \int_{X_W}^{X_E} \int_{-H}^{0} \rho_0 C_P (\overline{\boldsymbol{v}}\theta + \boldsymbol{v}^*\theta + D) dz dx \tag{3.5}$$

which shows that meridional ocean heat transports can be induced by Eulerian-mean flow, eddies and diffusion.

Therefore, the heat budget by Eq. (3.1) can be written as

$$OHS = OHU - \frac{\partial}{\partial y} OHT \tag{3.6}$$

which indicates that ocean heat storage is determined by heat uptake from atmosphere-ocean interface and heat redistribution in form of the meridional gradient of ocean heat transport. Here, $-\frac{\partial}{\partial \mathrm{y}}\mathrm{OHT}$ could be related to the changes in ocean circulations—such as the AMOC—and resultant meridional convergence or divergence of oceanic heat transport.

Accordingly, the basin integrated full-depth oceanic heat budget is

$$[OHS] = [OHU] - (OHT_N - OHT_S) \quad (3.7)$$

where [.] denotes a basin integration, OHT_N and OHT_S denote the ocean heat transports across the northern and southern boundaries of the basin.

Relative to the preindustrial time, the anthropogenic aerosol- or greenhouse gas-driven changes in the zonally integrated full-depth oceanic heat budget at certain latitude during 1861-2005 are defined as:

$$\Delta OHS = \Delta OHU - \Delta\left(\frac{\partial}{\partial y} OHT\right) \quad (3.8)$$

where Δ refers to the differences between the HIST-AER/HIST-GHG experiment and the preindustrial control run. ΔOHS can be represented by the change in the OHC trend [ΔTr(OHC)] that is defined as:

$$\Delta Tr(OHC) = Tr(OHC) - Tr(OHC_{ctrl}) \quad (3.9)$$

where Tr(OHC) and Tr(OHC_{ctrl}) denote the OHC trends in the HIST-AER/HIST-GHG simulation and preindustrial control run with CMIP5/6 models. Tr(OHC_{ctrl}) may reflect a temperature drift in the preindustrial control run, which is not necessarily zero [Gupta et al. (2013); Irving et al. (2021)] and can persist in the HIST-AER and HIST-GHG simulations. The difference between Tr(OHC) and Tr(OHC_{ctrl}) facilitates a cancellation of the drifts between the HIST-AER/HIST-GHG simulation and preindustrial control run and hence a reduction of the effect of drifts on the OHC trend in the HIST-AER/HIST-GHG simulation.

Similarly, the anthropogenic aerosol- or greenhouse gas-driven changes in the basin integrated full-depth oceanic heat budget can be written as:

$$\Delta[OHS] = \Delta[OHU] - (\Delta OHT_N - \Delta OHT_S) \quad (3.10)$$

We further decompose the Eulerian mean OHT change into the component that is driven by ocean circulation anomaly ($\overline{\mathrm{OHT}}_{\mathrm{v}'}$) and the component that is driven by ocean temperature anomaly ($\overline{\mathrm{OHT}}_{\theta'}$), such as

$$\overline{OHT}_{v'} = \iint \rho_0 C_P \boldsymbol{v}' \bar{\theta}_0 dz dx \quad (3.11)$$

where $\boldsymbol{v}'$ denotes the change in monthly Eulerian-mean velocity and θ_0 denotes the monthly climatological ocean temperature in the preindustrial control run.

$$\overline{OHT}_{\theta'} = \iint \rho_0 C_P \bar{\boldsymbol{v}}_0 \theta' dz dx \quad (3.12)$$

where θ' denotes the change in monthly ocean temperature and $\bar{\mathbf{v}}_0$ denotes the monthly climatological Eulerian-mean velocity in the preindustrial control run. It is worth noting that the above approach (Eqs. 3.11-12) may not serve as a strict decomposition of ocean circulation- and temperature-driven components given that the anthropogenic temperature signal may not appear as a quasi-passive tracer in some regions, which potentially contributes to the large uncertainties as shown in Figure 3.4.

3.2.5 Southern Ocean MOCs

The Eulerian-mean MOC ($\bar{\psi}$) or the "Deacon Cell" is computed through the zonal and vertical integrations of the Eulerian-mean meridional velocity v:

$$\bar{\psi} = \oint \int_z^0 \bar{v} dz' dx \tag{3.13}$$

The eddy-induced MOC (ψ^*) is computed through the zonal and vertical integrations of the meso- and sub-mesoscale eddy-induced meridional velocity v^*:

$$\psi^* = \oint \int_z^0 v^* dz' dx \tag{3.14}$$

The residual MOC (ψ_{res}) is calculated as:

$$\psi_{res} = \bar{\psi} + \psi^* \tag{3.15}$$

3.3 Results

3.3.1 Aerosol and greenhouse gas driven oceanic heat changes

We examine the OHU changes over 1861-2005 relative to the preindustrial time in the aerosol-only and greenhouse-gas-only simulations with a 8-model ensemble of CMIP5/6 models (Methods). The multi-model mean shows that the increasing emissions and concentrations of anthropogenic aerosols between 1861 and 2005 lead to an OHU decrease in the North Atlantic subpolar region (Figure 3.1a). Compared to aerosol effects, anthropogenic greenhouse gas increases generally have an opposite effect on OHU during this

period. In the subpolar North Atlantic, the greenhouse gas-induced OHU increase acts to offset the aerosol-induced OHU decrease (Figure 3.1b).

Meanwhile, we look into the trend of the vertically integrated ocean heat content (OHC) over 1861-2005, or equivalently, the ocean heat storage (OHS). We find a different pattern of OHS from OHU. Anthropogenic aerosols drive reduced OHS over global oceans except for a few sites such as the subpolar North Atlantic where OHU decreases but OHS increases (Figure 3.1c) primarily owing to a strengthened AMOC and associated heat transport there (Ma et al. 2020). Similarly, the rising anthropogenic greenhouse gases lead to enhanced OHS over most of global oceans but reduced OHS in the subpolar North Atlantic despite OHU increases there (Figure. 3.1d), which is related to a weakened AMOC (Liu et al. 2020). Under either anthropogenic aerosol or greenhouse gas forcing, the contrary changes between OHU and OHS in the subpolar North Atlantic manifest the turbulent heat flux feedback [Shi et al. (2018); Liu et al. (SA 2020); Gillett et al. (2016); Zhang and Cooke (2021)] or North Atlantic redistribution feedback (Couldrey et al. 2021) via the North Atlantic cooling (for aerosols)/warming (for greenhouse gases) hole (Figure B1a,b), and implies heat redistribution by ocean circulation change. Anthropogenic aerosol (greenhouse gas) forcing perturbs the climate system and initializes the feedback that involves an AMOC strengthening (weakening), a meridional convergence (divergence) of oceanic heat transport and

diminished (enhanced) OHU in the subpolar North Atlantic [Ma et al. (2020); Liu et al. (2020)].

To elaborate on the anthropogenic aerosol and greenhouse gas effects on ocean heat redistribution, we conduct a heat budget analysis that links OHU, meridional OHT and OHS [Methods; Liu et al. (2020); Winton et al. (2013)]. We find that anthropogenic aerosols bring about an anomalous oceanic heat convergence [$-\partial(\mathrm{OHT})/\partial y>0$] over 31°N-70°N and divergence [$-\partial(\mathrm{OHT})/\partial y<0$] in the rest of the Atlantic (Figure 3.2a). The former heat convergence acts to warm the subpolar North Atlantic, which overweighs the cooling due to an anomalous heat loss via ocean surface and hence allows for heat stored in the subpolar North Atlantic. The latter heat divergence primarily accounts for the abated heat storage in the rest of the Atlantic. On the contrary, anthropogenic greenhouse gases induce an anomalous oceanic heat divergence to the north of 32°N and convergence to the south (Figure 3.2b). The former heat divergence overweighs the surface heat uptake in the subpolar North Atlantic and results in diminished heat storage there. The latter heat convergence explains the mounting heat stored in the rest of the Atlantic. It merits attention that aerosol-induced changes in OHU and $-\partial(\mathrm{OHT})/\partial y$ are about twice the magnitude of those induced by greenhouse gases over the subpolar North Atlantic. This is possibly because a majority of the models in the heat budget analysis here (Methods) come from the CMIP6 in which aerosols impose a

stronger impact on ocean circulations such as the AMOC than greenhouse gases during the historical period (Menary et al. 2020).

Oceanic heat redistribution due to anthropogenic aerosols and greenhouse gases is not limited to the Atlantic but also extends to other ocean basins via inter-basin heat exchanges. We first probe the OHT change across the boundary between the Atlantic and Southern Oceans. Especially, driven by anthropogenic aerosols, changes in ocean circulations such as the AMOC strengthening (Figure 3.3a) cause an increase of the northward OHT across the boundary between Atlantic and Southern Oceans (30°S) by 31.79±19.32 TW (1TW = 10^{12} Watt) (Figure 3.4a). This circulation-induced OHT increase is slightly compensated by a temperature-induced OHT decrease (Methods) primarily due to the cooling in surface waters (Figure 3.3a), leading to a net anomalous northward OHT of 25.39±18.31 TW (Figure 3.4a). On the other hand, under the rising greenhouse gases, ocean circulation changes such as the AMOC weakening (Figure 3.3b) reduce the northward OHT by 6.00±14.95 TW, which is almost completely compensated by a temperature-induced OHT increase mainly owing to the warming in surface waters (Figure 3.3b), and result in a very small net anomalous southward OHT of 0.05±11.99 TW (Figure 3.4b). This anomalous OHT is much smaller in magnitude than its counterpart due to anthropogenic aerosols, and meanwhile, exhibits large uncertainty.

Inter-basin heat exchanges also occur between the Indo-Pacific and Southern Oceans. As a part of global adjustment of ocean thermocline [Sun et al. (2020); Huang et al. (2000)] in response to anthropogenic aerosol forcing, an anomalous anticlockwise ocean circulation is generated in the Indo-Pacific basin [Figure 3.3c; Newsom and Thompson (2018); Talley (2013)]. This anomalous ocean circulation produces a southward OHT across the boundary between the Indo-Pacific and Southern Oceans (Figure 3.4c). Since the ocean circulation-driven OHT component is only slightly compensated by a temperature-driven OHT component, a large amount of anomalous ocean heat is exported from the Indo-Pacific to the Southern Ocean. On the other hand, in response to anthropogenic greenhouse gases, an anomalous clockwise ocean circulation is formed over the Indo-Pacific (Figure 3.3d), which generates an anomalous northward OHT across the boundary between the Indo-Pacific and Southern Oceans. A majority of this ocean circulation-induced OHT anomaly is offset by a temperature-induced southward OHT anomaly. Therefore, the Southern Ocean exports a smaller amount of heat into the Indo-Pacific than that under the aerosol-driven scenario (Figure 3.4d).

We delve into the change in oceanic heat over the Southern Ocean that connects both Atlantic and Indo-Pacific Oceans. Relative to the preindustrial time, anthropogenic aerosols bring on a dipole-like change in OHU (Figure 3.2e) in which the ocean releases heat (presents negative net surface heat flux

anomalies) to the south of 45°S but takes heat (presents positive net surface heat flux anomalies) to the north between 1861 and 2005. Most of the taken heat is further redistributed by ocean circulations in the form of anomalous OHT convergence in 46°S-63°S and anomalous OHT divergence to the north of 46°S. As a result, OHS shows negative anomalies almost over the Southern Ocean with slight positive anomalies between 49°S and 51°S. Consistent with the OHS changes, we find that aerosol changes induce a wide-spreading cooling in the Southern Ocean peaking at -0.03 K/decade (Figure 3.3e). Such Southern Ocean cooling may be attributed to the aerosol forcing located in the tropical regions, dominated by East/South Asia (Shi et al. 2022). Note here, the heat redistribution or OHT anomalies could be achieved either via the climatological MOC carrying ocean temperature anomalies or via MOC anomalies acting on the climatological ocean temperature [Zanna et al. (2019); Rathore et al. (2020); Winton et al. (2013); Garuba and Klinger (2016); Couldrey et al. (2021); Marshall et al. (2015); Banks and Grogery (2006); Chen, H. et al. (2019)]. Particularly, anthropogenic aerosols drive an equatorward-weakened residual MOC in the Southern Ocean (Figure 3.3e). This is because Southern Hemisphere westerly winds displace equatorward and become weaker in response to anthropogenic aerosols [Figure B2a; Rotstayn et al. (2013); Wang et al. (2020)]. The wind-driven Deacon cell accordingly becomes equatorward weakened and is partially compensated by the changes in the

eddy-induced MOC (Methods), which leads to an equatorward-weakened residual MOC in the Southern Ocean (Figure B3a,c,e).

In contrast to aerosols, anthropogenic greenhouse gases engender poleward intensified Southern Hemisphere westerly winds [Figure B2b; Fyfe et al. (2007)] and hence a poleward intensified wind-driven Deacon Cell. The latter is partially compensated by eddy-induced MOC between 45°S-53°S, resulting in a poleward shifted and strengthened residual MOC (Figure B3b,d,f). Relative to the preindustrial time, anthropogenic greenhouse gases generally promote Southern Ocean OHU in a peak at 55°S (Figure 3.2f). Meanwhile, OHT diverges in 49°S-69°S and converges in 36°S-48°S. With combined effects of OHU and heat redistribution, OHS exhibits positive anomalies over the Southern Ocean peaking at 43°S. The greenhouse gases induced positive OHS anomalies manifest a subsurface warming in the Southern Ocean with a marked downward warming tongue between 35°S and 55°S (Figure 3.3f). It merits attention that other external forcers, such as stratospheric ozone depletion and tropospheric ozone increases, can also drive the interior Southern Ocean warming during the twentieth century [Swart et al. (2018); Li S. et al. (2021); Liu et al. (2022)].

We further explore the changes in the basin-integrated ocean heat budget during 1861-2005 relative to the preindustrial time. Driven by anthropogenic aerosols, the Atlantic receives heat from both the Southern and

Arctic Oceans at rates of 25.39±18.31 TW and 2.90±26.54 TW, and meanwhile, loses heat at a rate of 38.29±25.46 TW via ocean surface, which leads to reduced heat storage at a rate of 10.00±17.05 TW (Figure 3.5a). On the other hand, driven by anthropogenic greenhouse gas forcing, the Atlantic imports heat at rates of 1.72±11.52 TW from the Arctic but exports heat at a rate of 0.05±11.99 TW to the Southern Ocean, and takes heat at a rate of 30.84±12.60 TW from the atmosphere, which results in an increase of the heat storage at a rate of 32.02±6.04 TW (Figure 3.5b).

For the Indo-Pacific Oceans, they import heat at a rate of 1.56±2.28 TW from the Arctic Ocean but export heat at a rate of 27.03±20.86 TW to the Southern Ocean under anthropogenic aerosol forcing. Meanwhile, the oceans lose heat at a rate of 18.63±15.11 TW via ocean surface and hence have a decline of heat storage at a rate of 44.13±19.77 TW (Figure 3.5a). By contrast, the Indo-Pacific Oceans export heat at a rate of 1.00±1.15 TW to the Arctic but import heat at a rate of 10.94±8.39 TW from the Southern Ocean under anthropogenic greenhouse gas forcing. The integrated OHU over the basins amounts to 34.64±10.40 TW and an increase of heat storage at a rate of 44.62±9.91 TW ensues (Figure 3.5b).

Driven by anthropogenic aerosols, the Southern Ocean loses heat at a rate of 17.62±17.01 TW via ocean surface. It also has a net heat import of 1.64±11.37 TW from the north and a heat export of 0.24±2.90 TW to the

marginal seas around Antarctica such that the stored heat within the basin diminishes at a rate of 16.21±15.36 TW (Figure 3.5a). While driven by anthropogenic greenhouse gases, the Southern Ocean takes heat at a rate of 59.38±16.30 TW from the atmosphere, exports heat of 10.89±12.99 TW to the north and imports heat at a rate of 0.52±4.66 TW from the marginal seas in the south. As a result, the basin has an increase of the stored heat at a rate of 49.47±16.67 TW (Figure 3.5b).

3.3.2 Observational constraints on simulated ocean heat changes

Compared to CMIP5 models, CMIP6 models have been suggested to produce a stronger aerosol cooling [Dittus et al. (2020); Flynn and Mauritsen (2020); Zhang et al. (2021)] and a resultant stronger increase in the AMOC strength during the historical period [Menary et al. (2020); Hassan et al. (2021)]. Also, CMIP6 models include more sophisticated aerosol indirect effects on cloud microphysics (Wyser et al. 2020), which modulate the cloud forcing and potentially relate to a much higher climate sensitivity in these models [Meehl et al. (2020); Zelinka et al. (2020)]. Recently, the systematic CMIP6 model biases in surface ocean heat uptake have been isolated via a novel tracer-percentile framework as compared to observations (Sohail et al. 2021). In this context, to assess the creditability of CMIP5 and CMIP6 models in

simulating oceanic heat changes, we resort to observed OHC change for constraints on model results.

We examine the upper 2000m OHC changes relative to the 1960-1969 average from 6 observational datasets and from historical simulations with 10 CMIP5 models and 10 CMIP6 models (Methods) over individual oceans between 1960 and 2005 (Figure. 3.6). In the Atlantic, the observed, CMIP5 and CMIP6 model OHC trends are 0.96±0.43 ZJ/year, 1.09±0.76 ZJ/year and 0.48±0.74 ZJ/year (1ZJ = 10^{21} Joule), indicative of the CMIP5 models simulating an oceanic heat increase closer to the observations within this basin (Figure 3.6b). On the other hand, the observed, CMIP5 and CMIP6 model OHC trends are 0.55±0.71 ZJ/year, 1.40±1.01 ZJ/year and 0.22±0.70 ZJ/year in the Indo-Pacific where the observed trend is between the simulated by CMIP5 and CMIP6 models (Figure 3.6d). Over the Southern Ocean, the observed, CMIP5 and CMIP6 model OHC trends are 1.29±0.33 ZJ/year, 1.85±0.87 ZJ/year and 1.12±0.48 ZJ/year, meaning that the CMIP6 models simulate an oceanic heat increase closer to the observations in this basin (Figure 3.6f). Overall, albeit more of the CMIP6 models include the more sophisticated aerosol indirect effects than the CMIP5 models, they do not necessarily have a better performance than the CMIP5 models in simulating historical ocean heat uptake and storage. We can see CMIP6 models generally exhibit a stronger aerosol cooling effect than CMIP5 models in terms of OHC trends in all three

basins (Figure 3.6b,d,f), but there is no statistically significant difference in oceanic heat changes between observations and CMIP5/6 models (Methods). This result suggests that our estimate of oceanic warming from both CMIP5 and CMIP6 model simulations are plausible and under the constraint of observations when considering observation uncertainties.

3.4 Conclusion and discussion

To summarize, we find that anthropogenic aerosols and greenhouse gases have caused heat uptake, redistribution and storage over global oceans via different mechanisms between 1861 and 2005. Driven by anthropogenic aerosols, the Southern Ocean imports heat from the Indo-Pacific but exports heat into the Atlantic, accompanying with reduced OHU in the subpolar Atlantic. Alterations in ocean circulation and ocean temperature have a weak compensation in contributing to interbasin OHT changes. As a result, interbasin OHT changes are comparable to basin-integration OHU changes for the Atlantic and Indo-Pacific Oceans, meaning that both factors play important roles in altering OHS in these ocean basins. Nevertheless, as driven by anthropogenic greenhouse gases, excessive atmospheric heat enters the subpolar Atlantic while the Southern Ocean imports heat from the Atlantic but exports heat into the Indo-Pacific. Compared to aerosol forcing, alterations in ocean circulation and ocean temperature have a much stronger compensation

between their contributions to interbasin OHT changes under greenhouse gas forcing. Thereby, under the rising anthropogenic greenhouse gases, interbasin OHT changes are far smaller than basin-integration OHU changes such that the latter dominate the OHS changes over individual basins.

One may also note the evolution of the roles of anthropogenic aerosols and greenhouse gases in modulating global ocean heat uptake and storage in future climate. For example, following one possible shared socio-economic pathway (SSP245), anthropogenic greenhouse gases could impose much stronger impacts than aerosols on OHU and OHC trends over 2021-2100 (Figure B4). Given the distinct trajectories of anthropogenic aerosols and greenhouse gases in various SSPs, the impacts of both forcers on global ocean heat uptake and storage, could vary from historical to future climate, or between different SSP scenarios.

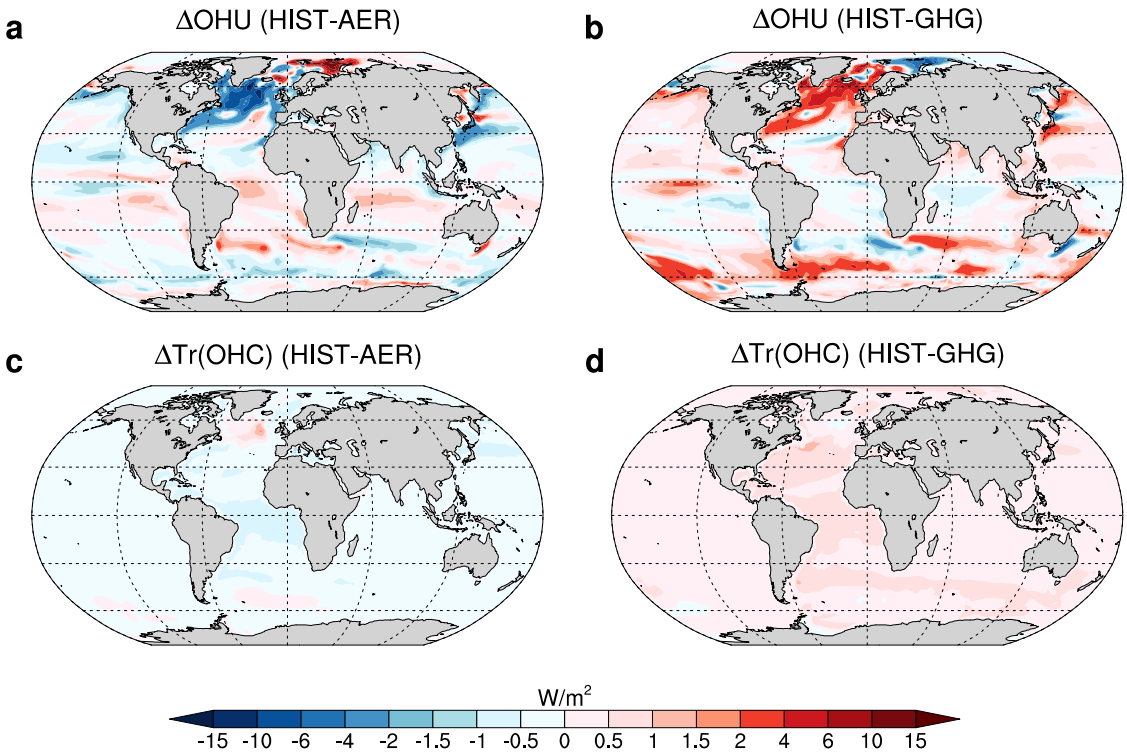

Figure 3.1: Anthropogenic aerosol and greenhouse gas driven changes in OHU and OHC trend. (a,b) Annual mean changes (relative to the preindustrial time) in global OHU during 1861-2005 (shading) for the multi-model means of the 8-model ensemble (a) HIST-AER and (b) HIST-GHG simulations. (c,d) As in (a,b) for the changes in the full-depth integrated annual mean OHC trend during 1861-2005.

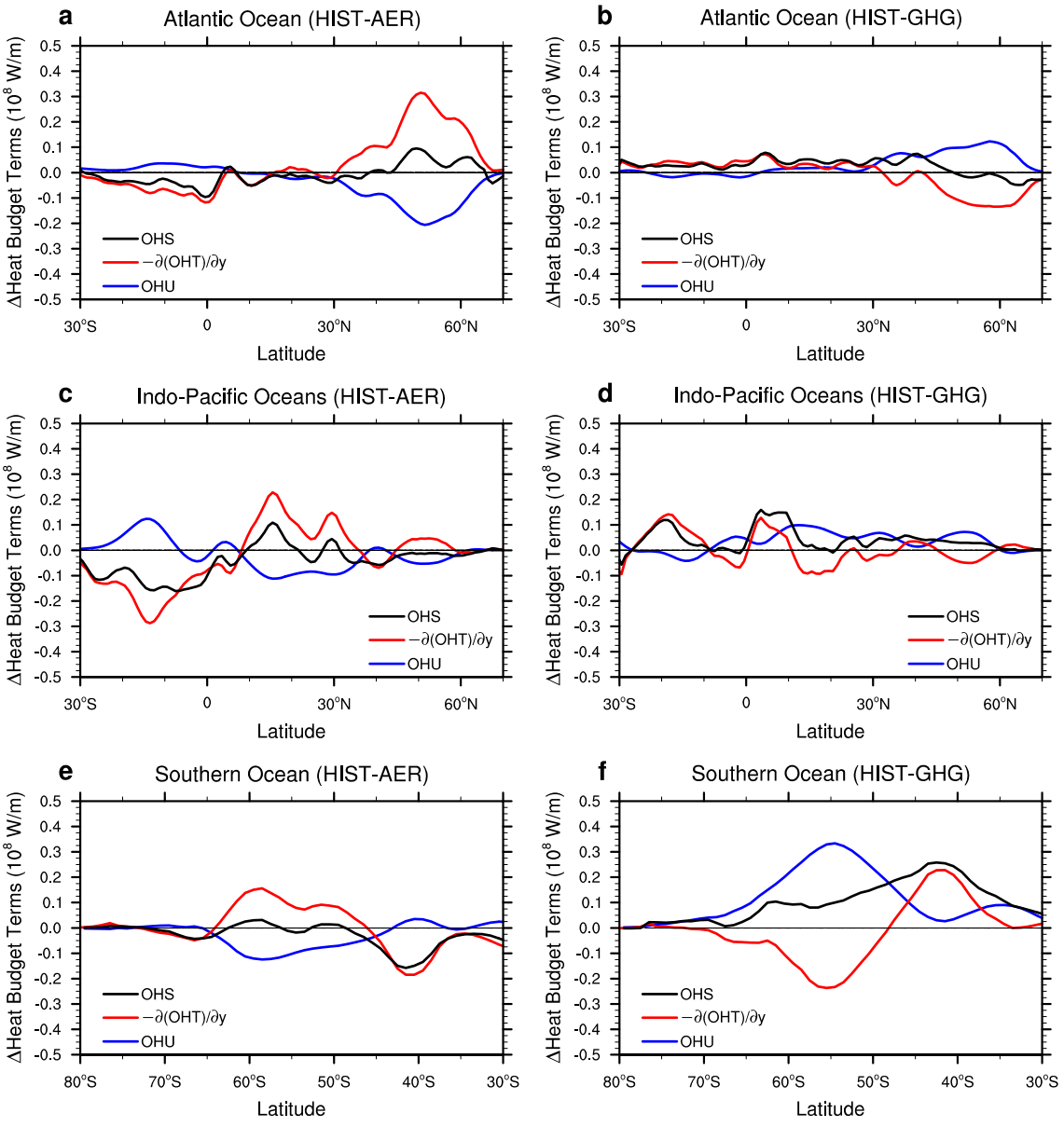

Figure 3.2: Anthropogenic aerosol and greenhouse gas driven changes in oceanic heat budgets for individual basins. (a,c,e) Annual mean changes (relative to the preindustrial time) in the zonally integrated full-depth oceanic heat budget over 1861-2005: OHU (multi-model mean, blue), -∂ (OHT)/∂y (multi-model mean, red) and OHS (multi-model mean, black) in the (a) Atlantic, (c) Indo-Pacific and (e) Southern Oceans for the 8-model ensemble HIST-AER simulation. (b,d,f) are as in (a,c,e) but for 8-model ensemble HIST-GHG simulation.

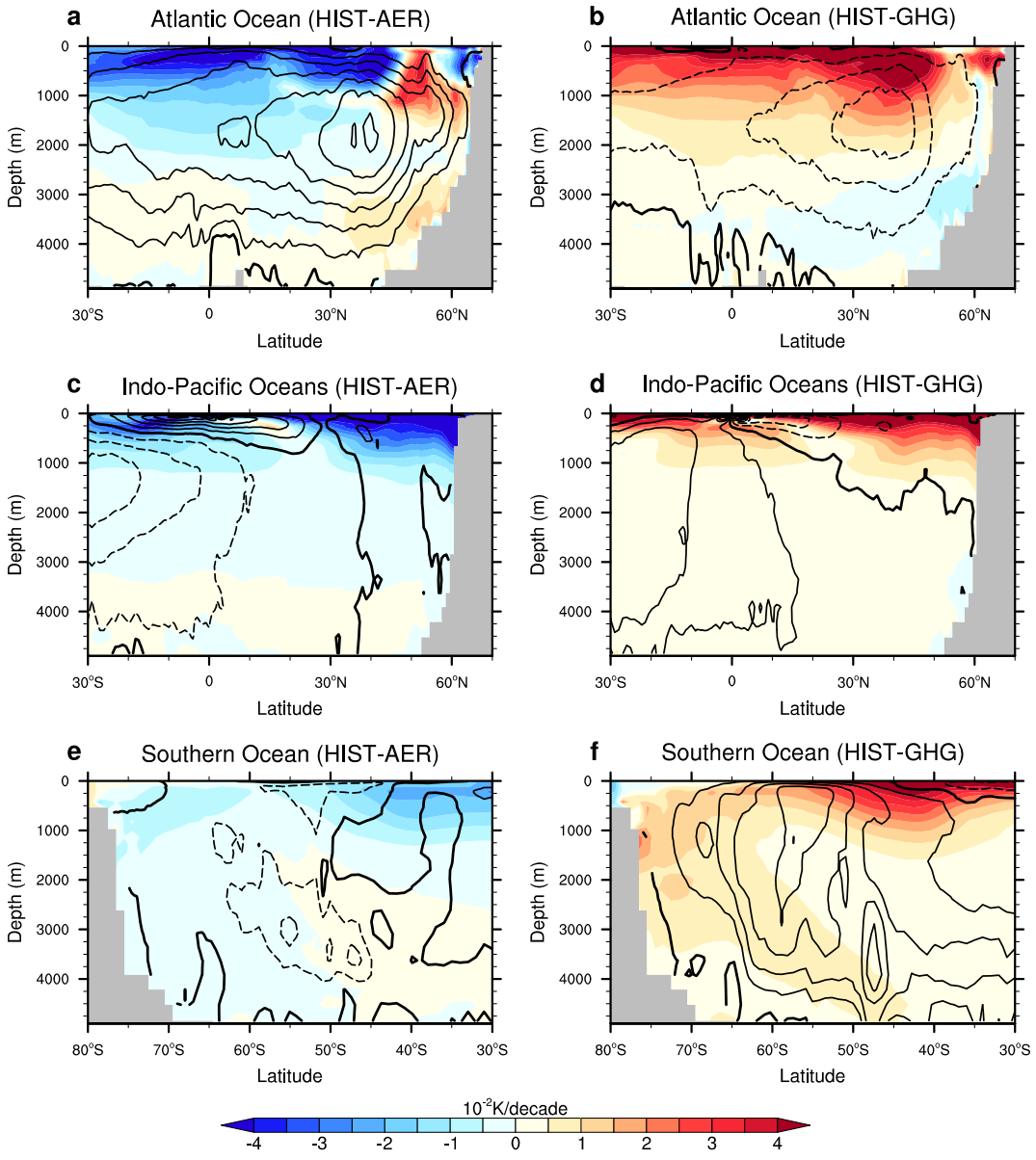

Figure 3.3: Anthropogenic aerosol and greenhouse gas driven ocean temperature and MOC changes over individual basins. (a,c,e) Changes (relative to the preindustrial time) in the annual and zonal mean temperature trend over 1861-2005 (color shading in 10^{-2} K/decade) in the (a) Atlantic, (c) Indo-Pacific and (e) Southern Oceans for the multi-model mean of the 8-model ensemble HIST-AER simulation. Changes in the annual mean Eulerian mean plus eddy-induced MOC is overlapped for each basin [contour with interval of 0.2 Sv (1 Sv = 10^6 m^3/s), zero contours thickened, solid positive and dashed negative]. (b,d,f) As in (a,c,e) but for the 9-model ensemble HIST-GHG simulation.

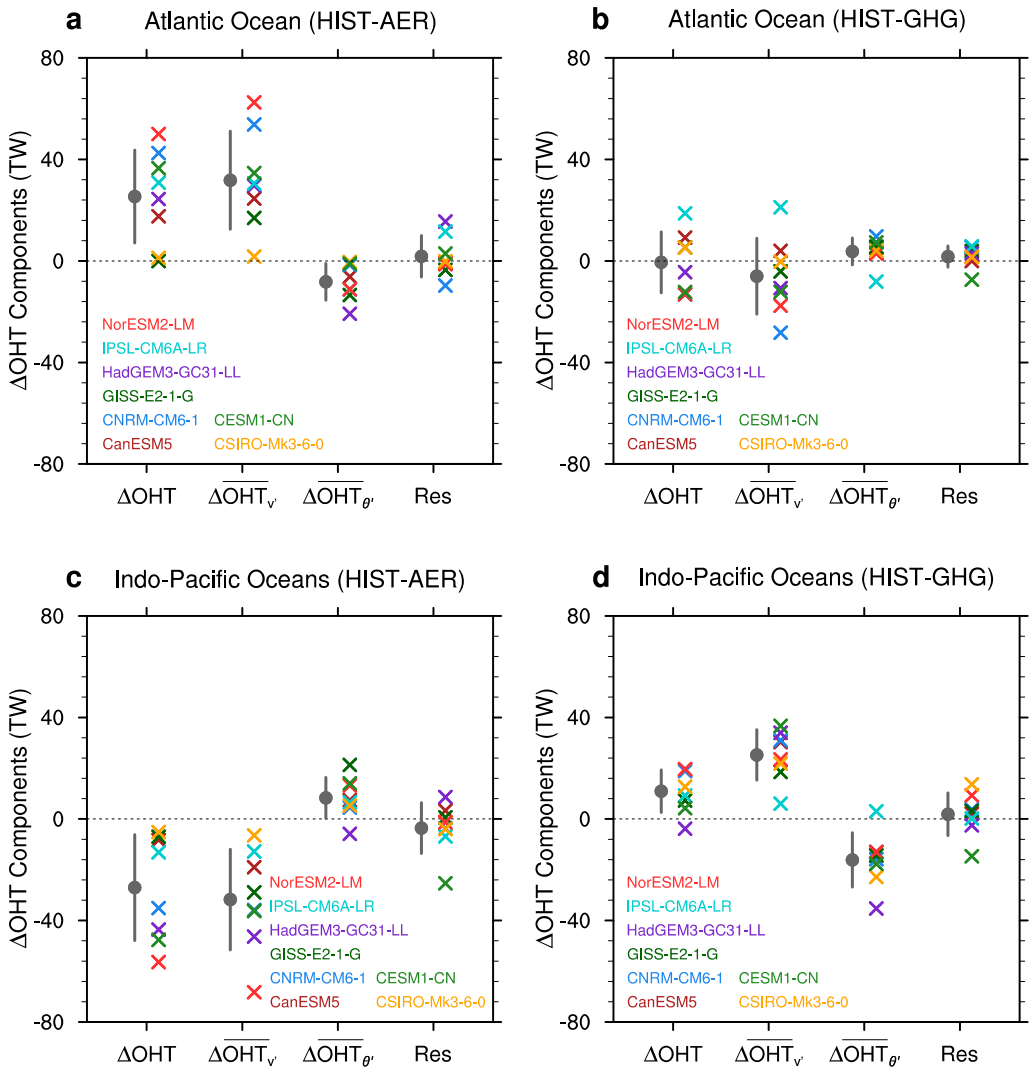

Figure 3.4: Decompositions of anthropogenic aerosol and greenhouse gas driven interbasin heat exchanges. (a,c) Annual mean changes (relative to the preindustrial time) in the meridional OHT (ΔOHT), the components due to ocean circulation alteration ($\Delta\overline{OHT}_{\theta'}$) and ocean temperature alteration ($\Delta\overline{OHT}_{v'}$) and the residual term (Res) due to the effects of eddies, diffusion and the nonlinearity resulting from ocean circulation and temperature changes across the boundaries (a) between the Atlantic and the Southern Oceans and (c) between the Indo-Pacific and the Southern Oceans during 1861-2005 from the 8-model ensemble HIST-AER simulation. (b,d) As in (a,c) but for the 8-model ensemble HIST-GHG simulation. Results are shown in multi-model mean (dot) ± one standard deviation among models (bars) as well as for each model (colored cross). Positive (negative) values indicate anomalous northward (southward) ocean heat transport.

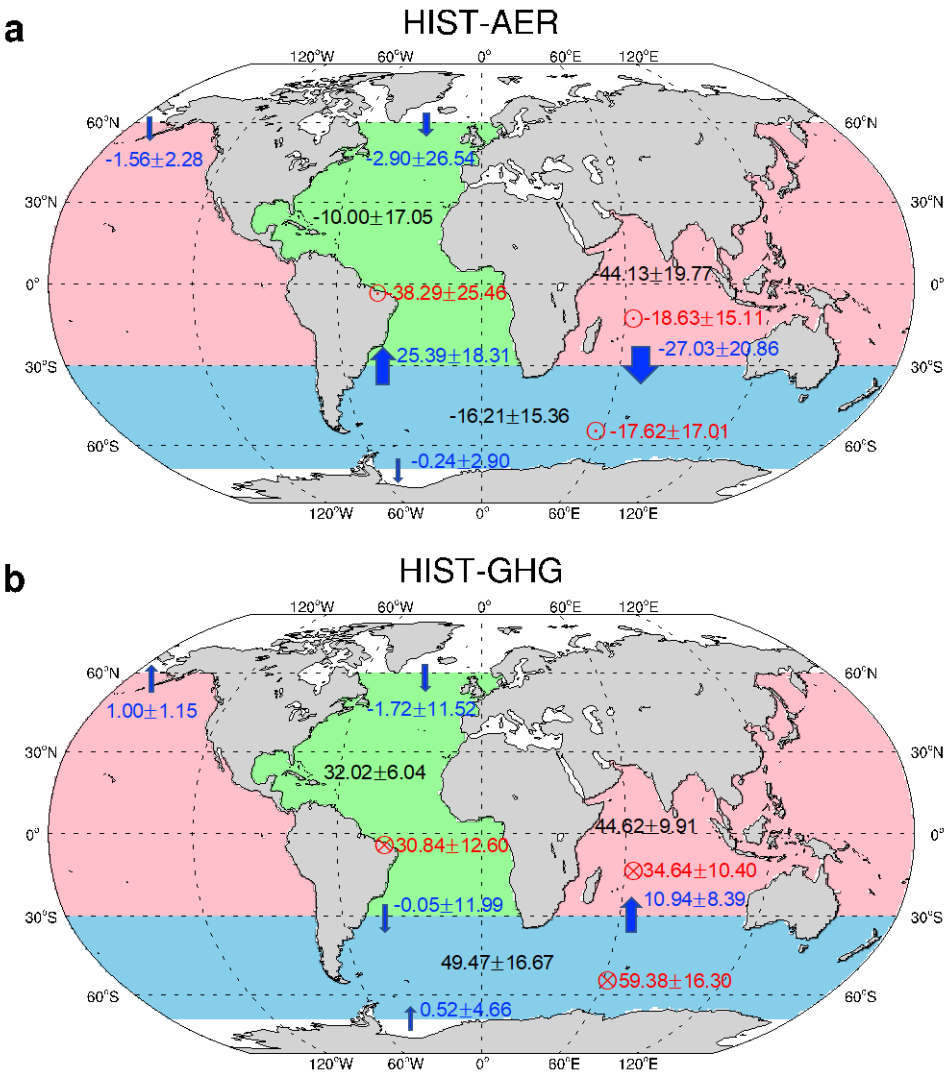

Figure 3.5: Anthropogenic aerosol and greenhouse gas driven changes in basin integrated oceanic heat budgets. Ocean basins defined in the current study for the basin integration: the Atlantic Ocean (green), the Southern Ocean (blue) and the Indo-Pacific Oceans (pink). Annual mean changes (relative to the preindustrial time) during 1861-2005 in the basin integrated full-depth oceanic heat budget for each basin that includes basin-integrated OHU (red, ⊗ denoting downward OHU anomalies, ⊙ denoting upward OHU anomalies), basin integrated OHS (black, positive denoting an OHS increase and negative denoting an OHS decrease) and interbasin ocean heat transport (blue arrow, southward negative and northward positive) for the 8-model ensemble (a) HIST-AER and (b) HIST-GHG simulations. The numbers are presented in form of multi-model mean ± one standard deviation among models, are in units of TW (1TW = 10^{12} Watt).

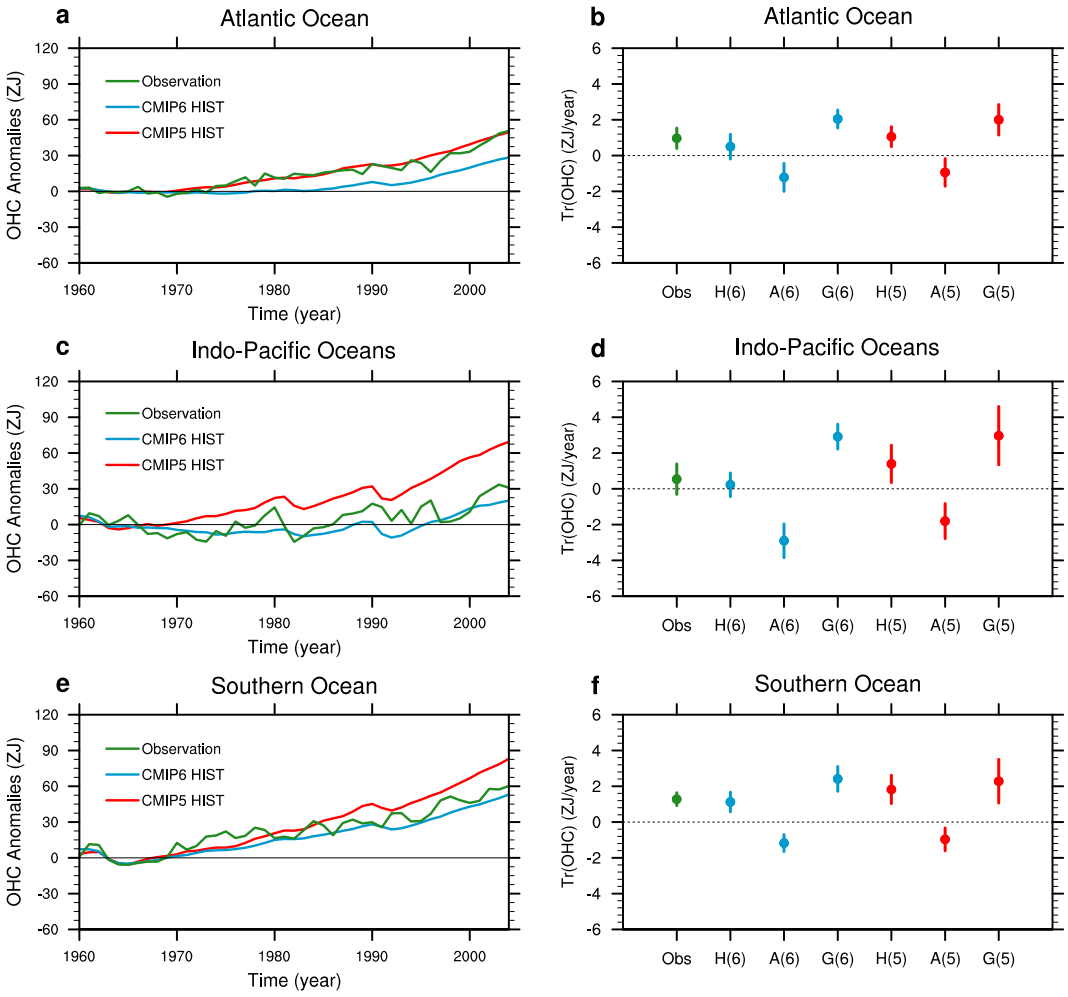

Figure 3.6: Observed and simulated OHC changes. (a,c,e) Annual mean upper 2000-m OHC anomalies (relative the 1960-1969 average) integrated over the (a) Atlantic, (c) Indo-Pacific and (e) Southern Oceans during 1960-2005 from 6 observational datasets (mean, green; uncertainty, light green; 1ZJ = 1021 Joule) and historical simulations (HIST) with 10 CMIP5 models (multi-model mean, red; inter-model spread, light red) and 10 CMIP6 models (multi-model mean, blue; inter-model spread, light blue). (b,d,f) Trends of annual mean upper 2000-m OHC integrated over the (b) Atlantic, (d) Indo-Pacific and (f) Southern Oceans during 1960-2005 for observational datasets (Obs), CMIP6 HIST [H(6)], CMIP6 HIST-AER[A(6)], CMIP6 HIST-GHG [G(6)], CMIP5 HIST [H(5)], CMIP5 HIST-AER [A(5)] and CMIP5 HIST-GHG [G(5)] simulations in form of observation/model mean (dot) ± one standard deviation among observations/models (bars). Ocean temperature drifts (500-year temperature trends in preindustrial control runs, see Methods) have been removed from CMIP5/6 model simulations before the calculation of OHC.

Chapter 4

Impacts of Arctic sea ice loss on global ocean circulations and interbasin ocean heat exchanges

Abstract

The Arctic sea ice loss during the past several decades plays an important role in driving global climate change. Herein we explore the effects of Arctic sea ice loss on global ocean circulations and ocean heat redistribution. We find that in response to Arctic sea ice loss, oceans are taking up heat from the atmosphere via sensible and latent heat fluxes mainly in the subpolar North Atlantic. Meanwhile, Arctic sea ice loss induced ocean circulation changes could redistribute the taken heat, which, however, is timescale-

dependent. Within a decade after Arctic sea ice loss, the Atlantic meridional overturning circulation (AMOC) is little altered such that most of the taken heat is locally stored in the Atlantic. On a multidecadal to centennial timescale, the AMOC decelerates redistributing the heat to other basins through interbasin ocean heat exchanges. In the Indo-Pacific Ocean, an anomalous ocean circulation is generated manifesting an abnormal northward flow near the surface, which imports about one-third of the redistributed heat from the Atlantic, via the Southern Ocean and into the Indian Ocean. Meanwhile, the Indonesia Throughflow weakens giving rise to an anomalous ocean heat transport from the Indian to Pacific Ocean. As a result, both Indian and Pacific Oceans are warmed on a multidecadal to centennial timescale. The Arctic sea ice loss also induces a "mini" global warming with a pronounced lower to middle tropospheric warming in the Southern Hemisphere. Accordingly, the Southern Hemisphere westerly winds poleward intensify to modulate the Deacon Cell and residual MOC in the Southern Ocean. Along with the ocean circulation changes and associated variations in ocean heat transport across the boundary between the Southern Ocean and Atlantic/Indo-Pacific Oceans, two-thirds of the ocean heat imported from the Atlantic remains in the Southern Ocean.

4.1 Introduction

Satellite observations depict that Arctic sea ice has declined rapidly during the past several decades [Figure 4.1a, b and c; e.g., Ding et al. (2017); Stroeve et al. (2012)], which has been attributed to greenhouse gases (GHGs) increases [e.g., Vihma (2014); Park et al. (2015)] and internal climate variability (Li et al. 2018). Arctic sea ice loss has been suggested as a key factor in driving climate changes in northern mid- and high-latitudes. For instance, over the Arctic Ocean, sea ice retreat opens ocean and hence modulates the atmosphere-ocean exchanges, leading to an increase in atmospheric moisture (Rinke et al. 2013) as well as the heat flux from oceans to the atmosphere [e.g., Francis et al (2009); Overland and Wang (2010)]. The sea ice induced atmospheric moisture increase and low tropospheric warming can extend to the Northern Hemisphere mid- and high-latitudes [Deser et al. (2010); Screen and Simmonds (2010)] where the meridional gradient of low-level atmosphere temperature weakens (Francis et al. 2009). As a result, North Pacific storm tracks migrate southward (Oudar et al. 2017), along with a dipole-like sea level pressure change that resembles the negative phase of the North Atlantic Oscillation (Peings and Magnusdottir 2014).

The effect of Arctic sea ice loss does not restrict to northern mid- and high-latitudes but extends over the globe (Liu and Fedorov 2019). Chiang and Bitz (2005) perturbed high latitudes ice cover in a slab ocean model and found

that rapid cooling and drying air is generated over the entire high- and mid-latitude and subsequently extend to Pacific and Atlantic low latitudes. Later, Deser et al. (2015) analyzed the effect of Arctic sea ice loss in both slab-ocean and coupled atmosphere-ocean model simulations and found that the ice effect is mainly confined in the northern hemisphere with warming in the high latitudes in the absence of ocean dynamics. However, when ocean dynamics are considered, the effect of Arctic sea ice loss can extend to tropics or even Antarctic, prompting a global warming except the low stratosphere in high latitudes in both hemispheres. The difference between slab-ocean and coupled atmosphere-ocean model simulations indicates the importance of ocean circulation to global climatic impacts of Arctic sea ice loss. Particularly, as a density-driven ocean circulation that is related to deep water formation in the subpolar North Atlantic, the Atlantic meridional overturning circulation (AMOC), has drawn the most attention (Liu et al. 2017). It has been reported that Arctic sea ice loss can modulate AMOC variations through either haline [Jungclaus et al. (2005); Sévellec and Fedorov (2015)] or thermal (Levermann et al. 2007) processes. Conducting an adjoint sensitivity analysis with an ocean model, Sévellec et al. (2017) suggested that both thermal and haline processes operate in contributing to the generation of buoyancy anomalies and a subsequent AMOC weakening. This result was supported by later studies

based on fully coupled climate model simulations [Sun et al. (2018); Liu et al. (2019); Li H. et al. (2021); Liu and Fedorov (2021)].

The AMOC slowdown, on the other hand, can modulate the ocean heat uptake, transport and storage in the Atlantic. Previous GHGs warming [e.g., Shi et al. (2018); Liu et al. (2020)] and freshwater hosing [e.g., Zhang and Delworth (2005); Jackson and Wood (2020)] experiments showed that a weakened AMOC causes a reduced northward ocean heat transport in the Atlantic, which results in an oceanic heat divergence and temperature cooling to the south of Greenland. The surface temperature cooling, furthermore, promotes ocean heat uptake in the subpolar North Atlantic region [e.g., Drijfhout (2015); Gregory et al. (2016); Ma et al. (2020); Marshall and Zanna (2014); Shi et al. (2018); Winton et al. (2013)].

Meanwhile, as a part of global conveyor belt, the AMOC can also play a role in modifying the ocean heat content in ocean basins beyond the Atlantic (Garuba and Klinger 2016). Triggered by a perturbation in the North Atlantic Deep Water formation to decelerate the AMOC, the subsequent signals propagate in form of an equatorward Kelvin wave along the western boundary in the Atlantic [Kawase (1987); Johnson and Marshall (2002); Zhang (2010)]. They further travel across the equator eastwardly and propagate poleward along the eastern boundary [e.g., Cessi et al. (2004); Huang et al. (2000); Sévellec and Fedorov (2013); Sun et al. (2020)]. The Kelvin wave leads to

abnormal meridional geostrophic transport with opposite signs in the Indo-Pacific and Atlantic Oceans by altering the zonal difference of interface depth, hence resulting in an abnormal northward ocean circulation near the surface at the boundaries with the Southern Ocean (Sun et al. 2020). Also, the Indonesian Throughflow (ITF) weakens due to a decreased pressure gradient between the Indian Ocean and Pacific (Sun and Thompson 2020), which further adjusts the interbasin exchange between the Pacific and Indian Oceans [e.g., Hu and Sprintall (2017); Lee et al. (2015)].

To summarize, Arctic sea ice loss has been suggested to induce an AMOC slowdown that can reshape the ocean heat content in ocean basins under GHGs warming and freshwater hosing scenarios. Nevertheless, it remains unclear that how Arctic sea ice loss, via changing the AMOC, governs global ocean heat uptake and heat redistribution between ocean basins. This is because, under GHGs warming, changes in Arctic sea ice and the AMOC happen concurrently such that it is hard to disentangle their effects on global ocean heat uptake and redistribution. Moreover, global ocean heat content anomalies could be attributed more to direct surface warming such that the effect of ocean circulation change is overwhelmed (Garuba and Klinger 2016). The freshwater hosing, on the other hand, is usually discussed in the context of paleo-climate (e.g., Yang et al. 2015a) in which large freshwater discharges due to past icesheet melts cause a strong AMOC weakening (McManus et al.

2004). The impact of on-going and future icesheet melts that mainly come from Greenland in the Northern Hemisphere, however, is of secondary importance to the on-going and future AMOC changes (Bakker et al. 2016).

In this study, we will combine observations and climate model simulations to explore the impacts of Arctic sea ice loss on global ocean circulations, heat uptake and redistribution.

4.2 Methods

4.2.1 Observations

We use observations of Arctic sea ice concentration and extent from the National Snow and Ice Data Center (NSIDC). The observations are produced based on two brightness temperature data sets: one is derived from Nimbus-7 Scanning Multichannel Microwave Radiometer (SMMR) processed at NASA Goddard Space Flight Center (GSFC), and the other is derived from Special Sensor Microwave/Imagers (SSM/Is) and Special Sensor Microwave Imager/Sounder (SSMIS) processed at the NSIDC. The NSIDC data include monthly averaged sea ice concentration and extent since 1978 October, wherein the sea ice concentration is provided in the polar stereographic projection at a grid cell of 25 km × 25 km. The sea ice extent is defined as the ocean area with sea ice concentration at least 15%. In this study, we compare the annual mean sea ice concentrations over the Arctic area during two periods

of 1980-1989 and 2006-2015 and adopt the difference between these two periods (Figure. 4.1a, b and c) as the benchmark for the following experimental setup. Particularly, the observed annual sea ice extent indicates a decrease by about 14% from 1980-1989 to 2006-2015, with the maximum seasonal decrease occurring in September by about 33% (Figure C1).

4.2.2 Model experiment

We use the Community Earth System Model (CESM) version 1.0.4 from the National Center for Atmospheric Research that includes the Community Atmosphere Model version 4 [CAM4; Neale et al. (2010)], the Community Land Model, version 4 [CLM4; Lawrence et al. (2012)], the Parallel Ocean Program, version 2 [POP2; Smith et al. (2010)], and the Community Ice Code, version 4 [CICE4; Holland et al. (2012)]. The atmosphere and land components use a T31 spectral truncation with 27 vertical layers in the atmosphere. The ocean and sea ice components use an irregular horizontal grid with a nominal ~3° resolution but is significantly finer (~1°) close to Greenland and in the Arctic Ocean. There are 60 vertical layers in the ocean. The ocean model employs a variable coefficient in the Gent-McWilliams eddy parameterization (Gent and McWilliams 1990), which allows the model to simulate an appropriate ocean response to wind change as indicated by eddy-resolving models (Gent and Danabasoglu 2011)

We conduct ensemble perturbation experiments based on the CESM preindustrial control run to replicate the observed Arctic sea ice loss during the past several decades. To achieve this goal, we lower the albedo of bare and ponded sea ice and snow cover on ice over the Arctic Ocean in the model sea ice component. We have tested different sea ice/snow reflectivity and emissivity parameters to achieve an Arctic sea ice loss. Herein we adopt one of the simulations that depicts the observed Arctic sea ice best (Figure 4.1d, e and f) in which the standard deviation parameters of bare and ponded sea ice (R_{ice} and R_{pnd}) are changed from 0 to −2 and the single scattering albedo of snow is reduced by 9% for all spectral bands. Further, to diminish the effect of internal variability, we also slightly modify the initial condition of the model atmosphere component to obtain 10 ensemble members. All of ensemble members are performed with the "best" sea ice/snow reflectivity and emissivity parameters and last for 200 years. We mainly present the results from the ensemble mean in the following parts. For example, the ensemble mean shows that the annual Arctic sea ice area has been decreased by about 14% in the last 100 years of the simulation compared with the control run, which is close to the observed Arctic sea ice loss from 1980-1989 to 2006-2015. The seasonal Arctic sea ice reduction also peaks in September, by about 34% relative to the control run (Figure C1).

4.2.3 Ocean heat budget analysis

We use the basin-integrated full-depth oceanic heat budget as below:

$$\iiint \rho_0 C_P \frac{\partial \theta}{\partial t} dxdydz + \iiint \rho_0 C_P [\nabla \cdot (\mathbf{v}\theta + D)] dxdydz = \iint (NSHF) dxdy \quad (4.1)$$

where ρ_0 is seawater density, Cp is the specific heat of sea water and θ is potential temperature of sea water. NSHF denotes net surface heat flux, which is the sum of radiative shortwave (SW) and longwave (LW) fluxes, turbulent sensible (SH) and latent (LH) heat fluxes as well as the heat flux due to snow/sea ice formation and melt (IMS). ∇ and **v** are three-dimensional gradient operator and velocity, and $\mathbf{v} = \bar{\mathbf{v}} + \mathbf{v}^*$. D denotes diffusion and other sub-grid processes. The x and y integrals are from the western to eastern boundary and from the southern to northern boundary for individual basins (the x integral is contour integral at the latitude of the Drake Passage). The z integral is from ocean bottom to ocean surface.

Based on Eq. (4.1), the ocean heat content (OHC) is defined as:

$$OHC = \iiint \rho_0 C_P \theta dxdydz \quad (4.2)$$

The OHC tendency as ocean heat storage (OHS) is defined as:

$$OHS = \frac{\partial}{\partial t} OHC = \frac{\partial}{\partial t} \iiint \rho_0 C_P \theta dxdydz \quad (4.3)$$

The ocean heat uptake (OHU) is defined as:

$$OHU = \iint (NSHF) dxdy \quad (4.4)$$

The interbasin oceanic heat transport (*OHT*) is defined as:

$$OHT = \iint \rho_0 C_P (\bar{\mathbf{v}}\theta + \mathbf{v}^*\theta + D) dxdz = \overline{OHT} + OHT^* + OHT^d \quad (4.5)$$

where $\overline{OHT} = \iint \rho_0 C_P \bar{\mathbf{v}} \theta dxdz$, $OHT^* = \iint \rho_0 C_P \mathbf{v}^* \theta dxdz$ and $OHT^d = \iint \rho_0 C_P D dxdz$. Eq. (4.5) shows that the interbasin ocean heat transport (OHT) at each ocean boundary, can be induced by Eulerian-mean flow ($\overline{\text{OHT}}$), eddies (OHT*) and diffusion (OHT^{d}) (Yang et al. 2015b).

For each basin, the net meridional oceanic heat transport is calculated as the sum of the OHT across the boundaries of the basin. As a result, the basin-integrated oceanic heat budget by Eq. (4.1) can be written as:

$$OHS = OHU - (OHT_{north} - OHT_{south}) \tag{4.6}$$

where $\text{OHT}_{\text{north}}$ and $\text{OHT}_{\text{south}}$ denote the OHTs at the northern and southern boundaries of each ocean basin. Note here, OHT in Eq. (4.5) is defined as meridional ocean heat transport since it will be mostly discussed in the following sections, whereas the OHT between the Indian and Pacific Oceans is zonal, which should be otherwise defined as $OHT = \iint \rho_0 C_P (\bar{\mathbf{v}} \theta + \mathbf{v}^* \theta + D) dydz$. Accordingly, the OHT at the eastern boundary of the Indian Ocean (or at the western boundary of the Pacific Ocean) should be considered. For simplicity, we keep the expressions of Eq. (4.5) and Eq. (4.8) and add the note here.

In this study, Arctic sea ice loss induced changes in the ocean heat budget in the perturbation experiment are defined as:

$$\Delta OHS = \Delta OHU - (\Delta OHT_{north} - \Delta OHT_{south}) \tag{4.7}$$

ΔOHS can be represented by the change in the OHC tendency [ΔTr(OHC)], which is defined as

$$\Delta Tr(OHC) = Tr(OHC) - Tr(OHC_{ctrl}) \quad (4.8)$$

where Δ refers to the differences between the perturbation experiment and the control run simulation and Tr(OHC) and $\mathrm{Tr(OHC_{ctrl})}$ refer to the OHC trends in the Arctic sea ice perturbation simulation and the preindustrial control run. $\mathrm{Tr(OHC_{ctrl})}$ could be associated with the temperature trend drift in the control, which might be small but is not necessary to be zero. Eq. (4.7) indicates that the ocean heat storage anomaly induced by Arctic sea ice loss within one ocean basin is determined by the ocean heat uptake via atmosphere-ocean interface and the net ocean heat transports by ocean circulations, eddies and diffusion across the boundaries of the basin.

We further decompose the Eulerian mean OHT change ($\Delta\overline{\mathrm{OHT}}$) into the circulation anomaly driven component ($\overline{\mathrm{OHT}}_{v'}$) and the temperature anomaly driven component ($\overline{\mathrm{OHT}}_{\theta'}$). Specifically,

$$\overline{OHT}_{v'} = \iint \rho_0 C_P \bar{\mathbf{v}}' \theta_0 dxdz \quad (4.9)$$

where $\bar{\mathbf{v}}'$ denotes the change in monthly Eulerian-mean velocity and θ_0 is the monthly climatological ocean temperature in the control run.

$$\overline{OHT}_{\theta'} = \iint \rho_0 C_P \bar{\mathbf{v}}_0 \theta' dxdz \quad (4.10)$$

where θ' denotes the change in monthly ocean temperature and $\bar{\mathbf{v}}_0$ is the monthly climatological Eulerian-mean velocity in the control run.

4.3 The fast response due to regional atmosphere-ocean interactions

We first examine the changes in Arctic sea ice and ocean circulations in our Arctic sea ice perturbation experiment. In response to the reduced albedo, Arctic sea ice shows a rapid decrease of up to 2×10^{12} m^2 in area and is up to 2 m in thickness within the first 5 years of the experiment (Figure 4.2a; Figure C3). The rapid Arctic sea ice retreat produces a surface freshwater input to the northern hemisphere oceans up to about 0.2 Sv (e.g., Li and Fedorov 2021), which is within the range of previous housing experiments (e.g., Jackson and Woods, 2020). Compared to this fast sea ice retreat, changes in ocean circulations are much slower and related to the propagation of sea ice induced buoyancy signals (Liu et al. 2019). During the first 10 years, most of sea ice induced buoyancy signals are confined within central Arctic Ocean and the Barents Sea. After that, these buoyancy anomalies propagate downstream extending to the North Atlantic deep convection regions, which suppress the formation of North Atlantic Deep Water there [Sévellec et al. (2017); Liu et al. (2019)] and lead to an AMOC weakening on multi-decadal timescales. By the end of the perturbation experiment, the decline of the AMOC is about 6 Sv (1Sv = 10^6 m^3/s), manifesting a drop about one-third of the AMOC strength in preindustrial control run (Figure 4.2b).

Along with the fast sea ice but slow AMOC responses, ocean heat uptake and interbasin ocean heat exchange exhibit distinct evolution patterns on different timescales. Within the first 10 years of the experiment when the AMOC strength is rarely modified by Arctic sea ice loss, changes in oceanic heat are mainly driven by atmospheric processes and constrained in the Atlantic basin. Specifically, Arctic sea ice loss allows more incoming solar radiation to warm the lower to middle troposphere in the Northern Hemisphere (Figure C4a). The atmospheric warming pattern here is consistent with previous studies with atmosphere-only simulations (e.g., Deser et al. 2015), thus identifying the dominant role of atmospheric processes in the fast response to Arctic sea ice loss.

Besides the warming in the atmosphere, Arctic sea ice loss can affect ocean surface heat fluxes. In the North Atlantic, we find that the Arctic sea ice loss promotes a net surface heat flux (NSHF) in the first 10 years of the perturbation experiment (Figure 4.3a). The intensified NSHF is mainly attributed to the increase of surface turbulent heat fluxes (sensible plus latent heat fluxes) as a result of atmospheric warming [Figure C5a; also c.f. Screen et al. (2013); Oudar et al. (2017)]. Meanwhile, the altered ice melting and formation create a positive anomaly of surface heat flux to the south of Greenland (Figure C5c) through a net latent heat release after the phase changes over seasons. The sea ice loss also leads to an open ocean, allowing

more solar radiation absorbed by the ocean. Though solar warming is partially compensated by longwave cooling at ocean surface, the net surface radiative (shortwave plus longwave) energy flux anomaly is positive over the Labrador Sea (Figure C5b), indicating that heat is entering the ocean in the North Atlantic in response to Arctic sea ice loss.

On the other hand, the AMOC is little modified within the first 10 years. With a neglectable AMOC change, the meridional ocean heat transports across the boundary between the Atlantic and Southern Oceans (~32°S) and the boundary between the Atlantic and Arctic Oceans (~65°N) are also little altered (Figure 4.4a). As a result, changes in the net OHT are much smaller than those in the OHU over the Atlantic basin, which suggests a dominant role of atmosphere-ocean interactions in modifying the Atlantic Ocean heat storage on a decadal time scale in response to Arctic sea ice loss.

The neglectable changes in OHT across the Atlantic boundaries indicate that the Atlantic neither exports heat into nor imports heat from other ocean basins. Hence most of the taken heat from the atmosphere is stored locally contributing to the OHS increase in the Atlantic. Herein we quantify the change rate of the integrated OHC over the whole Atlantic basin and find that the Atlantic Ocean has gained about 0.07 PW from the atmosphere during the first 10 years of the experiment (Figure 4.4a). In another word, with neglectable interbasin ocean heat exchanges, OHU dominates the OHS within

the Atlantic basin at a rate of 0.07 PW (Figure 4.4a). The spatial pattern of OHC trend generally follows that of NSHF change while the latter features an increase spreading most of the Atlantic and peaking at a rate of 10 W/m^2 in the subpolar region (Figure 4.3b). Correspondingly, the zonal mean ocean temperature exhibits a broad warming trend in the Atlantic (Figure 4.5a). To the south of 20°N, the ocean warming occurs in the upper 800m up to 0.1 K/decade. In mid-latitudes between 40°N and 60°N, the ocean warming can even penetrate to about 3000m in form of an equatorward tongue. Given a slight AMOC change during this period, the deep-reaching warming anomaly can be mainly attributed to surface heating and resultant warming signals carried by background ocean circulations (Winston et al. 2013).

Outside the Atlantic, Arctic sea ice loss also causes changes in surface heat flux over other ocean basins during the first 10 years. For instance, we find that Arctic sea ice loss can induce warming at the North Pacific surface via enlarged turbulent heat fluxes (Figure 4.3a and C5a), which could be associated with the advection of anomalous warm air from the Arctic to the surrounding regions (Sun et al. 2018). Meanwhile, the signal of stronger natural variability such as the Pacific Decadal Oscillation or Interdecadal Pacific Oscillation may still be detectable in the Pacific even in the 10-member ensemble mean. However, unlike the Atlantic, the increase in turbulent heat fluxes over the North Pacific is largely compensated by the decreases in

radiative energy fluxes there (Figure C5b). Besides, Arctic sea ice loss brings on a turbulent heat cooling in the southern and western Pacific that acts to dampen the warming in high latitudes, resulting in few net surface heat flux changes over the Pacific (Figure C6c). Similarly, in the Southern Hemisphere mid- and high-latitudes, Arctic sea ice loss promotes a turbulent heat warming over the Amundsen Sea and Ross Sea but a cooling over the eastern Atlantic and Indian Ocean sectors (Figure C5a). Thus the change in NSHF over the Southern Ocean is negligible when it is integrated over the whole basin (Figure C6d). Our result shows that, despite surface warming and cooling over a global scale due to rapid atmosphere processes, the basin integrated OHU increase is mainly confined in the Atlantic within the first 10 years after Arctic sea ice loss (Figure C6a).

4.4 The slow response dominated by interbasin ocean heat exchanges

4.4.1 Ocean heat uptake and redistribution within the Atlantic

Arctic sea ice loss can affect global ocean heat content via oceanic processes on a multidecadal to centennial timescale by altering ocean circulations and interbasin ocean heat exchanges. In the Atlantic, the AMOC has weakened by about 6 Sv about 100 years after the sea ice perturbation.

This AMOC weakening modifies the interbasin ocean heat exchanges between the Atlantic and other oceans.

Here we decompose the $\overline{\mathrm{OHT}}$ change into the circulation anomaly driven component ($\overline{\mathrm{OHT}_{v'}}$) and the temperature anomaly driven component ($\overline{\mathrm{OHT}_{\theta'}}$). We find that the weakened AMOC diminishes the northward $\overline{\mathrm{OHT}_{v'}}$ by about 0.12 PW across the boundary between the Atlantic and Southern Oceans (Figure 4.6b). The $\overline{\mathrm{OHT}_{v'}}$ reduction is slightly compensated by an $\overline{\mathrm{OHT}_{\theta'}}$ increase (Figure 4.6b) due to the enlarged vertical ocean temperature contrast such that the interbasin exchange $\overline{\mathrm{OHT}}$ induced by Eulerian-mean flows abates by about 0.12 PW (Figure 4.6b). On the other hand, ocean eddies and diffusion processes have a minor contribution to the change in the meridional ocean heat transport here. As a result, the net northward OHT reduces by about 0.13 PW (Figure 4.6a), indicating that the Atlantic is exporting heat across the boundary between the Atlantic and Southern Oceans. Meanwhile, the northward OHT also decreases across the boundary between the Atlantic and Arctic Oceans but by much smaller amplitude, around 0.01 PW (Figure 4.4a).

Besides the OHT changes across the Atlantic boundaries, we examine the OHU changes within the Atlantic 100 years after the sea ice perturbation. The weakened AMOC brings down the northward ocean heat transport and hence leads to an anomalous ocean heat divergence in the subpolar North Atlantic, which in turn can modify surface heat fluxes as well as OHU [Liu and

Fedorov (2019); Liu et al. (2020)]. In response to Arctic sea ice loss, the AMOC slowdown produces a robust SST cooling in the North Atlantic over the "warming hole" region up to -0.6 K [Figure 4.7b; also c.f. Deser et al. (2015); Simon et al. (2021); Sun et al. (2018)], which enhances the atmosphere-ocean surface temperature contrast (Figure C7b). The enlarged temperature contrast can alter the turbulent feedback via the thermal adjustment of atmosphere boundary layer to the SST anomaly and modifying the upper limit of the feedback [Hausmann et al. (2016); Zhang and Cooke (2021)]. This process promotes a further increase of turbulent heat fluxes and *OHU* (Figure C5g and 4.3e), allowing more atmospheric heat to enter the North Atlantic [e.g., Drijfhout (2015); Ma et al. (2020); Marshall and Zanna (2014); Shi et al. (2018); Winton et al. (2013)].

Combining both changes in OHU and OHT, we find that atmospheric heat entering the subpolar North Atlantic is mostly exported into the Southern Ocean along with a slowdown of the AMOC. We compare the OHU and OHS between the first 10 years and the last 100 years of our experiment and find that the weakened AMOC leads to an amplified OHU in the North Atlantic up to 10 W/m^2 (Figure 4.3e). On the contrary, the OHS decreases to the north of 20°N in the North Atlantic (Figure 4.3f). Consistent with this OHS decrease, the horizontal and vertical extents of Atlantic warming reduce. Ocean warming is mainly confined between 38°N and 45°N in the upper 1500m

during the last 100 years, with magnitude cut by about half (Figure 4.5b). To the north of 45°N, the ocean warming occurred in the first 10 years is replaced by an ocean cooling extending from the surface down to the bottom (Figure 4.5b). Similar ocean temperature changes have also been found in previous cases of AMOC slowdown [e.g., He et al. (2020); Liu et al. (2020)], indicative of a dominant role of ocean circulation changes in controlling subsurface temperature changes in the mid-latitude and subpolar North Atlantic.

To the south of 20°N, warming signals emerge in the upper 1400m accompanying with the AMOC slowdown (Figure 4.5b). Seen from on the lower limb of the Atlantic overturning at the 1000-m level (see Figure 4.8c contours), warming signals propagate southward in the Atlantic following the deep western boundary and equatorial Kelvin waves (Figure 4.9b). This pattern is consistent with paleoclimate observations (Weldeab et al. 2016), revealing the path of temperature anomaly propagation and the mechanisms on ocean heat redistribution and storage in the Atlantic basin [Kostov et al. (2014); Pedro et al. (2018); Zhang et al. (2018)].

4.4.2 Heat import and redistribution in the Indian and Pacific Oceans

From previous studies [Garuba and Klinger (2016); Sun et al. (2020)], the temperature signals associated with a weakened AMOC travel along the

South Atlantic eastern boundary [e.g., Huang et al. (2000); Kawase (1987); Sévellec and Fedorov (2013)], which can further spread into the Indian Ocean in form of a geostrophic transport response. In the Indian Ocean, these signals act to deepen the isopycnals along the western Indian Ocean and result in anomalous ocean circulation. In our experiment, we find that the anomalous ocean circulation in the Indo-Pacific is up to 2.4 Sv at its maximum, characterized by a northward transport near the surface and a southward transport in the deep ocean (Figure 4.8d). The anomalous ocean circulation generates an anomalous heat transport from the Southern Ocean to the Indian Ocean. Though the circulation driven heat transport anomaly is partially compensated by a concurrent temperature driven heat transport anomaly (Figure 4.6d), the Indian Ocean receives a heat import of 0.05 PW from the Southern Ocean (Figure 4.6c). This means that, about two-thirds of the redistributed heat from the Atlantic remain in the Southern Ocean, while the left one-third is imported by the Indo-Pacific after 100 years of sea ice perturbation.

The imported heat from the Atlantic is further redistributed between the Indian and Pacific Oceans by the ITF. As part of the global convey belt, the ITF also weakens, which is dynamically linked to the AMOC slowdown (Sun and Thompson 2020). The ITF weakening begins about 30 years after the

Arctic sea ice perturbation, lasting for another 80 years and ends up with a reduction of about 1.5 Sv (Figure 4.2c).

Associated with the weakened ITF, the climatological heat transport from the Pacific to the Indian Ocean is reduced by about 0.03 PW (Figure 4.6g), accounting for about 60% of the imported heat into the Indian Ocean across the boundary between the Indian and Southern Oceans. This means that the Indian Ocean imports heat from the Southern Ocean and exports part of the heat to the Pacific. As a result, about 40% of the imported heat remains in the Indian Ocean, a part of which is then released back to the atmosphere in the form of negative OHU through turbulent and radiative heat fluxes (Figure 4.4b). Consequently, the Indian Ocean gains heat at about 0.01 PW in response to Arctic sea ice loss as reflected by a warming trend (>0.02 K/decade) in the upper 1000-m ocean (Figure 4.5d). The anomalous heat transport associated with the weakened ITF contributes to the ocean warming in the Pacific. With small amounts of the interbasin exchanges at the boundary between the Pacific and Southern Oceans and the boundary between the Pacific and Arctic Oceans (Figure 4.4c), the ITF plays a dominant role in the interbasin ocean heat transport for the Pacific basin. The changes in the ITF and associated OHT lead to an OHS increase of about 0.02 PW (Figure 4.4c) that is reflected by a warming trend in the upper 1800 m to the south of 40°N in the Pacific Ocean (Figure 4.5f).

4.4.3 Linkage to the Southern Ocean

In our experiment, we find that Arctic sea ice loss induces a dipole-like pattern of surface zonal wind stress change, with positive (negative) anomalies to the south (north) of 42°S. The positive surface zonal wind stress anomalies peak around 55°S up to about 0.004 N/m^2 (Figure 4.10b). Consequently, the Deacon Cell is poleward displaced and strengthened by about 0.6 Sv at its maximum (Figure 4.10b), which is partially amplified (offset) by the eddy-driven MOC to the north (south) of 45°S due to altered isopycnal tilting and baroclinicity (Figure 4.10d). Therefore, changes in the residual MOC generally follow those in the Deacon Cell showing a poleward shift in the later 100 years in the perturbation experiment (Figure 4.10f).

Changes in the Southern Ocean MOCs are responsible for the altered OHT across the boundaries between the Southern Ocean and other basins (the Atlantic and the Indo-Pacific). Different from the first 10 years when the wind driven ocean circulation anomalies are mainly confined to the south of 40°S (Figure 4.10a), negative surface wind stress anomaly engenders a southward flow near the surface at these boundaries in the later 100 years (Figure 4.10b), therefore leading to a net OHT import at about 0.08 PW into the Southern Ocean. Specifically, the Southern Ocean imports about 0.13 PW from the Atlantic but exports about 0.05 PW to the Indian Ocean (Figure 4.4d). Meanwhile, the Southern Ocean releases heat of about 0.03 PW via ocean

surface back to the atmosphere primarily via diminished turbulent heat fluxes (Figure C6d). As a result, the basin-integrated OHS is increased by about 0.05 PW (Figure 5.4d), which indicates a subsurface warming and an OHC increase within the Southern Ocean.

We further find that Arctic sea ice loss induced Southern Ocean warming mainly occurs to the north of 50°S manifesting a downward and equatorward warming tongue (>0.02 K/decade) to the north of 47°S (Figure 4.5h). Our result well agrees with Pedro et al. (2018) and suggests that the Southern Ocean plays an important role in global ocean heat redistribution. The region to the north of the Antarctic Circumpolar Current serves as a heat reservoir, whilst the region to the south is seldom involved. Two processes operate during the interbasin heat redistribution. On one hand, triggered by the Arctic sea ice loss, the poleward intensified Southern Hemisphere westerly winds enhance the Ekman downwelling in the mid-latitude ocean, deepen the isopycnals and bring on a subsurface warming [e.g., Li et al. (2021); Liu et al. (2018); Lyu et al. (2020)]. On the other hand, Arctic sea ice loss results in a "mini" global warming along with a significant surface warming in the mid- and high-latitude Southern Ocean (Figure 4.7b). The subduction of the surface warming signals can also contribute to the warming in the interior ocean (e.g., Lyu et al. 2020). Both processes highlight the important role of the

atmosphere-ocean coupling and teleconnection in understanding the global effects of Arctic sea ice loss.

4.5 Conclusion and discussion

In this study, we analyze the effects of Arctic sea ice loss on global ocean circulation changes and global heat redistribution by conducting ensemble sea ice perturbation simulations with a fully coupled climate model. We find that Arctic sea ice loss promotes ocean heat uptake in the North Atlantic "warming hole" region via an increase of turbulent heat fluxes. During the first 10 years since sea ice perturbation, the AMOC is little altered such as most of the taken heat is stored locally in the Atlantic. However, after the first decade, the AMOC starts to weaken, which effectively redistributes most of the taken heat from the atmosphere to other ocean basins. Meanwhile, In the Indo-Pacific Ocean, an anomalous ocean circulation is generated appearing as abnormal northward flow near the surface. This anomalous ocean circulation carries about one-third of the redistributed heat from the Atlantic to the Indian Ocean. The ITF that connects the Indian and Pacific Oceans also weakened in response to Arctic sea ice loss, which reduces the climatological ocean heat transport from the Pacific to Indian Ocean and consequently acts to warm the Pacific but cool the Indian Ocean. As a result, either the Indian or Pacific Ocean has a net import of oceanic heat from other basins as well an increase

of basin-integrated OHS. In the Southern Ocean, Arctic sea ice loss induces a strong warming in the low troposphere peaking around 50°S, which further weakens the equatorward flank of the westerly winds. This wind change modifies the MOCs in the Southern Ocean and causes an anomalous southward flow at the boundary between the Southern Ocean and Atlantic/Indo-Pacific Oceans. As a result, about two-thirds of the redistributed heat from the Atlantic remain in the Southern Ocean and lead to an interior ocean warming.

Our results have great implications on global ocean heat redistributions in future and past climate changes considering that an AMOC slowdown can occur in either scenario. For example, the Southern Ocean warming under future anthropogenic forcing has been mostly viewed as a result of the subduction of surface warming along constant density surfaces [Church et al. (1991); Garuba and Klinger (2016); Gregory et al. (2016)] or temperature anomalies carried by climatological MOCs in the Southern Ocean (Marshall et al. 2015). Nevertheless, as suggested by the results in the current study, the MOC change and circulation-driven cross-boundary OHT change can contribute to the Southern Ocean warming [Liu et al. (2018); Shi et al. (2020)], which, meanwhile, are inherently linked to the AMOC and its associated OHT changes [Pedro et al. (2018); Sun and Thompson (2020); Sun et al. (2020)].

It is worth noting that the Arctic Ocean is also warming in our perturbation experiment, which is consistent with observations [e.g., Grotefendt et al. (1998); Burgard and Notz (2017); Steele et al. (2008)], suggesting that sea ice loss also plays a role in modifying the Arctic heat budget. On one hand, Arctic sea ice loss opens the atmosphere-ocean interface and thus facilities more solar energy flux into the ocean (Liu et al. 2019). Sea ice melting itself meanwhile can also directly alter the heat flux over the surface of the Arctic Ocean. On the other hand, the ocean heat transports across the boundaries between the Arctic and North Atlantic/Pacific Oceans will be modified as a result of the global impacts of Arctic sea ice loss on ocean circulations and interbasin heat exchanges [Figure 4.4a and c, also c.f. Liu and Fedorov (2021); Li H. et al. (2021)]. Both changes in surface heat flux and inter-basin ocean heat transport act to modulate the ocean heat budget in the Arctic Ocean.

It also merits attention that a recent AMOC reconstruction at 26°N based on satellite altimetry and cable measurements suggests an AMOC decline during 1993-2014, and the decline is especially robust since mid-2000s (Frajka-Williams 2015). The observed Arctic sea ice loss since the satellite era could have been playing a role, whereas many other factors such as greenhouse gases (e.g., Gregory et al. 2005) and aerosol (e.g., Hassan et al. 2021) changes

and even natural climate variability (Robert et al. 2014) could contribute to this observed AMOC change as well.

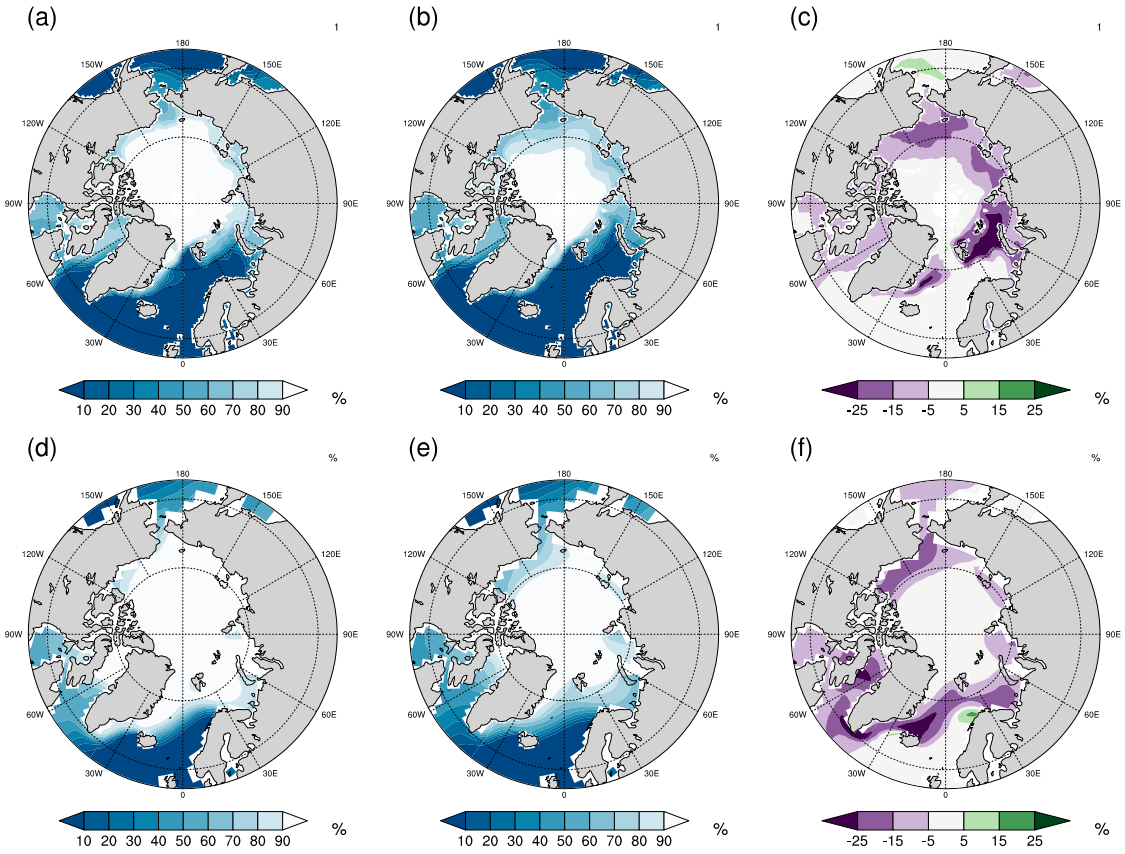

Figure 4.1: Observed annual mean of Arctic sea ice concentration from NSIDC during (a) 1980-1989 and (b) 2006-2015 and (c) the difference between the two periods given by (b) – (a). Simulated Arctic sea ice concentrations in (d) the control run, (e) the ensemble mean of the last 100 years of the Arctic sea ice perturbation simulation and (f) the difference between the two given by (e) – (d).

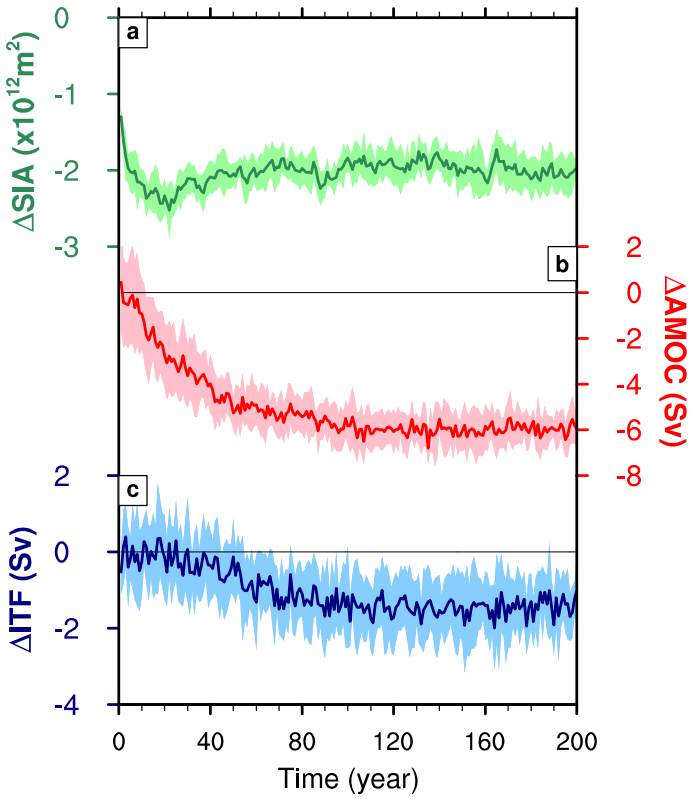

Figure 4.2: Changes in (a) Arctic sea ice area (ensemble mean, dark green; ensemble spread, light green), (b) AMOC strength (ensemble mean red; ensemble spread, pink) and (c) ITF strength (ensemble mean, dark blue; ensemble spread, blue) in the Arctic sea ice perturbation simulation. The ensemble spread is calculated as one standard deviation of the 10 ensemble members of the perturbation simulation.

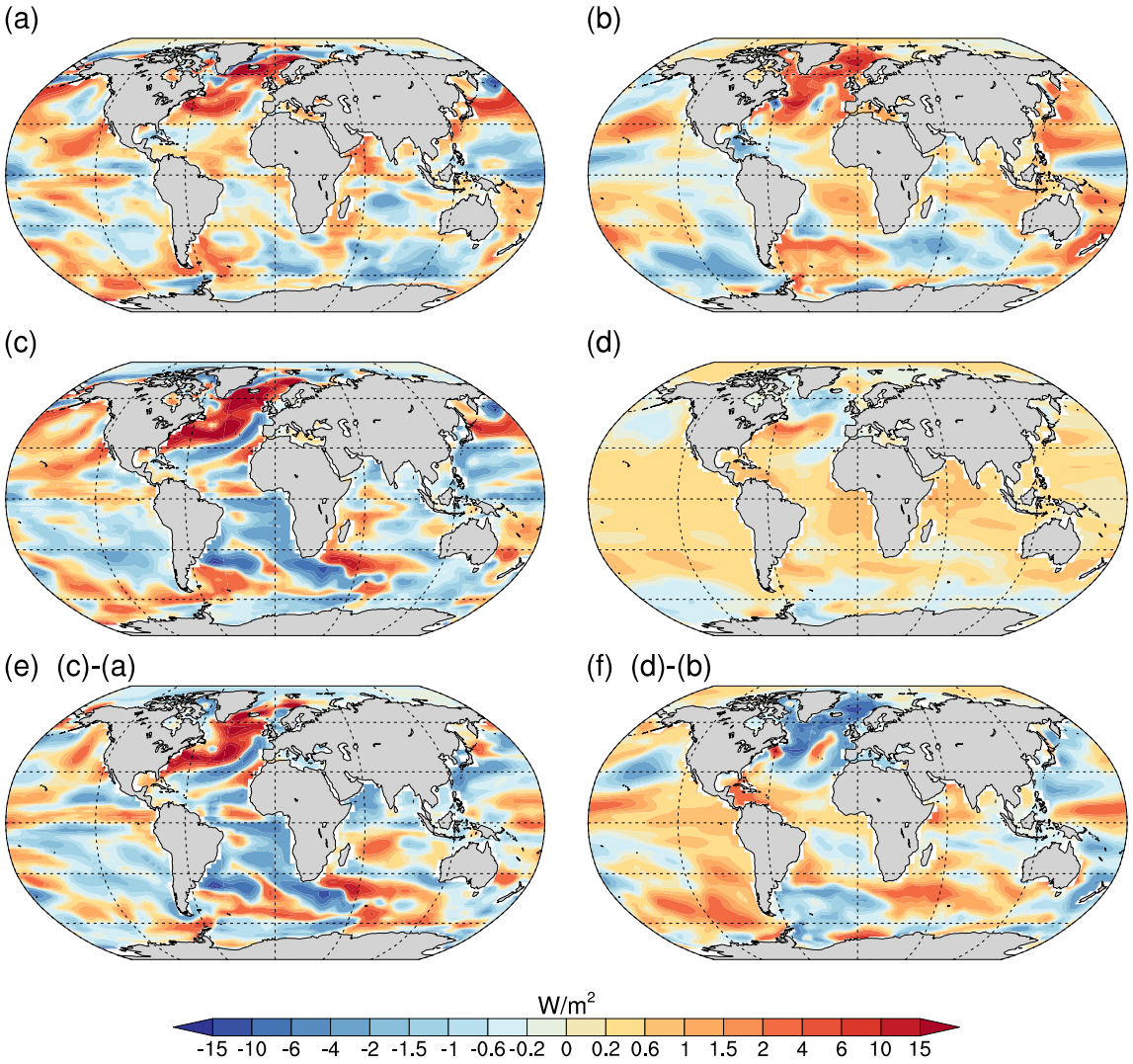

Figure 4.3: (left column) Arctic sea ice loss induced changes (relative to the control) in annual mean NSHF over (a) the first 10 years and (c) the later 100 years for the ensemble mean of the Arctic sea ice perturbation simulation as well as (e) the difference between the two given by (c)-(a). (right column) As in the left column but changes in the full depth integrated ocean heat storage.

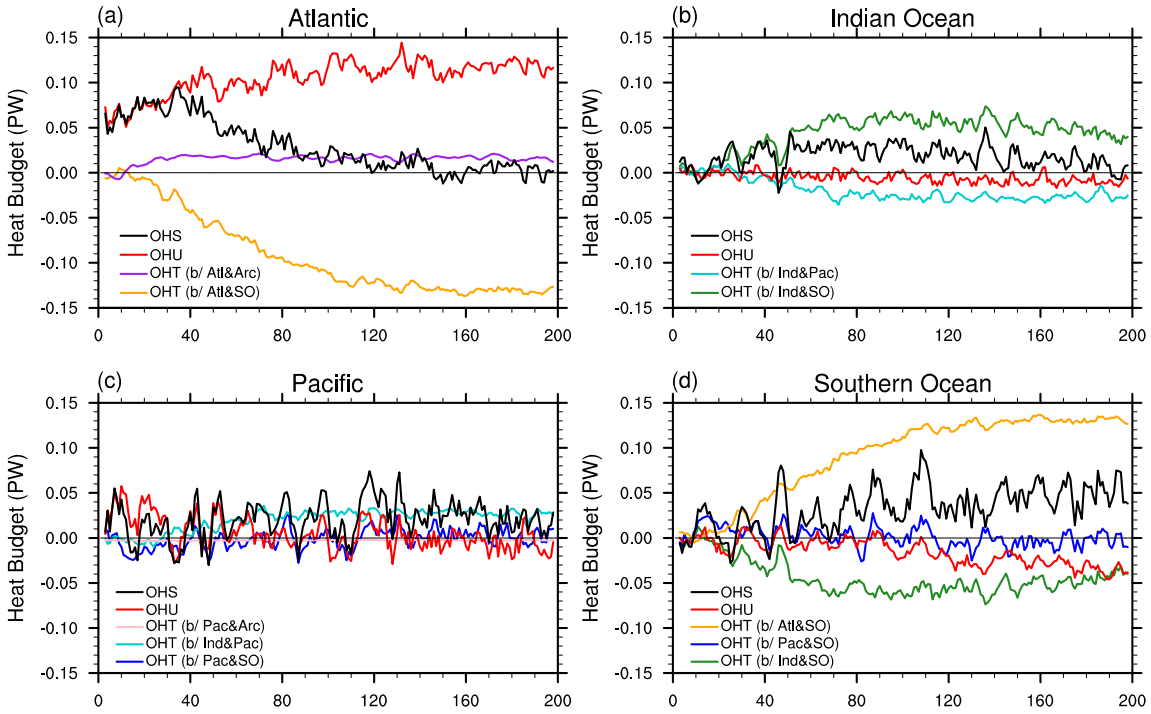

Figure 4.4: (a) Arctic sea ice loss induced changes (relative to the control) in annual mean ocean heat budget terms in the Atlantic: OHS (black), OHU (red), OHT at the Atlantic and Arctic boundary (purple), and at the Atlantic and Southern Ocean boundary (gold). (b) Arctic sea ice loss induced changes in annual mean ocean heat budget terms in the Indian Ocean: OHS (black), OHU (red), OHT at the Indian Ocean and Pacific boundary (cyan), and OHT at the Indian Ocean and Southern Ocean boundary (green). (c) Arctic sea ice loss induced changes in annual mean ocean heat budget terms in the Pacific: OHS (black), OHU (red), OHT at the Pacific and Arctic boundary (pink), and OHT at the boundary of the Pacific and Southern Oceans (blue), and OHT at the boundary of the Indian and Pacific Oceans [cyan; same as the cyan curve in (b)]. (d) Arctic sea ice loss induced changes in annual mean ocean heat budget terms in Southern Ocean: OHS (black), OHU (red), OHT at the boundary of the Atlantic and Southern Oceans [gold; same as the orange curve in (a)], and OHT at the boundary of the Indian and Southern Oceans [green; same as the green curve in (b)], and OHT at the boundary of the Pacific and Southern Oceans [blue; same as the blue curve in (c)]. For a basin, a positive OHT indicates an oceanic heat import while a negative OHT indicates an oceanic heat export.

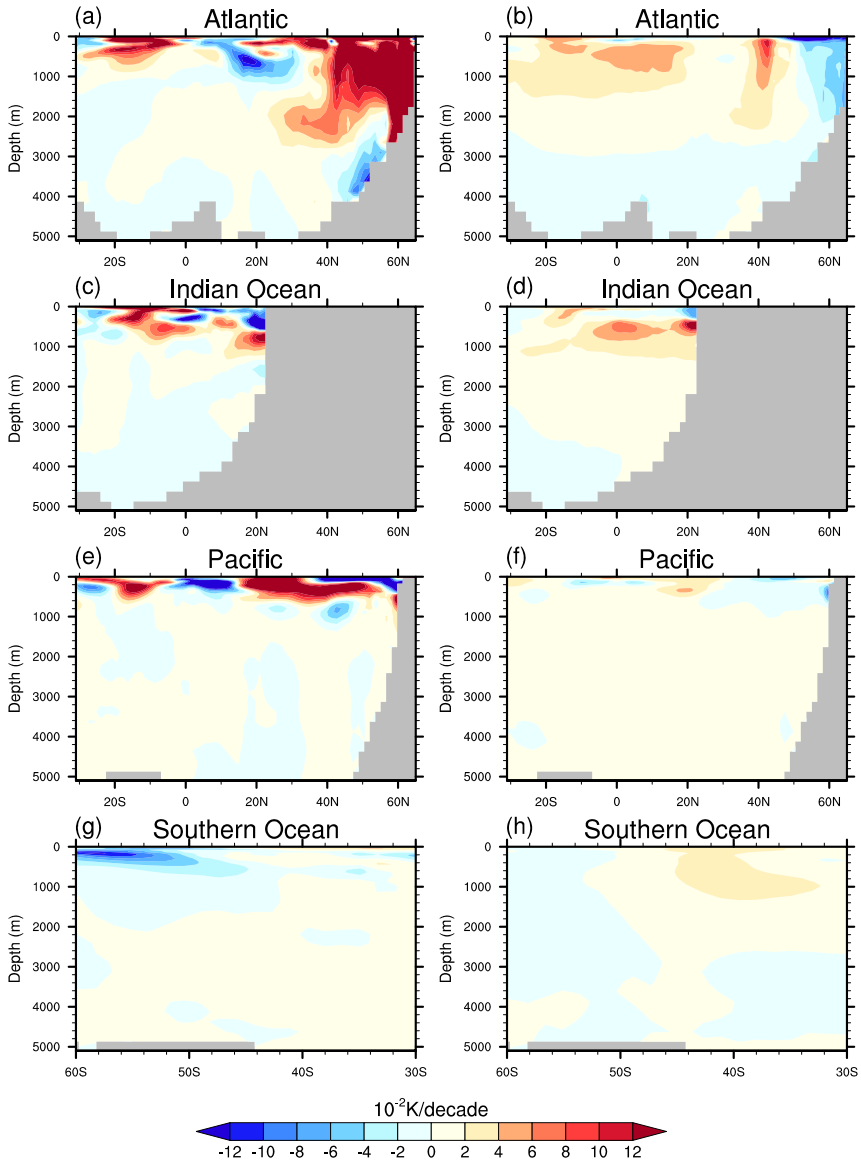

Figure 4.5: (left column) Arctic sea ice loss induced annual and zonal mean temperature trends (relative to the control) over the first 10 years in the (a) Atlantic, (b) Indian Ocean, (c) Pacific and (d) Southern Ocean. (right column) Similar to the left column but for the temperature trends over the later 100 years.

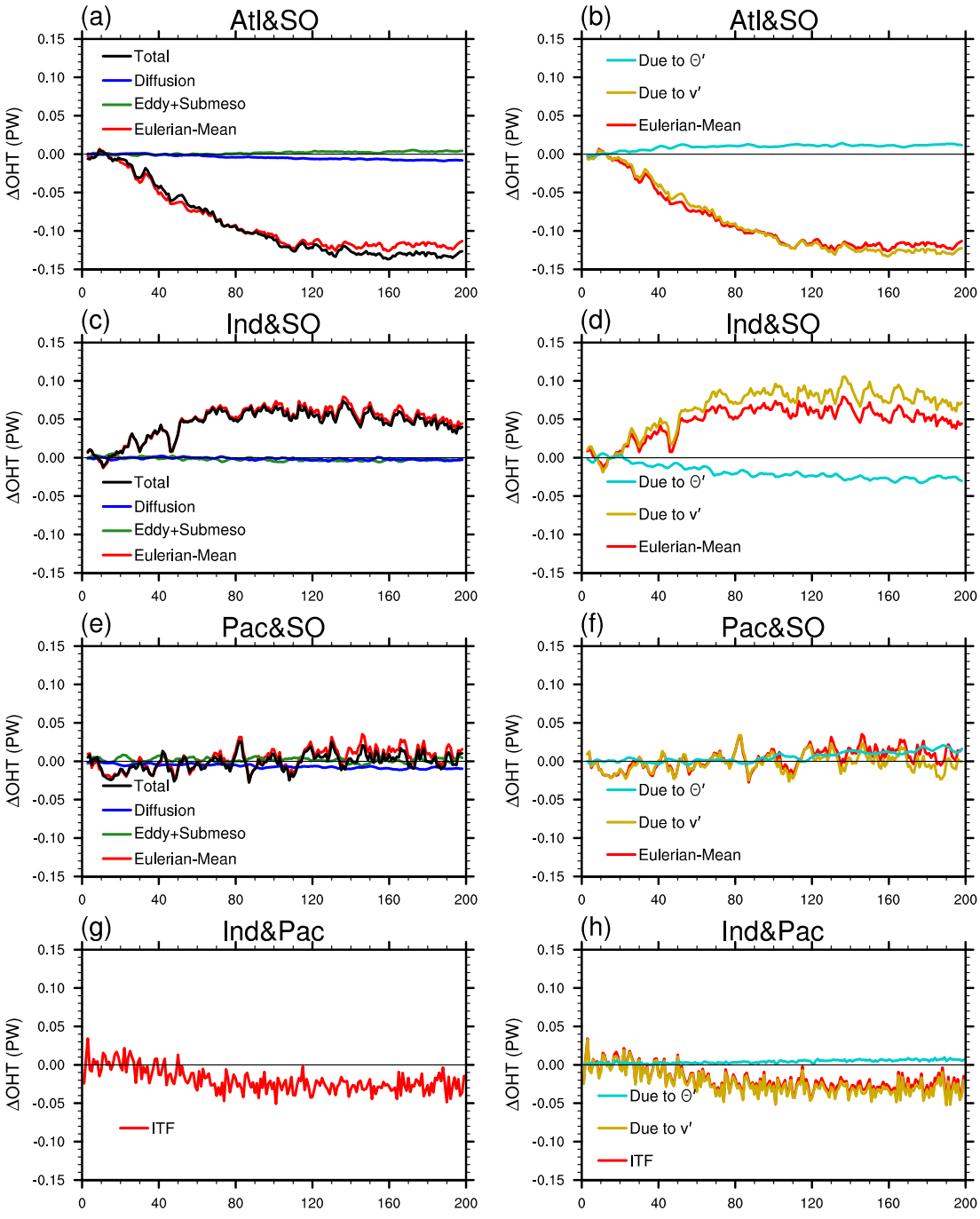
(a)
Atl&SO
(b)
Atl&SO
(c)
Ind&SO
(d)
Ind&SO
(e)
Pac&SO
(f)
Pac&SO
(g)
Ind&Pac
(h)
Ind&Pac
ΔOHT (PW)
0.15
0.10
0.05
0.00
-0.05
-0.10
-0.15
0
40
80
120
160
200
Total
Diffusion
Eddy+Submeso
Eulerian-Mean
Due to Θ′
Due to v′
ITF

Figure 4.6: (a) Arctic sea ice loss induced changes (relative to the control) in annual mean northward ocean heat transport at the boundary of the Southern and Atlantic Oceans (positive: from the Southern Ocean to the Atlantic): total (black) and the components induced by diffusion processes (blue), mesoscale and sub-mesoscale eddies (green) and Eulerian mean flow (red). (b) Replot of ocean heat transports by the Eulerian mean flow (red) in (a), the ocean-circulation driven component (brown) and the temperature driven component (cyan). (c) and (d): as in (a) and (b) but for changes in annual mean northward ocean heat transport at the boundaries between the Southern and Indian Oceans and between the Southern and Pacific Oceans, respectively. (g) Changes in the ITF induced ocean heat transport (positive: from the Pacific to Indian Ocean). (h) Replot of the ITF induced heat transport (red) in (g), the ocean-circulation driven component (brown) and the temperature driven component (cyan).

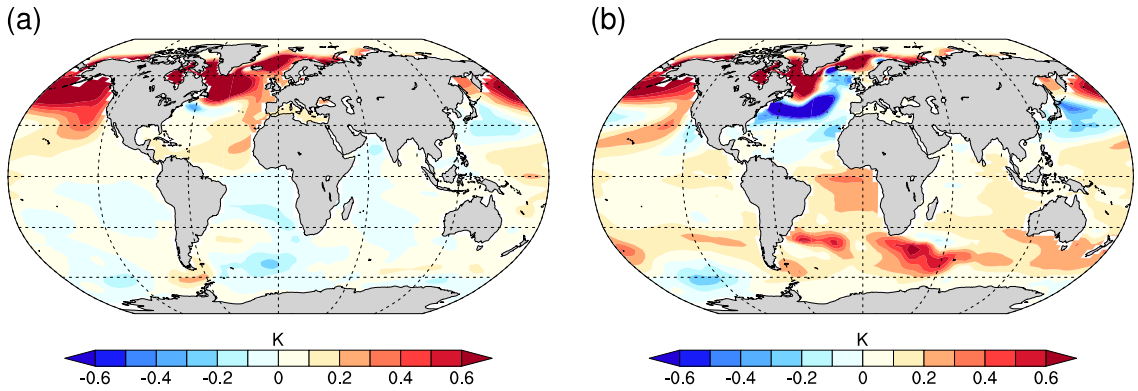

Figure 4.7: Changes in sea surface temperature (SST, relative to the control) for the ensemble mean of the Arctic sea ice perturbation simulation during (a) the first 10 years and (b) the later 100 years.

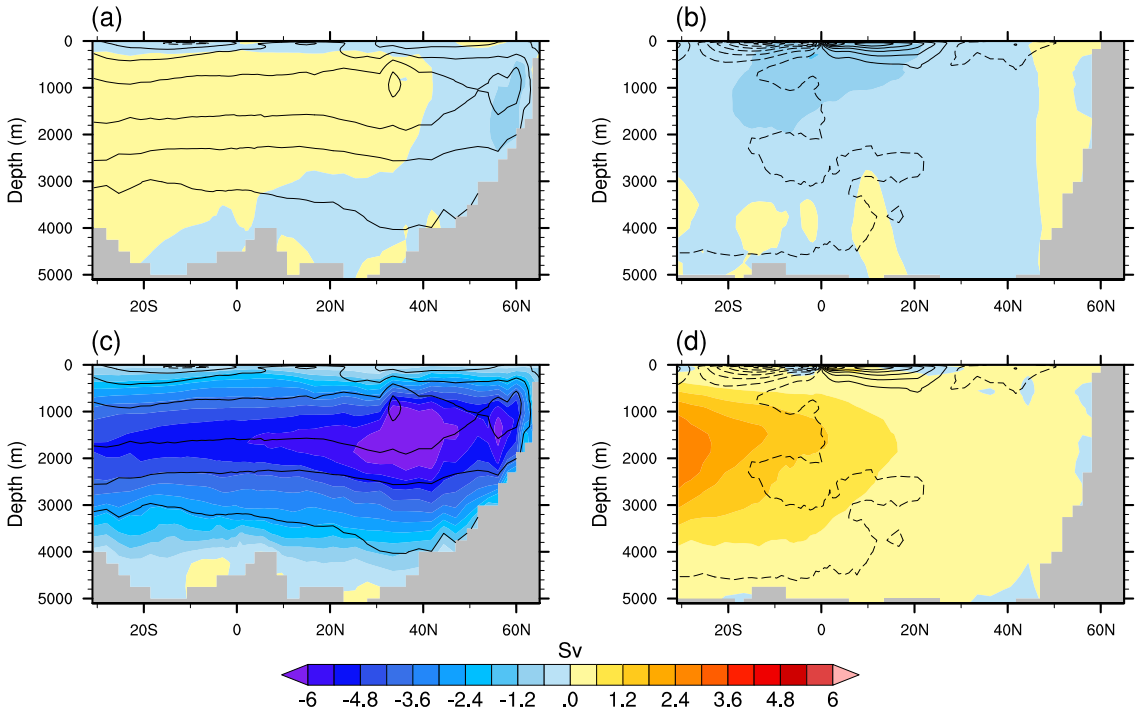

Figure 4.8: (left column) Arctic sea ice loss induced changes (relative to the control) in annual mean AMOC in the Atlantic over (a) the first 10 years and (c) the later 100 years. (right column) As in the left column but the MOC changes in the Indo-Pacific Ocean. Annual mean MOC climatology from control run in each ocean basin is shown in each panel [contours in Sv, with a contour interval of 5 Sv, zero contours thickened and solid (dashed) contours indicating positive (negative) values].

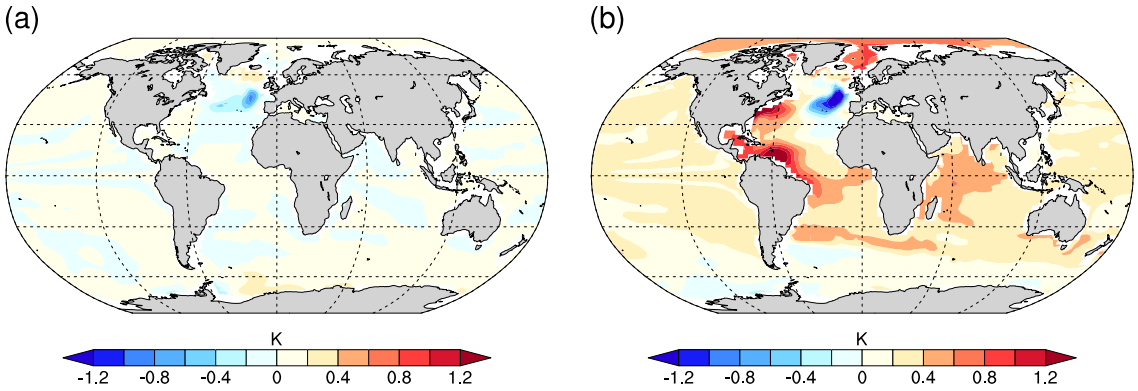

Figure 4.9: Changes in ocean temperature (relative to the control) at the 1000-m level over (a) the first 10 years and (b) the last 100 years.

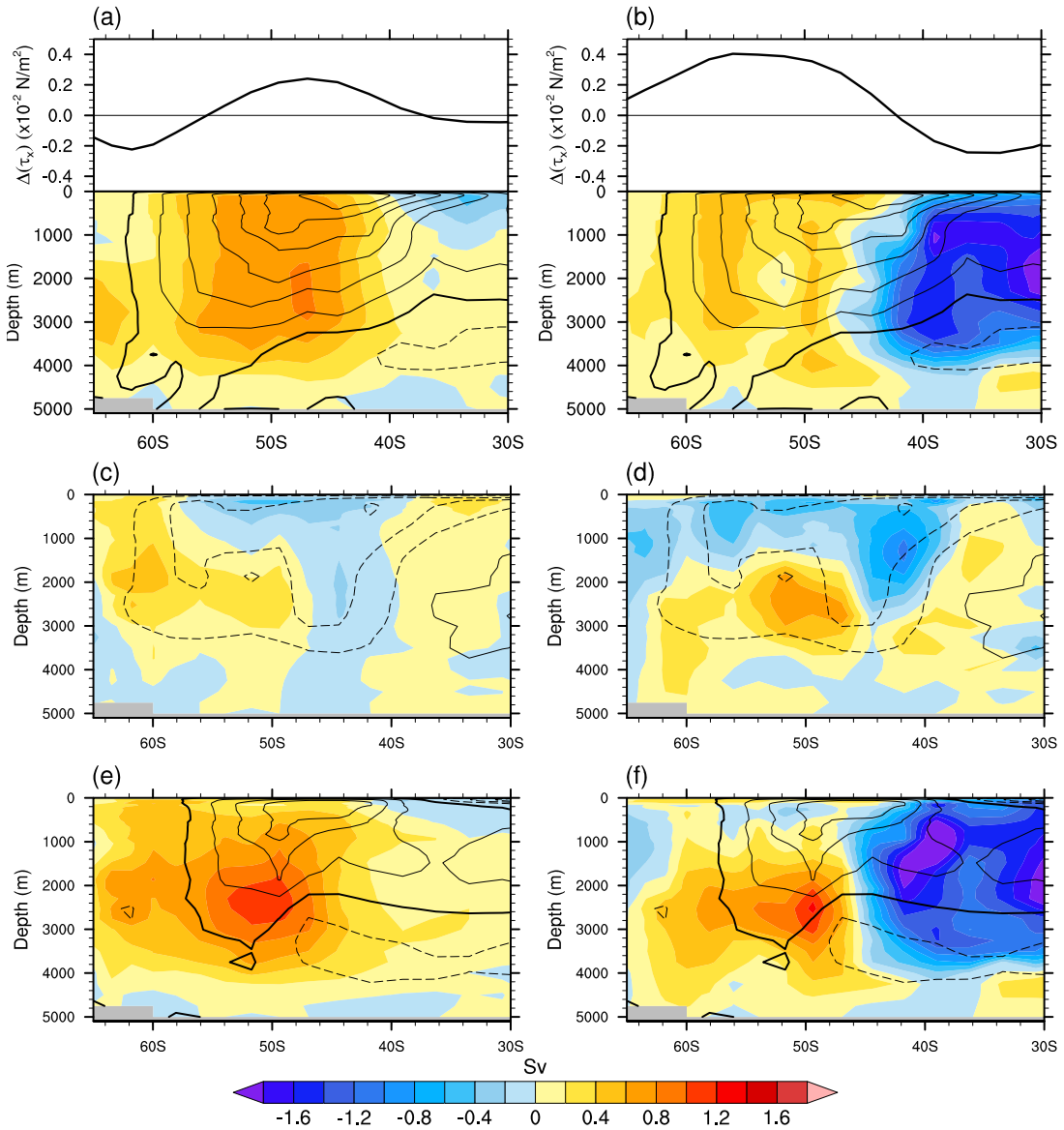

Figure 4.10: (left column) Arctic sea ice loss induced changes (relative to the control) in annual mean (a) Eulerian mean, (c) eddy-induced, and (e) residual MOCs (shading in Sv) in the Southern Ocean during the first 10 years. (right column) As in the left column but the MOC changes during the last 100 years. Annual mean MOC climatology from control run is shown in each panel [contours in Sv, with a contour interval of 5 Sv, zero contours thickened and solid (dashed) contours indicating positive (negative) values]. Arctic sea ice loss induced changes (relative to the control) in annual and zonal mean zonal surface wind stress curl during the first 10 years and the last 100 years in the experiment are attached on (a) and (b) respectively.

Chapter 5

Conclusions

Overall, multiple observation data sets and model simulations are employed in this dissertation to investigate the global ocean circulation changes and ocean heat uptake in a warming climate. Chapter 2 focuses on the changes in the Southern Ocean, where the ocean heat uptake and ocean heat content show a robust increasing trend in the past few decades. I explore the role of historical ozone changes, including both stratospheric ozone depletion and tropospheric ozone increases on Southern Ocean heat uptake and storage. Besides the regional changes in the Chapter 2, Chapter 3 highlights the importance of interbasin heat exchanges on modulating ocean heat anomaly in different ocean basins driven by anthropogenic aerosol and greenhouse gas changes. Chapter 3 also indicates the global effects of AMOC variations. Therefore, I further identify that the Arctic sea ice loss, which occurs in Northern Hemisphere polar regions, are of vital importance in modulating

global ocean circulations as well as ocean heat transport and storage in each ocean basin by affecting the AMOC strength.

In chapter 2, I investigate the effects of historical ozone changes on Southern Ocean heat uptake and storage. By comparing CESM1-CAM5-BGC historical simulations with fixed atmospheric ozone concentrations experiment, I find that atmospheric ozone changes can contribute to about 50% of the historical poleward intensification of Southern Hemisphere westerly winds during 1958-2005. Driven by the surface wind changes, the Deacon Cell also suggests a poleward intensification, which dominates the residual MOC in the Southern Ocean interior accompanying with oceanic heat redistribution. I then conduct an oceanic heat budget analysis, and I find that, due to atmospheric ozone changes, the Southern Ocean is taking heat mostly in 50°S-58°S while ocean heat storage peaks at around 44°S, which is due to Eulerian mean ocean circulation anomaly induced oceanic heat transport. I then calculate the full-depth integrated OHC over the Southern Ocean. The result suggests that the ozone induced warming contributes to about 22% of the historical warming during the past five decades. To understand the temperature and salinity changes from another perspective, I also conduct the heave and spiciness decomposition. I show that historical ozone forcing leads to spiciness changes with warming and salifying in the upper ocean at isopycnal outcrops but cooling and freshening along the Antarctica continental shelf. Meanwhile,

historical ozone changes also result in dipole-like pattern of isopycnal changes, with shoaling to the south of 62°S but deepening to the north of 50°S, corresponding to warming at high latitudes and deep-reaching warming tongue at lower latitudes.

However, ozone suggests distinct changes in the atmosphere, with depletion in the stratosphere but increases in the troposphere. Therefore, I further isolate the roles of different ozone changes on driving Southern Ocean interior warming in Chapter 2. I show that during 1955-2000, in the region of upper 2000 m within 30°S-60°S, around three-fifths of ozone induced Southern Ocean warming can be attributed to tropospheric ozone increases and the other two-fifths to stratospheric ozone depletion. Besides the different contributions, the mechanisms are also different. Particularly, tropospheric ozone increases cause Southern Ocean subsurface warming primarily via isopycnal deepening. They intensify the surface westerly winds over the Southern Ocean such that the wind-driven compression results in isopycnal deepening around 42°S and prompts warming there. On the other hand, stratospheric ozone depletion promotes warming in the Southern Ocean mainly through spiciness changes along isopycnals in the upper 500 m. In response to stratospheric ozone depletion, the net surface heat flux increases but freshwater flux decreases over the Southern Ocean between 40°S and 60°S, indicating that ocean is taking heat but losing freshwater which consequently contributes to the

warming and saltening spiciness changes in the isopycnal outcropping regions of the Southern Ocean.

Unlike the ozone changes that are mainly constrained in the Southern Hemisphere middle-high latitudes, another two important forcing agents: anthropogenic aerosol and greenhouse gases suggest effects over the world. In Chapter 3, I focus on their roles in altering global ocean circulations and ocean heat uptake. I identify that both anthropogenic aerosols and greenhouse gases can contribute to heat uptake, redistribution and storage changes over global oceans but via different mechanisms between 1861 and 2005. In particular, driven by anthropogenic aerosols, Indo-Pacific is exporting heat to the Southern Ocean while Atlantic is importing heat from the Southern Ocean accompanying with reduced OHU in the North Atlantic. OHT is dominated by the ocean circulation anomalies, which are slightly compensated by ocean temperature induced OHT changes. As a result, interbasin OHT changes are comparable to basin-integrated OHU changes for the Atlantic and Indo-Pacific Oceans, meaning that both terms play important roles in altering OHS in these ocean basins. On the contrary, as driven by anthropogenic greenhouse gases, excessive atmospheric heat is taken by the subpolar Atlantic while the Southern Ocean imports heat from the Atlantic but exports heat into the Indo-Pacific. Compared to aerosol forcing, ocean circulation anomaly induced interbasin OHT changes are strongly compensated by that due to temperature

anomaly under greenhouse gas forcing. Thereby, interbasin OHT changes are much smaller than basin-integrated OHU changes the rising anthropogenic greenhouse gases, producing the dominant role of regional atmosphere-ocean heat interactions in contributing to the OHS changes over individual basins.

As the aforementioned conclusions from Chapter 3, the North Atlantic is connected to the Indo-Pacific at low latitudes and even the Southern Ocean in the Southern Hemisphere by the AMOC. Therefore, in Chapter 4, I investigate the interbasin connection by exploring the remote effects of the Arctic sea ice loss, with a focus on the global ocean circulations and interbasin heat exchanges. By conducting ensemble sea ice perturbation simulations with a fully coupled climate model, I find that Arctic sea ice loss promotes OHU in the North Atlantic region while changes in OHS suggests distinct changes based on different timescale. During the first 10 years in the experiment, most of the taken heat is stored locally in the Atlantic with slight AMOC variations. Later, after the first decade, the AMOC starts to weaken along with effective heat redistribution. About one-third of the redistributed heat from the Atlantic is imported by the Indian Ocean, which is associated with the abnormal northward flow near the surface in the Indo-Pacific Oceans. Meanwhile, another important ocean circulation, the ITF, which connects the Indian Ocean and Pacific at the tropics is also weakened due to Arctic sea ice loss, leading to heat redistribution within the Indo-Pacific Oceans. As a result, either the

Indian or Pacific Ocean has a net import of oceanic heat from other basins as well an increase of basin-integrated OHS. The left two-thirds of the redistributed heat from the Atlantic remain in the Southern Ocean due to the anomalous southward flow at the boundary between the Southern Ocean and Atlantic/Indo-Pacific Oceans, which is driven by the weakened equatorward flank of the westerly winds in the Southern Hemisphere.

The research presented in this dissertation improves the understanding of changes in global ocean circulation, ocean heat uptake in the warming climate. The explanation of the mechanism also provides a methodology for reliable projections of climate change in the future. Nevertheless, there still exist important scientific questions to tackle. For example, how will winds and ocean circulations be altered in the Southern Ocean with a projected ozone hole recovery? How will the ozone-induced heat uptake and storage contribute to the Southern Ocean heat anomaly? Besides, what are the roles of anthropogenic aerosols and GHGs on global ocean heat anomaly in the future? Will the mechanism vary from historical to future climatology or even between different SSPs? To elucidate these questions, we need to understand the regional changes in ocean heat uptake and also basin-to-basin heat exchanges.

Bibliography

Bakker P, Schmittner A, Lenaerts JT, Abe-Ouchi A, Bi D, van den Broeke MR, Chan WL, Hu A, Beadling RL, Marsland SJ, Mernild SH (2016) Fate of the Atlantic Meridional Overturning Circulation: Strong decline under continued warming and Greenland melting. Geophys. Res. Lett., 43, 252-260.

Balmaseda MA, Mogensen K, Weaver AT (2013) Evaluation of the ECMWF ocean reanalysis system ORAS4. Quart. J. R. Meteorol. Soc., 139, 1132-1161.

Banerjee A, Fyfe JC, Polvani LM, Waugh D, Chang KL (2020) A pause in Southern Hemisphere circulation trends due to the Montreal Protocol. Nature, 579, 544–548.

Banks HT, Gregory JM (2006) Mechanisms of ocean heat uptake in a coupled climate model and the implications for tracer based predictions of ocean heat uptake. Geophys. Res. Lett., 33, L07 608, doi:10.1029/2005GL025352.

Bilbao RA, Gregory JM, Bouttes N, Palmer MD, Stott P (2019) Attribution of ocean temperature change to anthropogenic and natural forcings using the temporal, vertical and geographical structure. Clim. Dyn. 53, 5389–5413.

Bindoff NL, McDougall TJ (1994) Diagnosing climate change and ocean ventilation using hydrographic data. J. Phys. Oceanogr., 24, 1137–1152.

Bitz CM, Gent PR, Woodgate RA, Holland MM, Lindsay R (2006) The influence of sea ice on ocean heat uptake in response to increasing CO_2. J. Climate, 19, 2437–2450.

Bitz CM, Polvani LM (2012) Antarctic climate response to stratospheric ozone depletion in a fine resolution ocean climate model. Geophys. Res. Lett., 39, L20705, doi: 10.1029/2012GL053393.

Böning CW, Dispert A, Visbeck M, Rintoul SR, Schwarzkopf FU (2008) The response of the Antarctic Circumpolar Current to recent climate change. Nat. Geosci., 1, 864–869.

Bryan FO, Gent PR, Tomas R (2014) Can Southern Ocean eddy effects be parameterized in climate models? J. Climate, 27, 411–425.

Burgard C, Notz D (2017) Drivers of Arctic Ocean warming in CMIP5 models. Geophys. Res. Lett., 44, 4263-4271.

Cai WJ, Cowan T, Godfrey S, Wijffels S (2010) Simulations of processes associated with the fast warming rate of the southern midlatitude ocean. J. Climate, 23, 197–206.

Cessi P, Bryan K, Zhang R (2004) Global seiching of thermocline waters between the Atlantic and the Indian-Pacific Ocean Basins. Geophys. Res. Lett., 31, L04302.

Checa-Garcia R, Hegglin MI, Kinnison D, Plummer DA, Shine KP (2018) Historical tropospheric and stratospheric ozone radiative forcing using the CMIP6 database. Geophys. Res. Lett., 45, 3264–3273.

Chemke R, Polvani LM (2020) Using multiple large ensembles to elucidate the discrepancy between the 1979–2019 modeled and observed Antarctic sea ice trends. Geophys. Res. Lett., 47, e2020GL088339.

Chen C, Liu W, Wang G (2019) Understanding the uncertainty in the 21st century dynamic sea level projections: The Role of the AMOC. Geophys. Res. Lett., 46, 210–217.

Chen H, Morrison AK, Dufour CO, Sarmiento JL (2019) Deciphering patterns and drivers of heat and carbon storage in the Southern Ocean. Geophys. Res. Lett., 46, 3359–3367.

Cheng L, Trenberth KE, Fasullo J, Boyer T, Abraham J, Zhu J (2017) Improved estimates of ocean heat content from 1960 to 2015. Sci. Adv., 3, e1601 545, doi:10.1126/sciadv.1601545.

Chiang JC, Bitz CM (2005) Influence of high latitude ice cover on the marine Intertropical Convergence Zone. Clim. Dyn., 25, 477-496.

Church JA, Godfrey JS, Jackett DR, McDougall TJ (1991) A model of sea level rise caused by ocean thermal expansion. J. Climate, 4, 438–456.

Clément L, McDonagh EL, Marzocchi A, Nurser AG (2020) Signature of ocean warming at the mixed layer base. Geophys. Res. Lett., 47, e2019GL086269.

Comiso JC, Nishio F (2008) Trends in the sea ice cover using enhanced and compatible AMSR-E, SSM/I, and SMMR data, J. Geophys. Res., 113, C02S07.

Cooper OR, Parrish DD, Ziemke J, Balashov NV, Cupeiro M, Galbally IE, Gilge S, Horowitz L, Jensen NR, Lamarque JF, Naik V (2014) Global distribution and trends of tropospheric ozone: An observation-based reviewGlobal distribution and trends of tropospheric ozone. Elementa: Sci. Anthrop., 2, 000029.

Couldrey MP, Gregory JM, Boeira Dias F, Dobrohotoff P, Domingues CM, Garuba O, Griffies SM, Haak H, Hu A, Ishii M, Jungclaus J (2021) What causes the spread of model projections of ocean dynamic sea-level change in response to greenhouse gas forcing? Clim. Dyn. 56, 155–187.

Dalan F, Stone PH, Sokolov AP (2005) Sensitivity of the ocean's climate to diapycnal diffusivity in an EMIC. Part II: Global warming scenario. J. Climate, 18, 2482–2496.

Deser C, Tomas R, Alexander M, Lawrence D (2010) The seasonal atmospheric response to projected Arctic sea ice loss in the late twenty-first century. J. Climate, 23, 333-351.

Deser C, Tomas RA, Sun L (2015) The role of ocean–atmosphere coupling in the zonal-mean atmospheric response to Arctic sea ice loss. J. Climate, 28, 2168-2186.

Desbruyères D, McDonagh EL, King BA, Thierry V (2017) Global and full-depth ocean temperature trends during the early twenty-first century from Argo and repeat hydrography. J. Climate, 30, 1985–1997.

Dias FB, Fiedler R, Marsland SJ, Domingues CM, Clément L, Rintoul SR, Mcdonagh EL, Mata MM, Savita A (2020) Ocean heat storage in response to changing ocean circulation processes. J. Clim. 33, 9065–9082.

Ding Q, Schweiger A, L'Heureux M, Battisti DS, Po-Chedley S, Johnson NC, Blanchard-Wrigglesworth E, Harnos K, Zhang Q, Eastman R, Steig EJ

(2017) Influence of high-latitude atmospheric circulation changes on summertime Arctic sea ice. Nature Clim. Change, 7, 289-95.

Dittus AJ, Hawkins E, Wilcox LJ, Sutton RT, Smith CJ, Andrews MB, Forster PM (2020) Sensitivity of historical climate simulations to uncertain aerosol forcing. Geophys. Res. Lett. 47, e2019GL085806.

Good SA, Martin MJ, Rayner NA (2013) EN4: Quality controlled ocean temperature and salinity profiles and monthly objective analyses with uncertainty estimates. J. Geophys. Res. Oceans 118, 6704–6716.

Döös K, Nycander J, Coward AC (2008) Lagrangian decomposition of the Deacon Cell. J. Geophys. Res., 113, C07028

Döös K, Webb DJ (1994) The Deacon cell and the other meridional cells of the Southern Ocean. J. Phys. Oceanogr., 24, 429–442.

Drijfhout SS (2015) Global radiative adjustment after a collapse of the Atlantic meridional overturning circulation. Clim. Dyn., 45, 1789-1799.

Durack PJ, Gleckler PJ, Landerer FW, Taylor KE (2014) Quantifying underestimates of long-term upper-ocean warming. Nature Clim. Change, 4, 999–1005.

Durack PJ, Wijffels SE (2010) Fifty-year trends in global ocean salinities and their relationship to broad-scale warming. J. Climate, 23, 4342–4362.

Exarchou E, Kuhlbrodt T, Gregory JM, Smith RS (2015) Ocean heat uptake processes: A model intercomparison. J. Climate, 28, 887–908.

Eyring V, Bony S, Meehl GA, Senior CA, Stevens B, Stouffer RJ, Taylor KE (2016) Overview of the Coupled Model Intercomparison Project Phase 6 (CMIP6) experimental design and organization. Geosci. Model Dev., 9, 1937-1958.

Fahey D, Newman PA, Pyle JA, Safari B, Chipperfield MP, Karoly D, Kinnison DE, Ko M, Santee M, Doherty SJ (2018) Scientific Assessment of Ozone Depletion: 2018, Global Ozone Research and Monitoring Project – Report No. 58, 588 pp., Geneva, Switzerland.

Farman JC, Gardiner BG, Shanklin JD (1985) Large losses of total ozone in Antarctica reveal seasonal ClOx/NOx interaction. Nature, 315, 207-210.

Ferreira D, Marshall J, Bitz CM, Solomon S, Plumb A (2015) Antarctic ocean and sea ice response to ozone depletion: A two-time-scale problem. J. Climate, 28, 1206–1226.

Flynn CM, Mauritsen T (2020) On the climate sensitivity and historical warming evolution in recent coupled model ensembles. Atmos. Chem. Phys. 20, 7829–7842.

Francis JA, Chan W, Leathers DJ, Miller JR, Veron DE (2009) Winter Northern Hemisphere weather patterns remember summer Arctic sea-ice extent. Geophys. Res. Lett., 36, L07503

Frajka-Williams E (2015) Estimating the Atlantic overturning at 26°N using satellite altimetry and cable measurements. Geophys. Res. Lett., 42, 3458-3464.

Frölicher TL, Sarmiento JL, Paynter DJ, Dunne JP, Krasting JP, Winton M (2015) Dominance of the Southern Ocean in anthropogenic carbon and heat uptake in CMIP5 models. J. Climate, 28, 862–886.

Fyfe JC (2006) Southern Ocean warming due to human influence. Geophys. Res. Lett., 33, L19 701, doi:10.1029/2006GL027247.

Fyfe JC, Saenko OA, Zickfeld K, Eby M, Weaver AJ (2007) The role of poleward-intensifying winds on Southern Ocean warming. J. Climate, 20, 5391–5400.

Gao L, Rintoul SR, Yu W (2018) Recent wind-driven change in Subantarctic Mode Water and its impact on ocean heat storage. Nature Clim. Change, 8, 58–63.

Garuba OA, Klinger BA (2016) Ocean heat uptake and interbasin transport of the passive and redistributive components of surface heating. J. Climate, 29, 7507–7527.

Gent PR, Danabasoglu G (2011) Response to increasing Southern Hemisphere winds in CCSM4. J. Climate, 24, 4992–4998.

Gent PR, Mcwilliams JC (1990) Isopycnal mixing in ocean circulation models. J. Phys. Oceanogr., 20, 150–155.

Gille ST (2002) Warming of the Southern Ocean since the 1950s. Science, 295, 1275–1277.

Gillett NP, Shiogama H, Funke B, Hegerl G, Knutti R, Matthes K, Santer BD, Stone D, Tebaldi C (2016) The detection and attribution model intercomparison project (DAMIP v1. 0) contribution to CMIP6. Geosci. Model Dev., 9, 3685–3697 (2016).

Gillett NP, Thompson DWJ (2003) Simulation of recent Southern Hemisphere climate change. Science, 302, 273–275.

Good SA, Martin MJ, Rayner NA (2013) EN4: Quality controlled ocean temperature and salinity profiles and monthly objective analyses with uncertainty estimates. J. Geophys. Res. Oceans, 118, 6704-6716.

Gouretski V, Reseghetti F (2010) On depth and temperature biases in bathythermograph data: Development of a new correction scheme based on analysis of a global ocean database. Deep Sea Research Part I: Oceanographic Research Papers.; 57, 812-833.

Gregory JM (2000) Vertical heat transports in the ocean and their effect on time-dependent climate change. Clim. Dyn., 16, 501–515.

Gregory JM, and Coauthors (2005) A model intercomparison of changes in the Atlantic thermohaline circulation in response to increasing atmospheric CO2 concentration. Geophys. Res. Lett., 32, L12703

Gregory JM, Church JA, Boer GJ, Dixon KW, Flato GM, Jackett DR, Lowe JA, O'farrell SP, Roeckner E, Russell GL, Stouffer RJ, Winton M (2001) Comparison of results from several AOGCMs for global and regional sea-level change 1900–2100. Clim. Dyn., 18, 225–240.

Gregory JM, Bouttes N, Griffies SM, Haak H, Hurlin WJ, Jungclaus J, Kelley M, Lee WG, Marshall J, Romanou A, Saenko OA, Stammer D, Winton M (2016) The Flux-Anomaly-Forced Model Intercomparison Project (FAFMIP) contribution to CMIP6: investigation of sea-level and ocean climate change in response to CO_2 forcing. Geosci. Model Dev., 9, 3993–4017.

Griffies SM, Winton M, Anderson WG, Benson R, Delworth TL, Dufour CO, Dunne JP, Goddard P, Morrison AK, Rosati A, Wittenberg AT, Yin J,

Zhang R (2015) Impacts on ocean heat from transient mesoscale eddies in a hierarchy of climate models. J. Climate, 28, 952–977.

Grise KM, Polvani LM, Tselioudis G, Wu Y, Zelinka MD (2013) The ozone hole indirect effect: Cloud-radiative anomalies accompanying the poleward shift of the eddy-driven jet in the Southern Hemisphere. Geophys. Res. Lett., 40, 3688-3692.

Grotefendt K, Logemann K, Quadfasel D, Ronski S (1998) Is the Arctic Ocean warming? J. Geophys. Res.: Oceans, 103, 27679-27687.

Gupta AS, Jourdain NC, Brown JN, Monselesan D (2013) Climate drift in the CMIP5 models. J. Clim. 26, 8597–8615.

Haigh JD (1994) The role of stratospheric ozone in modulating the solar radiative forcing of climate. Nature, 370, 544–546.

Häkkinen S, Rhines PB, Worthen DL (2015) Heat content variability in the North Atlantic Ocean in ocean reanalyses. Geophys. Res. Lett., 42, 2901–2909.

Han L, Yan XH (2018) Warming in the Agulhas region during the global surface warming acceleration and slowdown. Sci. Rep., 8, 13 452.

Hande LB, Siems ST, Manton MJ (2012) Observed trends in wind speed over the Southern Ocean. Geophys. Res. Lett., 39, L11 802, doi:10.1029/2012GL051734.

Hassan T, Allen RJ, Liu W and Randles CA (2021) Anthropogenic aerosol forcing of the Atlantic meridional overturning circulation and the associated mechanisms in CMIP6 models. Atmos. Chem. Phys., 21, 5821-5846

Hausmann U, Czaja A, Marshall J (2016) Estimates of air–sea feedbacks on sea surface temperature anomalies in the Southern Ocean. J. Climate, 29, 439-454.

Hausmann U, Czaja A, Marshall J (2017) Mechanisms controlling the SST air-sea heat flux feedback and its dependence on spatial scale. Clim. Dyn. 48, 1297–1307.

He C, Liu Z, Hu A (2019) The transient response of atmospheric and oceanic heat transports to anthropogenic warming. Nat. Clim. Chang., 9, 222–226.

He C, Liu Z, Zhu J, Zhang J, Gu S, Otto-Bliesner BL, Brady E, Zhu C, Jin Y, Sun J (2020) North Atlantic subsurface temperature response controlled by effective freshwater input in "Heinrich" events. Earth Planet. Sci. Lett., 539,116247.

Hersbach H, Peubey C, Simmons A, Berrisford P, Poli P, Dee D (2015) ERA-20CM: A twentieth-century atmospheric model ensemble. Quart. J. R. Meteorol. Soc., 141, 2350-2375.

Hieronymus M, Nycander J (2013) The budgets of heat and salinity in NEMO. Ocean Modell., 67, 28–38.

Holland MM, Bailey DA, Briegleb BP, Light B, Hunke E (2012) Improved sea ice shortwave radiation physics in CCSM4: The impact of melt ponds and aerosols on Arctic sea ice. J. Climate, 25, 1413–1430.

Hu S, Sprintall J (2017) Observed strengthening of interbasin exchange via the Indonesian seas due to rainfall intensification. Geophys. Res. Lett., 44, 1448-1456.

Huang RX, Cane MA, Naik N, Goodman P (2000) Global adjustment of the thermocline in response to deepwater formation. Geophys. Res. Lett., 27, 759-762.

Hurrell JW et al (2013) The Community Earth System Model: A framework for collaborative research. B. Am. Meteorol. Soc., 94, 1339–1360.

Irving DB, Wijffels S, Church JA (2019) Anthropogenic aerosols, greenhouse gases, and the uptake, transport, and storage of excess heat in the climate system. Geophys. Res. Lett. 46, 4894–4903.

Irving D, Hobbs W, Church J, Zika J (2021) A mass and energy conservation analysis of drift in the CMIP6 ensemble. J. Clim. 34, 3157–3170.

Ishii M, Shouji A, Sugimoto S, Matsumoto T (2005) Objective analyses of SST and marine meteorological variables for the 20th century using COADS and the Kobe Collection. Int. J. Climatol. 25, 865–879.

Jackett DR, McDougall TJ (1997) A neutral density variable for the world's oceans. J. Phys. Oceanogr., 27, 237–263.

Jackson LC, Wood RA (2020) Fingerprints for Early Detection of Changes in the AMOC. J. Climate, 33, 7027-7044.

Johnson HL, Marshall DP (2002) A theory for the surface Atlantic response to thermohaline variability. J. Phys. Oceanogr., 32, 1121-1132.

Jungclaus JH, Haak H, Latif M, Mikolajewicz U (2005) Arctic–North Atlantic interactions and multidecadal variability of the meridional overturning circulation. J. Climate, 18, 4013-4031.

Kalnay E, Kanamitsu M, Kistler R, Collins W, Deaven D, Gandin L, Iredell M, Saha S, White G, Woollen J, Zhu Y (1996) The NCEP/NCAR 40-year reanalysis project. Bull. Amer. Meteor. Soc., 77, 437-472.

Kawase M (1987) Establishment of deep ocean circulation driven by deep-water production. J. Phys. Oceanogr 17, 2294–2317

Kay JE, Deser C, Phillips A, Mai A, Hannay C, Strand G, Arblaster JM, Bates SC, Danabasoglu G, Edwards J, Holland M, Kushner P, Lamarque JF, Lawrence D, Lindsay K, Middleton A, Munoz E, Neale R, Oleson K, Polvani L, Vertenstein M (2015) The Community Earth System Model (CESM) large ensemble project: A community resource for studying climate change in the presence of internal climate variability. Bull. Amer. Meteor. Soc., 96, 1333–1349.

Kobayashi S, Ota Y, Harada Y, Ebita A, Moriya M, Onoda H, Onogi K, Kamahori H, Kobayashi C, Endo H, Miyaoka K (2015) The JRA-55 reanalysis: General specifications and basic characteristics. J. Meteor. Soc. Japan, 93, 5-48.

Köhl A (2014) Detecting processes contributing to interannual halosteric and thermosteric sea level variability. J. Climate, 27, 2417–2426.

Köhl A (2020) Evaluating the GECCO3 1948–2018 ocean synthesis–a configuration for initializing the MPI-ESM climate model. Quart. J. R. Meteorol. Soc., 146, 2250– 2273.

Kostov Y, Armour KC, Marshall J (2014) Impact of the Atlantic meridional overturning circulation on ocean heat storage and transient climate change. Geophys. Res. Lett., 41,2108-2116.

Kuhlbrodt T, Gregory JM (2012) Ocean heat uptake and its consequences for the magnitude of sea level rise and climate change. Geophys. Res. Lett., 39, L18 608, doi:10.1029/ 2012GL052952.

Landrum LL, Holland MM, Raphael MN, Polvani LM (2017) Stratospheric ozone depletion: An unlikely driver of the regional trends in Antarctic sea ice in austral fall in the late twentieth century. Geophys. Res. Lett., 44, 11062–11070.

Langematz U (2000) An estimate of the impact of observed ozone losses on stratospheric tempera-ture. Geophys. Res. Lett., 27, 2077–2080.

Large WG, McWilliams JC, Doney SC (1994) Oceanic vertical mixing: A review and a model with a nonlocal boundary layer parameterization. Rev. Geophys., 32, 363–403.

Lawrence DM, Oleson KW, Flanner MG, Fletcher CG, Lawrence PJ, Levis S, Swenson SC, Bonan GB (2012) The CCSM4 land simulation, 1850–2005: Assessment of surface climate and new capabilities. J. Climate, 25, 2240–2260.

Lee SK, Park W, Baringer MO, Gordon AL, Huber B, Liu Y (2015) Pacific origin of the abrupt increase in Indian Ocean heat content during the warming hiatus. Nature Geosci., 8, 445-449.

Lee SY, Chiang JC, Matsumoto K, Tokos KS (2011) Southern Ocean wind response to North Atlantic cooling and the rise in atmospheric CO2: Modeling perspective and paleoceanographic implications. Paleoceanography, 26, PA1214.

Levermann A, Mignot J, Nawrath S, Rahmstorf S (2007) The role of northern sea ice cover for the weakening of the thermohaline circulation under global warming. J. Climate, 20, 4160-4171.

Levitus S, Antonov JI, Boyer TP, Baranova OK, Garcia HE, Locarnini RA, Mishonov AV, Reagan JR, Seidov D, Yarosh ES, Zweng MM (2012) World ocean heat content and thermosteric sea level change (0–2000 m),

1955–2010. Geophys. Res. Lett., 39, L10 603, doi:10.1029/2012GL051106.

Li D, Zhang R, Knutson T (2018) Comparison of mechanisms for low-frequency variability of summer Arctic sea ice in three coupled models. J. Climate, 31, 1205-1226.

Li H, Fedorov AV (2021) Persistent freshening of the Arctic Ocean and changes in the North Atlantic salinity caused by Arctic sea ice decline. Clim. Dyn., 57, 2995-3013.

Li H, Fedorov AV, Liu W (2021) AMOC stability and diverging response to Arctic sea ice decline in two climate models. J. Climate, 34, 5443-5460.

Li S, Liu W (2022) Impacts of Arctic sea ice loss on global ocean circulations and interbasin ocean heat exchanges. Clim. Dyn. 59, 2701–2716.

Li S, Liu W, Lyu K, Zhang X (2021) The effects of historical ozone changes on Southern Ocean heat uptake and storage. Clim. Dyn., 22, 1-7.

Li X, Holland DM, Gerber EP, Yoo C (2014) Impacts of the north and tropical Atlantic Ocean on the Antarctic Peninsula and sea ice, Nature, 505, 538–542.

Liu W, Fedorov AV (2019) Global impacts of Arctic sea ice loss mediated by the Atlantic meridional overturning circulation. Geophys. Res. Lett., 46, 944–952.

Liu, W., Fedorov, AV (2021) Interaction between Arctic sea ice and the Atlantic meridional overturning circulation in a warming climate. Clim. Dyn., 1-17.

Liu W, Fedorov AV, Sévellec F (2019) The mechanisms of the Atlantic meridional overturning circulation slowdown induced by Arctic sea ice decline. J. Climate, 32, 977-996.

Liu W, Fedorov AV, Xie S-P, Hu S (2020) Climate impacts of a weakened Atlantic Meridional Overturning Circulation in a warming climate. Science Advances. 6, eaaz4876.

Liu W, Hegglin MI, Checa-Garcia R, Li S, Gillett NP, Lyu K, Zhang X, Swart NC (2022) Stratospheric ozone depletion and tropospheric ozone

increases drive Southern Ocean interior warming. Nat. Clim. Change 12, 365–372.

Liu W, Lu J, Xie SP, Fedorov A (2018) Southern Ocean heat uptake, redistribution, and storage in a warming climate: The role of meridional overturning circulation. J. Climate, 31, 4727–4743.

Liu W, Xie S-P, Liu Z, Zhu J (2017). Overlooked possibility of a collapsed Atlantic Meridional Overturning Circulation in warming climate. Science Advances, 3, e1601666.

Liu W, Xie SP, Lu J (2016) Tracking ocean heat uptake during the surface warming hiatus. Nat. Commun., 7, 10 926.

Llovel W, Terray L (2016) Observed southern upper-ocean warming over 2005–2014 and associated mechanisms. Environ. Res. Lett., 11, 124 023, doi:10.1088/1748-9326/11/12/124023.

Lyu K, Zhang X, Church JA, Wu Q (2020) Processes responsible for the Southern Hemisphere ocean heat uptake and redistribution under anthropogenic warming. J. Climate, 33, 3787–3807.

Ma X, Liu W, Allen RJ, Huang G, Li X (2020) Dependence of regional ocean heat uptake on anthropogenic warming scenarios. Sci. Adv., 6, eabc0303.

Manabe S, Stouffer RJ, Spelman MJ, Bryan K (1991) Transient responses of a coupled ocean-atmosphere model to gradual changes of atmospheric CO_2. Part I. Annual Mean Response. J. Climate, 4, 785–818.

Marshall DP, Zanna L (2014) A conceptual model of ocean heat uptake under climate change. J. Climate., 27, 8444-8465.

Marshall GJ (2003) Trends in the Southern Annular Mode from Observations and Reanalyses. J. Climate, 16, 4134–4143.

Marshall J, Armour KC, Scott JR, Kostov Y, Hausmann U, Ferreira D, Shepherd TG, Bitz CM (2014) The ocean's role in polar climate change: asymmetric Arctic and Antarctic responses to greenhouse gas and ozone forcing. Philos. T. R. Soc. A., 372, 20130 040.

Marshall J, Radko T (2003) Residual-mean solutions for the Antarctic Circumpolar Current and its associated overturning circulation. J. Phys. Oceanogr., 33, 2341–2354.

Marshall J, Scott JR, Armour KC, Campin JM, Kelley M, Romanou A (2015) The ocean's role in the transient response of climate to abrupt greenhouse gas forcing. Clim. Dyn., 44, 2287–2299.

McManus JF, Francois R, Gherardi JM, Keigwin LD, Brown-Leger S (2004) Collapse and rapid resumption of Atlantic meridional circulation linked to deglacial climate changes. Nature, 428, 834–837.

Meehl GA, Arblaster JM, Bitz CM, Chung CTY, Tang H (2016) Antarctic sea-ice expansion between 2000 and 2014 driven by tropical Pacific decadal climate variability, Nat. Geosci., 9, 590–595.

Meehl GA, Arblaster JM, Chung CTY, Holland MM, DuVivier A, Thompson L, Yang D, Bitz CM, (2019) Sustained ocean changes contributed to sudden Antarctic sea ice retreat in late 2016. Nat. Commun., 10, 14.

Menary MB, Robson J, Allan RP, Booth BB, Cassou C, Gastineau G, Gregory J, Hodson D, Jones C, Mignot J, Ringer M (2020) Aerosol-forced AMOC changes in CMIP6 historical simulations. Geophys. Res. Lett. 47, e2020GL088166.

Morrison AK, Griffies SM, Winton M, Anderson WG, Sarmiento JL (2016) Mechanisms of Southern Ocean heat uptake and transport in a global eddying climate model. J. Climate, 29, 2059–2075.

Morrison AK, Saenko OA, Hogg AM, Spence P (2013) The role of vertical eddy flux in Southern Ocean heat uptake. Geophys. Res. Lett., 40, 5445–5450.

Neale RB et al (2010) Description of the NCAR Community Atmosphere Model (CAM 5.0). NCAR Tech. Note NCAR/TN-486, NCAR, 264 pp.

Newsom ER, Thompson AF (2018) Reassessing the role of the Indo-Pacific in the ocean's global overturning circulation. Geophys. Res. Lett. 45, 12422–12431.

Oudar T, Sanchez-Gomez E, Chauvin F, Cattiaux J, Terray L, Cassou C (2017) Respective roles of direct GHG radiative forcing and induced Arctic sea

ice loss on the Northern Hemisphere atmospheric circulation. Clim. Dyn., 49, 3693-3713.

Overland JE, Wang M (2010) Large-scale atmospheric circulation changes are associated with the recent loss of Arctic sea ice. Tellus A: Dyn. Meteorol. Oceanogr., 62, 1-9.

Park HS, Lee S, Son SW, Feldstein SB, Kosaka Y (2015) The impact of poleward moisture and sensible heat flux on Arctic winter sea ice variability. J. Climate, 28, 5030-5040.

Paynter D, Frölicher TL (2015) Sensitivity of radiative forcing, ocean heat uptake, and climate feedback to changes in anthropogenic greenhouse gases and aerosols. J. Geophys. Res. Atmos. 120, 9837–9854.

Pedro JB, Jochum M, Buizert C, He F, Barker S, Rasmussen SO (2018) Beyond the bipolar seesaw: Toward a process understanding of interhemispheric coupling. Quat. Sci. Rev., 192, 27-46.

Peings Y, Magnusdottir G (2014) Response of the wintertime Northern Hemisphere atmospheric circulation to current and projected Arctic sea ice decline: A numerical study with CAM5. J. Climate, 27, 244-264.

Polvani LM, Waugh DW, Correa GJ, Son SW (2011) Stratospheric ozone depletion: The main driver of twentieth-century atmospheric circulation changes in the Southern Hemisphere. J. Climate, 24, 795–812.

Previdi M, Polvani LM (2014) Climate system response to stratospheric ozone depletion and recovery. Quart. J. R. Meteorol. Soc., 140, 2401–2419.

Purich A, England MH (2019) Tropical teleconnections to Antarctic sea ice during austral spring 2016 in coupled pacemaker experiments, Geophys. Res. Lett., 46, 6848– 6858.

Purkey SG, Johnson GC (2010) Warming of global abyssal and deep Southern Ocean waters between the 1990s and 2000s: Contributions to global heat and sea level rise budgets. J. Climate, 23, 6336–6351.

Ramaswamy V, Chanin ML, Angell J, Barnett J, Gaffen D, Gelman M, Keckhut P, Koshelkov Y, Labitzke K, Lin JJ, O'Neill A, Nash J, Randel W, Rood R, Shine K, Shiotani M, Swinbank R (2001) Stratospheric

temperature trends: Observations and model simulations. Rev. Geophys., 39, 71–122.

Rathore S, Bindoff NL, Phillips HE, Feng M (2020) Recent hemispheric asymmetry in global ocean warming induced by climate change and internal variability. Nat. Comm. 11, 2008.

Robson J, Ortega P, Sutton R (2016) A reversal of climatic trends in the North Atlantic since 2005. Nat. Geosci. 9, 513–517.

Rhein M et al (2013) Observations: ocean. in: Climate change 2013: The Physical Science Basis. Contribution of Working Group I to the Fifth Assessment Report of the Inter-governmental Panel on Climate Change [Stocker TF, Qin D, Plattner GK, Tignor M, Allen SK, Boschung J, Nauels A, Xia Y, Bex V, Midgley PM (eds.)]. Cambridge University Press, Cambridge, United Kingdom and New York, NY, USA, pp. 255–316.

Ring MJ, Plumb RA (2008) The Response of a Simplified GCM to Axisymmetric Forcings: Applicability of the Fluctuation–Dissipation Theorem. J. Atmos. Sci., 65, 3880-3898.

Rinke A, Dethloff K, Dorn W, Handorf D, Moore JC (2013) Simulated Arctic atmospheric feedbacks associated with late summer sea ice anomalies. J. Geophys. Res.: Atmos., 118, 7698-7714.

Roach LA, Dörr J, Holmes CR, Massonnet F, Blockley EW, Notz D, et al. (2020) Antarctic sea ice area in CMIP6. Geophys. Res. Lett., 47, e2019GL086729.

Roberts CD, Jackson L, McNeall D (2014) Is the 2004–2012 reduction of the Atlantic meridional overturning circulation significant? Geophys. Res. Lett., 41, 3204–3210.

Roemmich D, Church J, Gilson J, Monselesan D, Sutton P, Wijffels S (2015) Unabated planetary warming and its ocean structure since 2006. Nat. Clim. Chang., 5, 240–245.

Rose BE, Armour KC, Battisti DS, Feldl N, Koll DD (2014) The dependence of transient climate sensitivity and radiative feedbacks on the spatial pattern of ocean heat uptake. Geophys. Res. Lett., 41, 1071–1078.

Rosenblum E, I Eisenman (2017) Sea Ice Trends in Climate Models Only Accurate in Runs with Biased Global Warming. J. Climate, 30, 6265–6278.

Rotstayn LD, Collier MA, Jeffrey SJ, Kidston J, Syktus JI, Wong KK (2013) Anthropogenic effects on the subtropical jet in the Southern Hemisphere: aerosols versus long-lived greenhouse gases. Environ. Res. Lett. 8, 014030.

Rowland FS (1989) Chlorofluorocarbons and the depletion of stratospheric ozone. Am. Sci., 77, 36-45.

Sallée JB (2018) Southern Ocean warming. Oceanography, 31, 52–62.

Sallée JB, Shuckburgh E, Bruneau N, Meijers AJ, Bracegirdle TJ, Wang Z, Roy T (2013) Assessment of Southern Ocean water mass circulation and characteristics in CMIP5 models: Historical bias and forcing response. J. Geophys. Res.: Oceans, 118, 1830–1844.

Schneider DP, Deser C (2018) Tropically driven and externally forced patterns of Antarctic sea ice change: Reconciling observed and modeled trends. Clim. Dyn., 50, 4599-4618.

Screen JA, Simmonds I (2010) The central role of diminishing sea ice in recent Arctic temperature amplification. Nature, 464, 1334-1337.

Screen JA, Simmonds I, Deser C, Tomas R (2013) The atmospheric response to three decades of observed Arctic sea ice loss. J. Climate, 26, 1230-1248.

Sen Gupta A, Santoso A, Taschetto AS, Ummenhofer CC, Trevena J, England MH (2009) Projected changes to the Southern Hemisphere ocean and sea ice in the IPCC AR4 climate models. J. Climate, 22, 3047–3078.

Sen Gupta A, England MH (2006) Coupled ocean–atmosphere–ice response to variations in the southern annular mode. J. Climate, 19, 4457-4486.

Sévellec F, Fedorov AV (2013) The leading, interdecadal eigenmode of the Atlantic meridional overturning circulation in a realistic ocean model. J. Climate, 26, 2160-2183.

Sévellec F, Fedorov AV (2015) Optimal excitation of AMOC decadal variability: Links to the subpolar ocean. Prog. Oceanogr., 132, 287-304.

Sévellec F, Fedorov AV, Liu W (2017) Arctic sea-ice decline weakens the Atlantic meridional overturning circulation. Nature Clim. Change, 7, 604-610.

Seviour WJ, Waugh DW, Polvani LM, Correa GJ, Garfinkel CI (2017) Robustness of the simulated tropospheric response to ozone depletion. J. Climate, 30, 2577–2585.

Shi JR, Kwon YO, Wijffels SE (2022) Two Distinct Modes of Climate Responses to the Anthropogenic Aerosol Forcing Changes. J. Clim. 35, 3445–3457.

Shi JR, Talley LD, Xie SP, Liu W, Gille ST (2020) Effects of Buoyancy and Wind Forcing on Southern Ocean Climate Change. J. Climate, 33, 10003-10020.

Shi JR, Xie SP, Talley LD (2018) Evolving relative importance of the Southern Ocean and North Atlantic in anthropogenic ocean heat uptake. J. Climate, 31, 7459–7479.

Shindell DT, Faluvegi G, Rotstayn L, Milly G (2015) Spatial patterns of radiative forcing and surface temperature response. J. Geophys. Res. 120, 5385–5403 (2015).

Sigmond M, Fyfe JC (2010) Has the ozone hole contributed to increased Antarctic sea ice extent? Geophys. Res. Lett., 37, L18 502, doi:10.1029/2010GL044301.

Sigmond M, Fyfe JC (2013) The Antarctic sea ice response to the ozone hole in climate models. J. Climate, 27, 1336–1342.

Sigmond M, Reader MC, Fyfe JC, Gillett NP (2011) Drivers of past and future Southern Ocean change: Stratospheric ozone versus greenhouse gas impacts. Geophys. Res. Lett., 38, L12 601.

Simon A, Gastineau G, Frankignoul C, Rousset C, Codron F (2021) Transient climate response to Arctic sea ice loss with two ice-constraining methods. J. Climate, 34, 3295-3310.

Smith DM, Murphy JM (2007) An objective ocean temperature and salinity analysis using covariances from a global climate model. J. Geophys. Res. Oceans 112, C02022.

Smith KL, Polvani LM, Marsh DR (2012) Mitigation of 21st century Antarctic sea ice loss by stratospheric ozone recovery. Geophys. Res. Lett., 39, L20 701, doi:10.1029/ 2012GL053325.

Smith RD, Jones P, Briegleb B, Bryan F, Danabasoglu G, Dennis J, Dukowicz J, Eden C, Fox-Kemper B, Gent P, Hecht M, Jayne S, Jochum M, Large W, Lindsay K, Maltrud M, Norton N, Peacock S, Vertenstein M, Yeager S (2010) The Parallel Ocean Program (POP) reference manual. Los Alamos National Laboratory Tech. Rep. LAUR-10-01853, LANL, 140 pp.

Sohail T, Irving DB, Zika JD, Holmes RM, Church JA (2021) Fifty year trends in global ocean heat content traced to surface heat fluxes in the sub-polar ocean. Geophys. Res. Lett. 48, e2020GL091439.

Solomon S (1990) Progress towards a quantitative understanding of Antarctic ozone depletion. Nature, 347, 347-354.

Solomon A, Polvani LM, Smith KL, Abernathey RP (2015) The impact of ozone depleting substances on the circulation, temperature, and salinity of the Southern Ocean: An attribution study with CESM1(WACCM). Geophys. Res. Lett., 42, 5547–5555.

Son SW, Gerber EP, Perlwitz J, Polvani LM, Gillett NP, Seo KH, Eyring V, Shepherd TG, Waugh D, Akiyoshi H, Austin J (2010) Impact of stratospheric ozone on Southern Hemisphere circulation change: A multimodel assessment. J. Geophys. Res.: Atmos., 115, D00M07.

Son SW, Han BR, Garfinkel CI, Kim SY, Park R, Abraham NL, Akiyoshi H, Archibald AT, Butchart N, Chipperfield MP, Dameris M (2018) Tropospheric jet response to Antarctic ozone depletion: An update with Chemistry-Climate Model Initiative (CCMI) models. Environ. Res. Lett., 13, 054024.

Stammerjohn SE, Drinkwater MR, Smith RC, Liu X (2003) Ice-atmosphere interactions during sea-ice advance and retreat in the western Antarctic Peninsula region. J. Geophys. Res., 108, 3329.

Steele M, Ermold W, Zhang J (2008) Arctic Ocean surface warming trends over the past 100 years. Geophys. Res. Lett., 35, L02614.

Stevenson DS, Young PJ, Naik V, Lamarque JF, Shindell DT, Voulgarakis A, Skeie RB, Dalsoren SB, Myhre G, Berntsen TK, Folberth GA.

Tropospheric ozone changes, radiative forcing and attribution to emissions in the Atmospheric Chemistry and Climate Model Intercomparison Project (ACCMIP) (2013) Atmos. Chem. Phys., 13, 3063-3085.

Stroeve JC, Kattsov V, Barrett A, Serreze M, Pavlova T, Holland M, Meier WN (2012) Trends in Arctic sea ice extent from CMIP5, CMIP3 and observations. Geophys. Res. Lett., 39, L16502.

Stuecker MF, Bitz CM, Armour KC (2017) Conditions leading to the unprecedented low Antarctic sea ice extent during the 2016 austral spring season. Geophys. Res. Lett., 44, 9008–9019.

Sun L, Alexander M, Deser C (2018) Evolution of the global coupled climate response to Arctic sea ice loss during 1990–2090 and its contribution to climate change. J. Climate, 31, 7823-7843.

Sun S, Thompson AF (2020) Centennial Changes in the Indonesian Throughflow Connected to the Atlantic Meridional Overturning Circulation: The Ocean's Transient Conveyor Belt. Geophys. Res. Lett., 47, e2020GL090615.

Sun S, Thompson AF, Eisenman I (2020) Transient overturning compensation between Atlantic and Indo-Pacific basins. J. Phys. Oceanogr., 50, 2151-2172.

Sun S, Thompson AF, Xie SP, Long SM (2022) Indo-Pacific warming induced by a weakening of the Atlantic Meridional Overturning Circulation. J. Clim. 35, 815–832.

Swart NC, Cole JNS, Kharin VV, Lazare M, Scinocca JF, Gillett NP, Anstey J, Arora V, Christian JR, Hanna S, Jiao Y, Lee WG, Majaess F, Saenko OA, Seiler C, Seinen C, Shao A, Sigmond M, Solheim L, von Salzen K, Yang D, Winter B (2019) The Canadian Earth System Model version 5 (CanESM5.0.3). Geosci. Model Dev., 12, 4823–4873.

Swart NC, Fyfe JC (2012) Observed and simulated changes in the Southern Hemisphere surface westerly wind-stress. Geophys. Res. Lett., 39, L16 711, doi:10.1029/2012GL052810.

Swart NC, Gille ST, Fyfe JC, Gillett NP (2018) Recent Southern Ocean warming and freshening driven by greenhouse gas emissions and ozone depletion. Nat. Geosci., 11, 836–841.

Talley L (2013) Closure of the global overturning circulation through the Indian, Pacific, and Southern Oceans: Schematics and transports. Oceanography 26, 80–97.

Thompson DWJ, Solomon S (2002) Interpretation of recent Southern Hemisphere climate change. Science, 296, 895–899.

Turner J, Hosking JS, Bracegirdle TJ, Marshall GJ, Phillips T (2015) Recent changes in Antarctic sea ice. Philos. Trans. R. Soc., 373, 20140163.

Turner J, Phillips T, Marshall GJ, Hosking JS, Pope JO, Bracegirdle TJ, Deb P (2017) Unprecedented springtime retreat of Antarctic sea ice in 2016. Geophys. Res. Lett., 44, 6868–6875.

Vihma T (2014) Effects of Arctic sea ice decline on weather and climate: A review. Surv. Geophys., 35, 1175-1214.

Von Schuckmann K, Palmer MD, Trenberth KE, Cazenave A, Chambers D, Champollion N, Hansen J, Josey SA, Loeb N, Mathieu PP, Meyssignac B (2016) An imperative to monitor Earth's energy imbalance. Nat. Clim. Change 6, 138–144.

Wang H, Xie SP, Zheng XT, Kosaka Y, Xu Y, Geng YF (2020) Dynamics of Southern Hemisphere atmospheric circulation response to anthropogenic aerosol forcing. Geophys. Res. Lett. 47, e2020GL089919.

Wang L, Lyu K, Zhuang W, Zhang W, Makarim S, Yan XH (2021) Recent Shift in the Warming of the Southern Oceans Modulated by Decadal Climate Variability. Geophys. Res. Lett., 48, e2020GL090889.

Waugh DW, Primeau F, DeVries T, Holzer M (2013) Recent changes in the ventilation of the southern oceans. Science, 339, 568–570.

Waugh DW, McC. Hogg A, Spence P, England MH, Haine TW (2019) Response of Southern Ocean ventilation to changes in midlatitude westerly winds. J. Climate, 32, 5345-5361.

Weldeab S, Friedrich T, Timmermann A, Schneider RR (2016) Strong middepth warming and weak radiocarbon imprints in the equatorial Atlantic during Heinrich 1 and Younger Dryas. Paleoceanography, 31, 1070-1082.

Winton M, Griffies SM, Samuels BL, Sarmiento JL, Frölicher TL (2013) Connecting changing ocean circulation with changing climate. J. Climate, 26, 2268–2278.

Winton M, Takahashi K, Held IM (2010) Importance of ocean heat uptake efficacy to transient climate change. J. Climate, 23, 2333–2344.

Wyser K, van Noije T, Yang S, von Hardenberg J, O'Donnell D, Döscher R (2020) On the increased climate sensitivity in the EC-Earth model from CMIP5 to CMIP6. Geosci. Model Dev. 13, 3465–3474.

Xie P, Vallis GK (2012) The passive and active nature of ocean heat uptake in idealized climate change experiments. Clim. Dyn., 38, 667–684.

Yang H, Zhao Y, Liu Z, Li Q, He F, Zhang Q (2015a) Heat Transport Compensation in Atmosphere and Ocean over the Past 22,000 Years. Sci. Rep., 5, 16661.

Yang H, Li Q, Wang K, Sun Y, Sun D (2015b) Decomposing the meridional heat transport in the climate system. Clim. Dyn., 44, 2751–2768.

Yeung LY, Murray LT, Martinerie P, Witrant E, Hu H, Banerjee A, Orsi A, Chappellaz J (2019) Isotopic constraint on the twentieth-century increase in tropospheric ozone. Nature, 570, 224-227.

Young PJ, Naik V, Fiore AM, Gaudel A, Guo J, Lin MY, Neu JL, Parrish DD, Rieder HE, Schnell JL, Tilmes S, Wild O, Zhang L, Ziemke J, Brandt J, Delcloo A, Doherty RM, Geels C, Hegglin MI, Hu L, Im U, Kumar R, Luhar A, Murray L, Plummer D, Rodriguez J, Saiz-Lopez A, Schultz MG, Woodhouse MT, Zeng, G (2018) Tropospheric Ozone Assessment Report: Assessment of global-scale model performance for global and regional ozone distributions, variability, and trends. Elementa: Sci. Anthrop., 6, 10.

Zelinka MD, Myers TA, McCoy DT, Po-Chedley S, Caldwell PM, Ceppi P, Klein SA, Taylor KE (2020) Causes of higher climate sensitivity in CMIP6 models. Geophys. Res. Lett. 47, e2019GL085782.

Zhang J, Furtado K, Turnock ST, Mulcahy JP, Wilcox LJ, Booth BB, Sexton D, Wu T, Zhang F, Liu Q (2021) The role of anthropogenic aerosols in the anomalous cooling from 1960 to 1990 in the CMIP6 Earth system models. Atmos. Chem. Phys. 21, 18609–18627.

Zanna L, Khatiwala S, Gregory JM, Ison J, Heimbach P (2019) Global reconstruction of historical ocean heat storage and transport. Proc. Natl. Acad. Sci. U.S.A., 116, 1126–1131.

Zhang L, Cooke W (2021) Simulated changes of the Southern Ocean air-sea heat flux feedback in a warmer climate. Clim. Dyn., 22, 1-6.

Zhang L, Delworth TL, Cooke W, Yang X (2019) Natural variability of Southern Ocean convection as a driver of observed climate trends. Nat. Clim. Chang., 9, 59–65.

Zhang M, Wu Z, Qiao F, (2018) Deep Atlantic Ocean warming facilitated by the deep western boundary current and equatorial Kelvin waves. J. Climate, 31, 8541-8555.

Zhang R (2010) Latitudinal dependence of Atlantic meridional overturning circulation (AMOC) variations. Geophys. Res. Lett., 37, L16703.

Zhang R, Delworth TL (2005) Simulated tropical response to a substantial weakening of the Atlantic thermohaline circulation. J. Climate, 18, 1853-1860.

Zhang W, Yan XH (2017) The subpolar North Atlantic ocean heat content variability and its decomposition. Sci. Rep., 7, 13 748.

Zhang Y, Cooper OR, Gaudel A, Thompson AM, Nédélec P, Ogino SY, West JJ (2016) Tropospheric ozone change from 1980 to 2010 dominated by equatorward redistribution of emissions. Nat. Geosci., 9, 875-879.

Appendix A

Appendix to The effects of historical ozone changes on Southern Ocean heat uptake and storage

Appendix A Figures

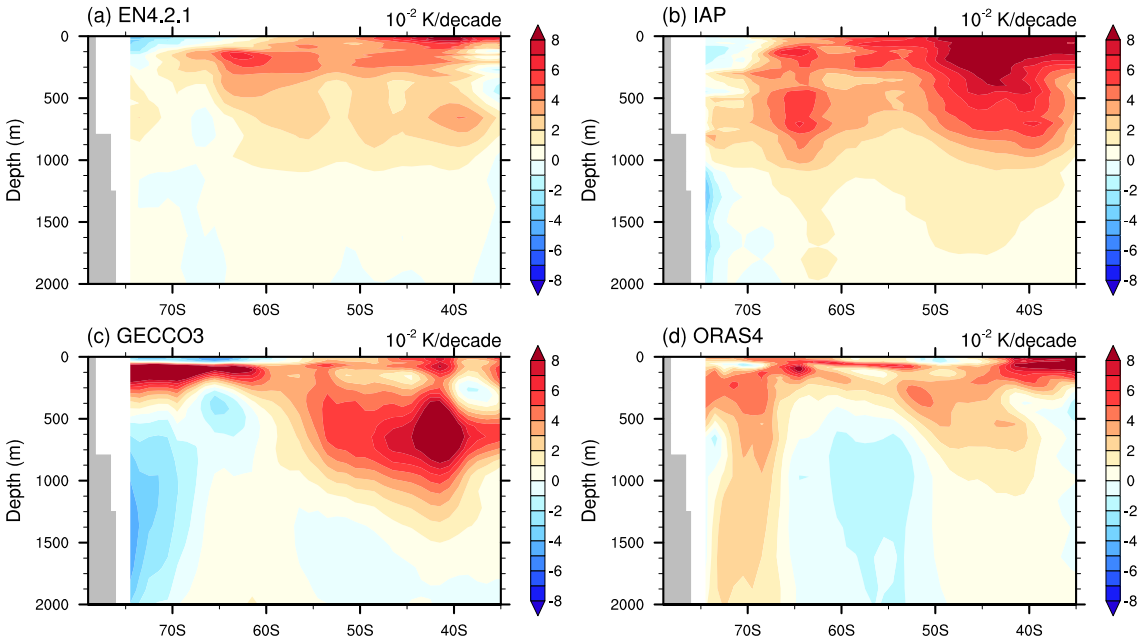

Figure A1: Annual and zonal mean historical temperature trends (shading in 10^{-2} K/decade) over the Southern Ocean during 1958-2005 from (a) EN4.2.1, (b) IAP, (c) GECCO3 and (d) ORAS4 datasets.

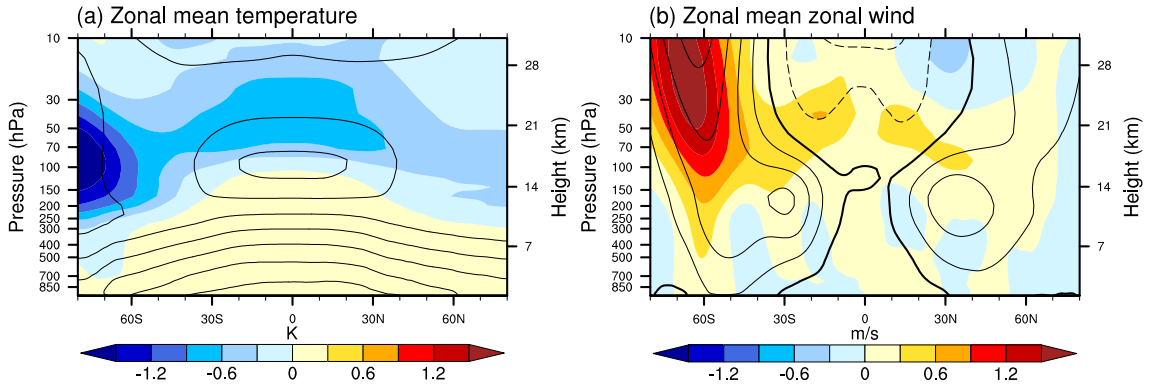

Figure A2: Changes in annual and zonal mean (a) atmospheric temperature (shading in K) and (b) zonal winds (shading in m/s) due to atmospheric ozone change during 1958-2005 in CESM1-CAM5-BGC. Annual and zonal mean climatological atmospheric temperature and zonal winds of HIST_fixedO_3 ensemble mean during 1958-2005 are superposed on panels (a) and (b), respectively. The contour interval is 15 K for climatological atmospheric temperature and 10 m/s for climatological zonal winds with zero contours thickened and solid (dashed) contours indicating positive (negative) values.

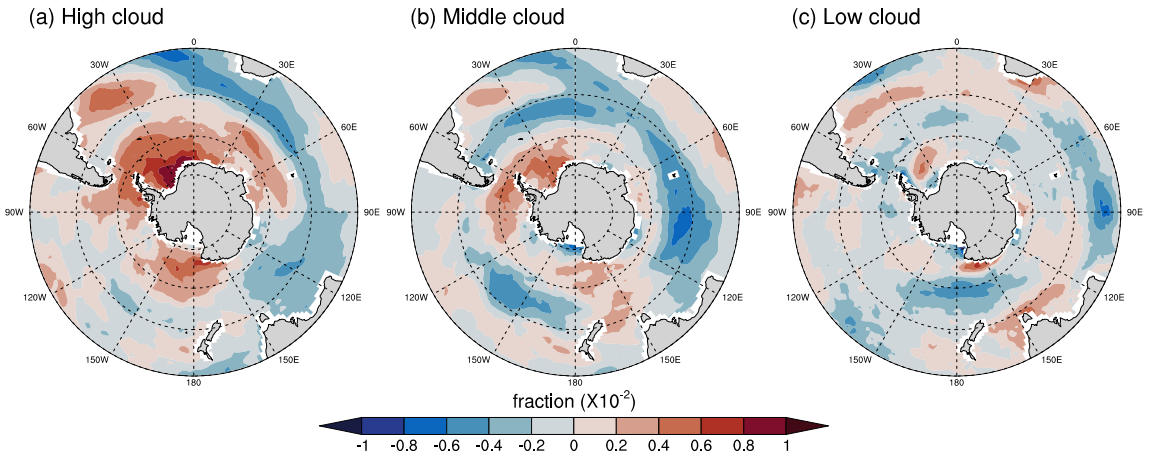

Figure A3: Changes in annual mean (a) total cloud, (b) high cloud (c) middle cloud and (d) low cloud fraction over ocean/sea ice due to atmospheric ozone change during 1958-2005 in CESM1-CAM5-BGC.

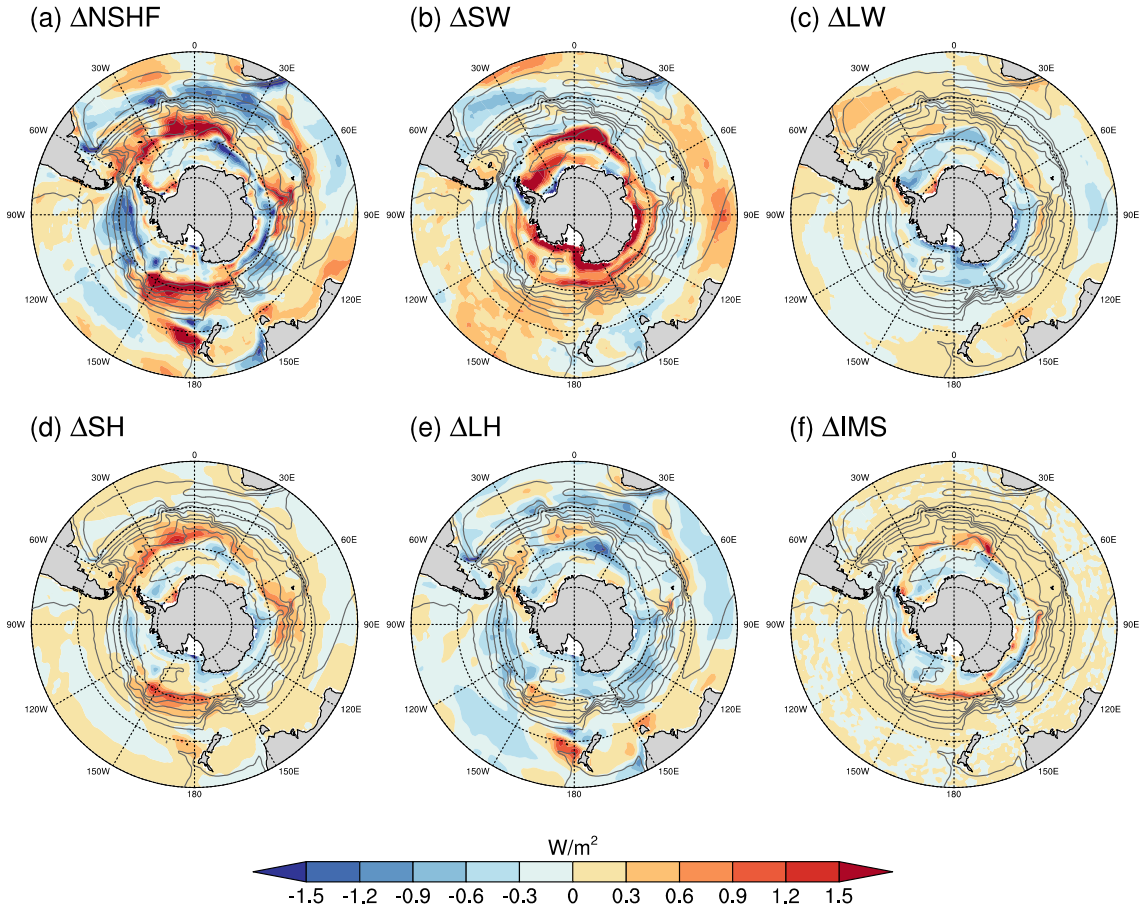

Figure A4: Changes in annual mean (a) net surface heat flux (NSHF), (b) shortwave (SW) and (c) longwave (LW) radiation fluxes, (d) sensible (SH) and (e) latent (LH) heat fluxes and (f) the flux due to snow/sea ice formation and melt (IMS) over ocean due to atmospheric ozone change during 1958-2005 in CESM1-CAM5-BGC. The averaged path of the ACC over 1958-2005 is superposed in (a) that is represented by the contours of annual mean barotropic stream function from the 1958-2005 averages of the ensemble means HIST_fixedO_3 (gray).

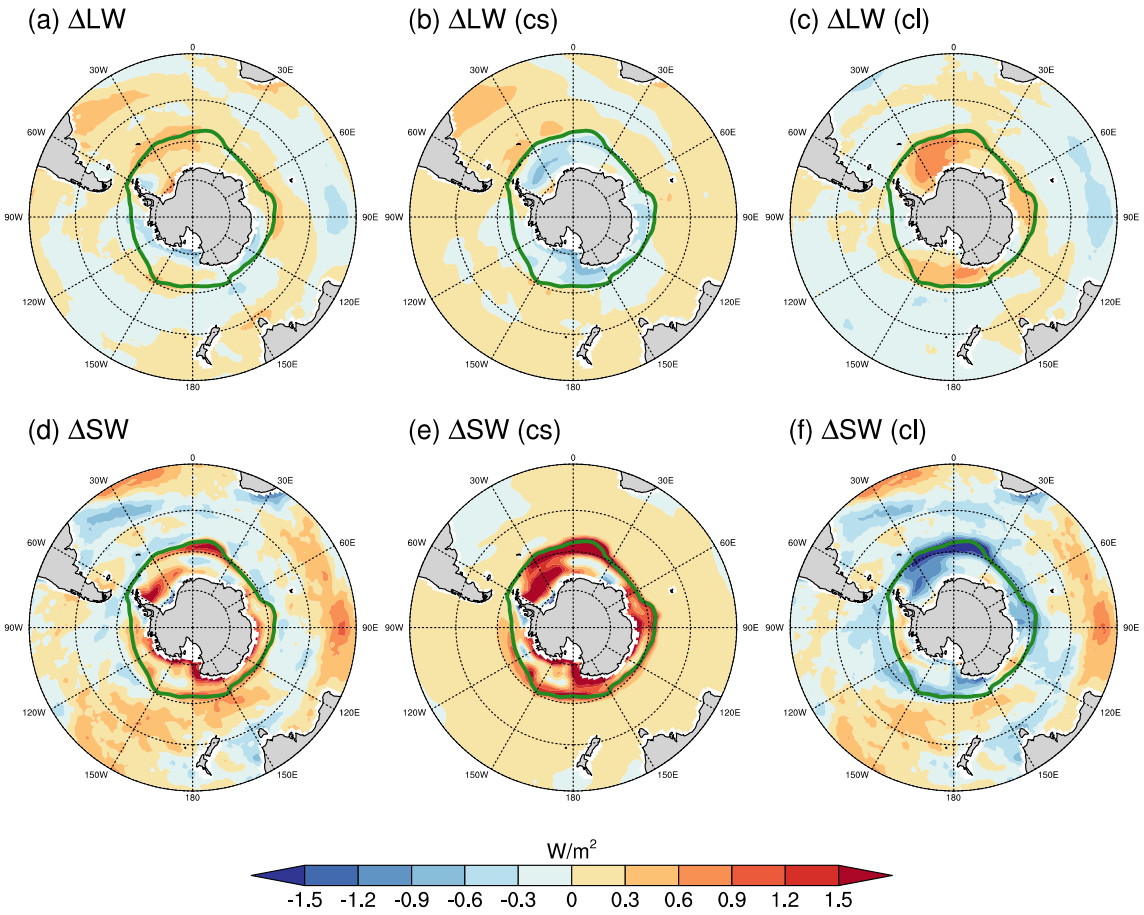

Figure A5: Changes in annual mean (a) downward longwave (LW) and (d) shortwave (SW), (b) downward longwave [LW (cs)] and (e) shortwave [SW (cs)] with clear sky, and (c) downward longwave [LW (cl)] and (f) shortwave [SW (cl)] due to cloud effects over ocean/sea ice in response to atmospheric ozone change during 1958-2005 in CESM1-CAM5-BGC. Annual mean climatological sea ice edges (green) that are based on 15% sea ice fraction from HIST_fixedO_3 ensemble mean during 1958-2005 are superposed in each panel.

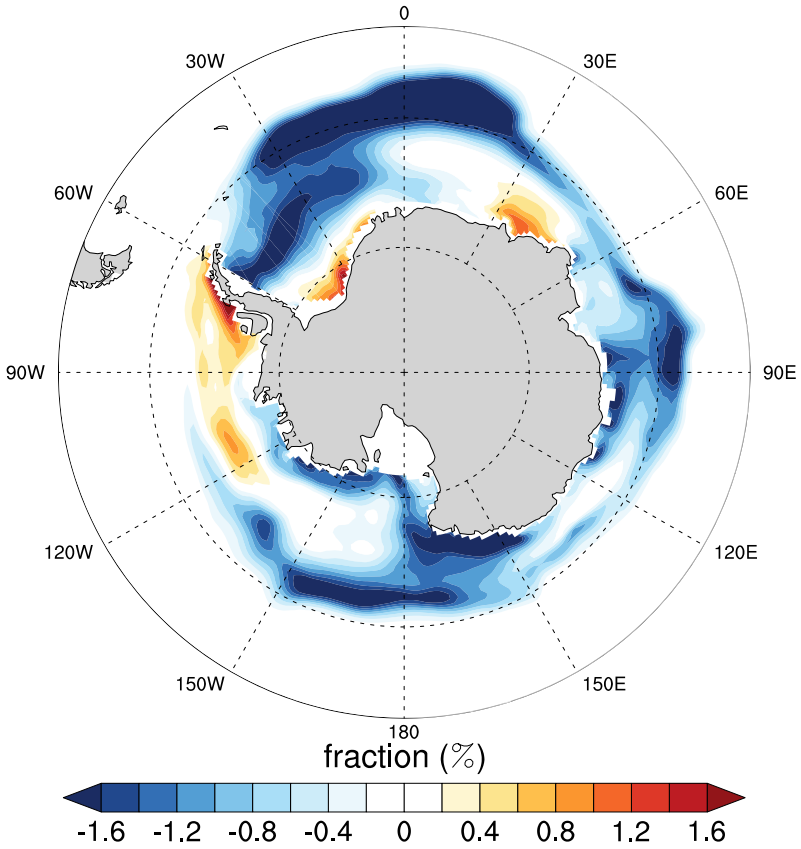

Figure A6: Changes in annual mean sea ice concentration due to atmospheric ozone change during 1958-2005 in CESM1-CAM5-BGC.

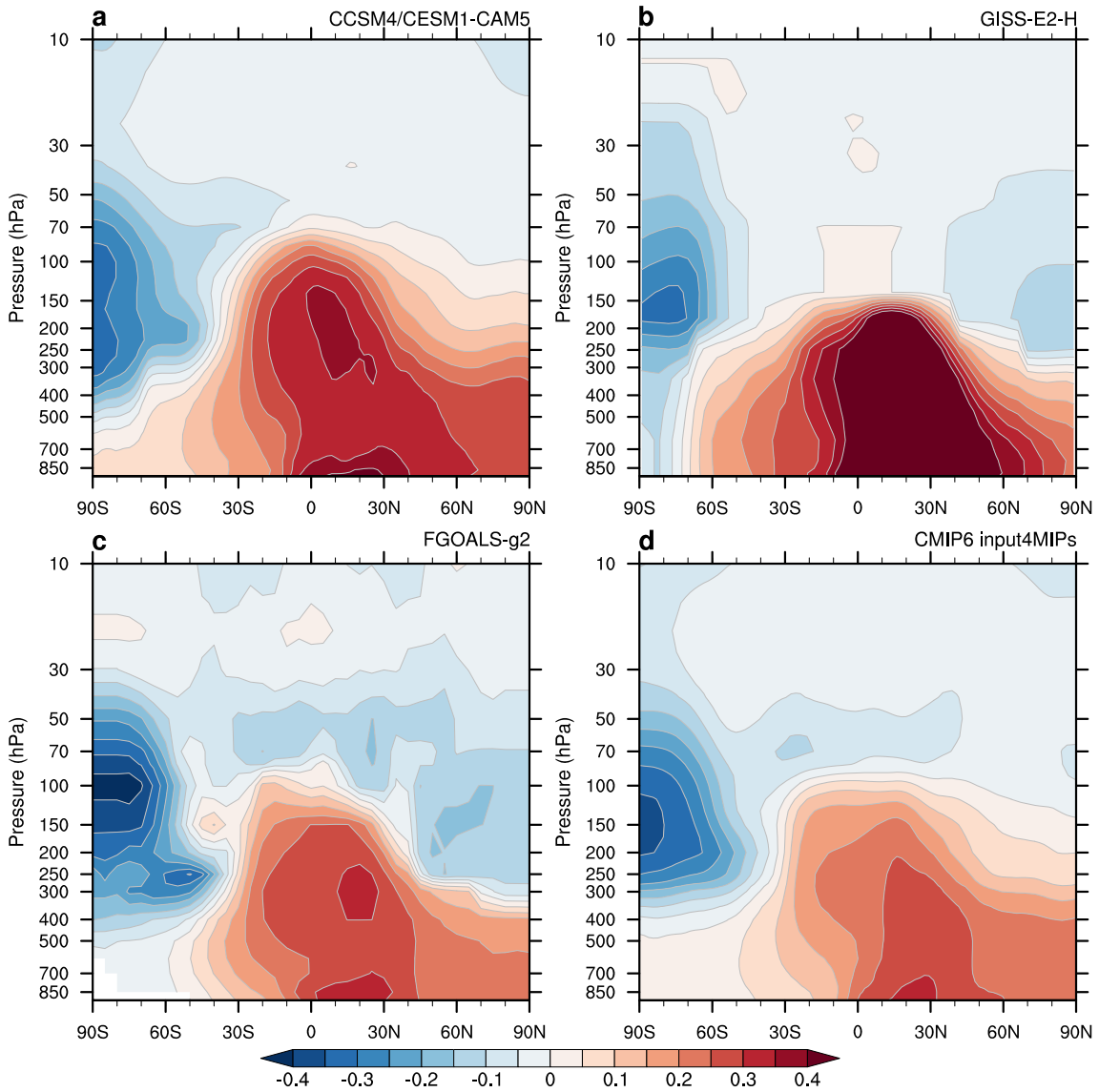

Figure A7: Prescribed ozone changes in CMIP5 and CMIP6 models. Annual and zonal mean fractional change in ozone forcing (shading in fraction) between 1995-1999 and 1955-1959 (relative to 1955-1959) in the CMIP512,45 and most CMIP632 models (including CanESM5) used in the current study, i.e., [O3(1995-1999) – O3(1955-1959)]/O3(1955-1959), in (a) CCSM4 and CESM1-CAM5, (b) GISS-E2-H, (c) FGOALS-g2 and (d) CMIP6 input4MIPs31 (https://doi.org/10.22033/ESGF/input4MIPs.1115).

Appendix B

Appendix to Anthropogenic aerosol and greenhouse gas driven ocean heat uptake and redistribution

Appendix B Figures

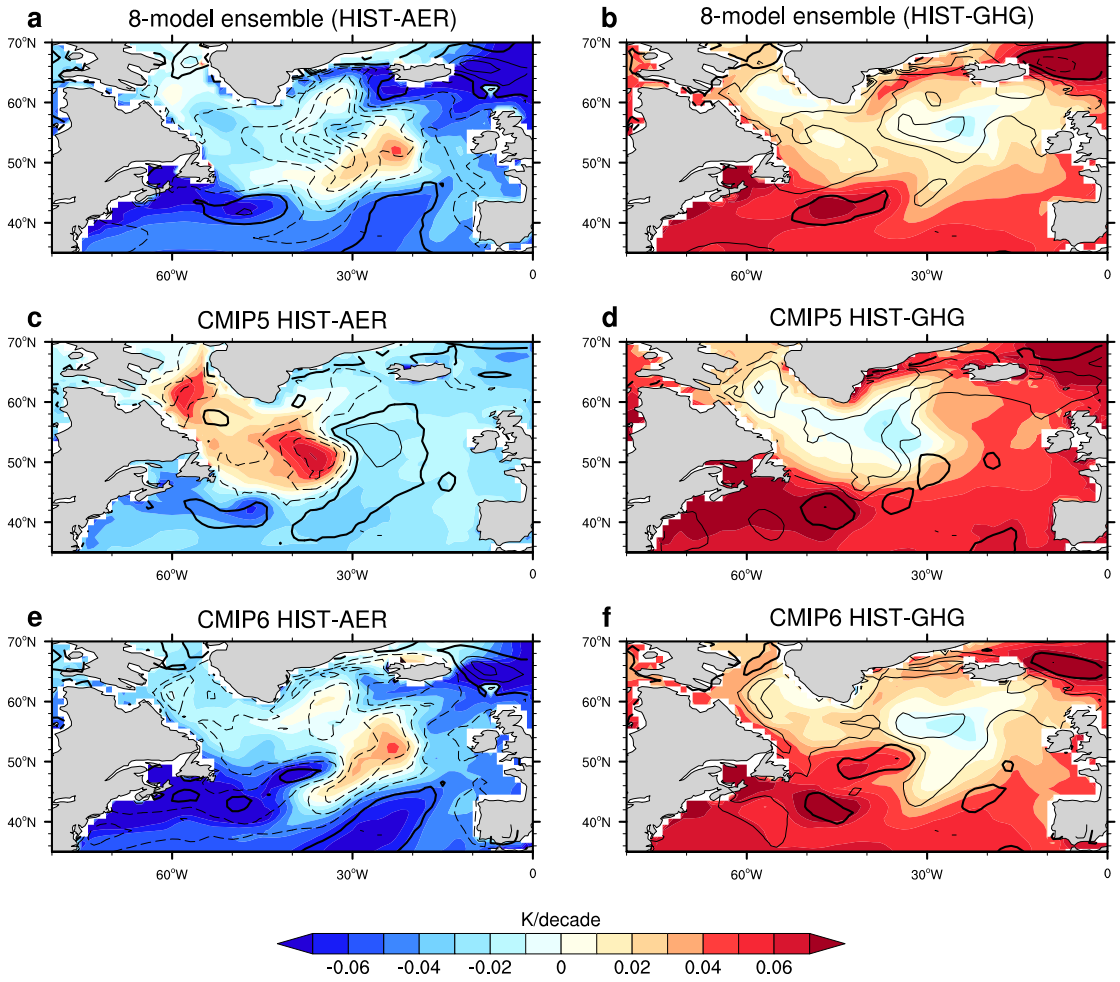

Figure B1: Anthropogenic aerosol and greenhouse gas driven changes in North Atlantic SST trend and net surface heat flux. (a,c,e) Changes (relative to the preindustrial time) in annual mean SST trend (color shading in K/decade) and net surface heat flux (contour in W/m2, with contour interval of 3 W/m2, zero contours thickened, positive solid and negative dashed, positive downward) in the North Atlantic during 1861-2005 for the multi-model means of the HIST-AER simulation with (a) the 8-model ensemble, (c) 10 CMIP5 models and (e) 10 CMIP6 models. (b,d,f) As in (a,c,e) but for the multi-model means of the HIST-GHG simulation.

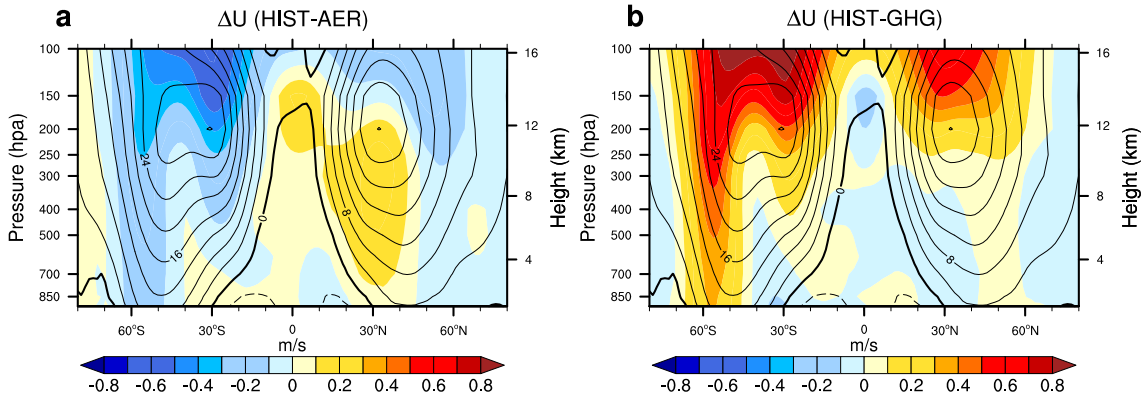

Figure B2: Anthropogenic aerosol and greenhouse gas driven zonal wind changes. Changes (relative to the preindustrial time) in annually and zonally averaged zonal winds (color shading in m/s) during 1861-2005 for the multi-model means of the (a) HIST-AER and (b) HIST-GHG simulations for the 8-model ensemble. The multi-model mean preindustrial climatology of annually and zonally averaged zonal winds (contours with an interval of 4 m/s, zero contours thickened, solid positive and dashed negative) is superposed on either panel.

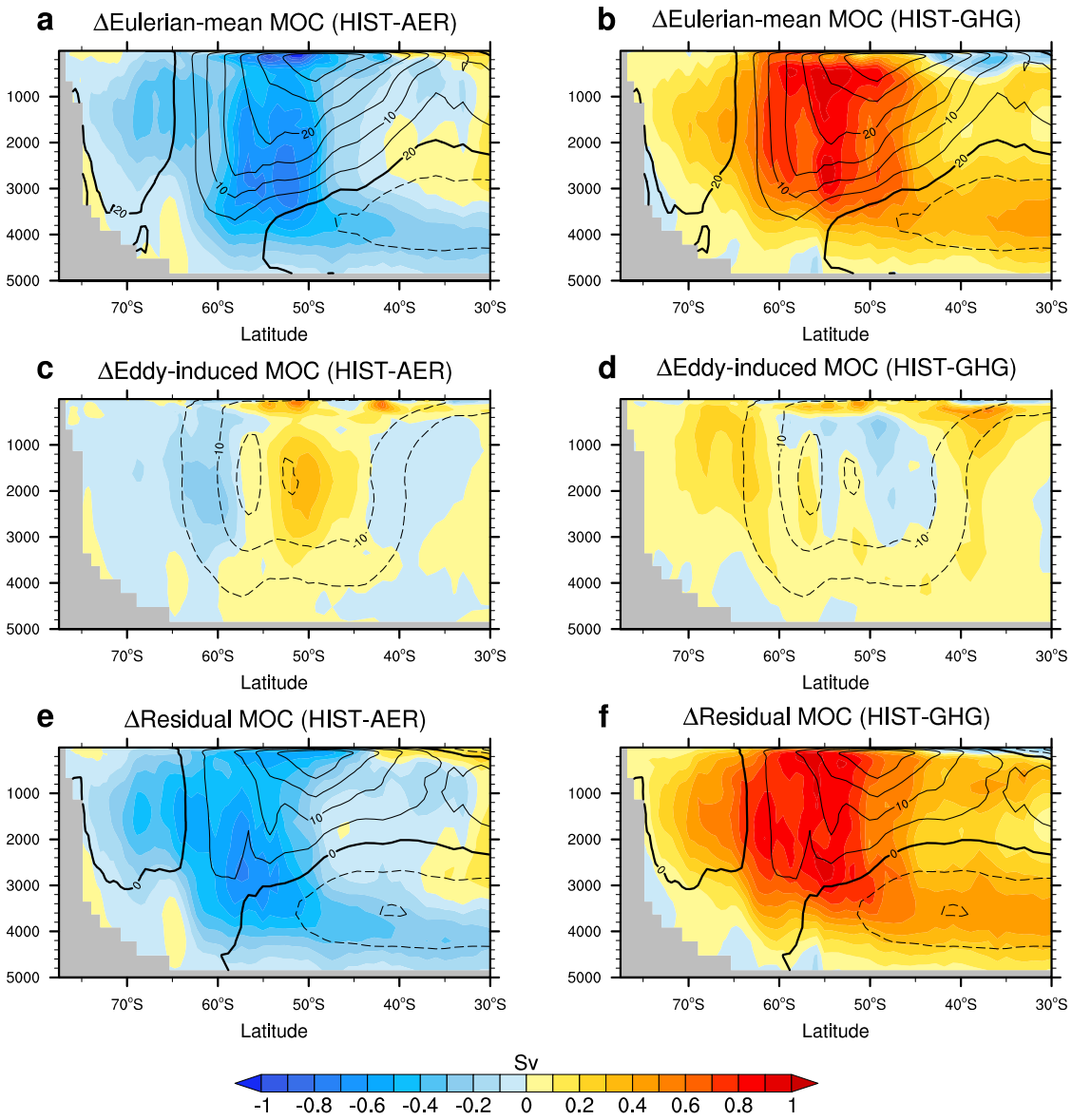

Figure B3: Anthropogenic aerosol and greenhouse gas driven Southern Ocean MOC changes. Changes (relative to the preindustrial time) in annual mean (a) Eulerian-mean, (c) eddy-induced and (e) residual MOCs (color shading in Sv, 1Sv = 10^6 m^3/s) in the Southern Ocean during 1861-2005 for the multi-model mean of the HIST-AER simulation with CESM1-CN, GISS-E2-1-G, HadGEM3-GC31-LL and NorESM2-LM, since the variable of eddy-induced MOC is available only in these four models within the 8-model ensemble. (b,d,f) As in (a,c,e) but for the HIST-GHG simulation. Annual mean MOC climatology from preindustrial control run in each ocean basin is shown in each panel (contours in Sv, with a contour interval of 5 Sv, zero contours thickened, solid positive and dashed negative).

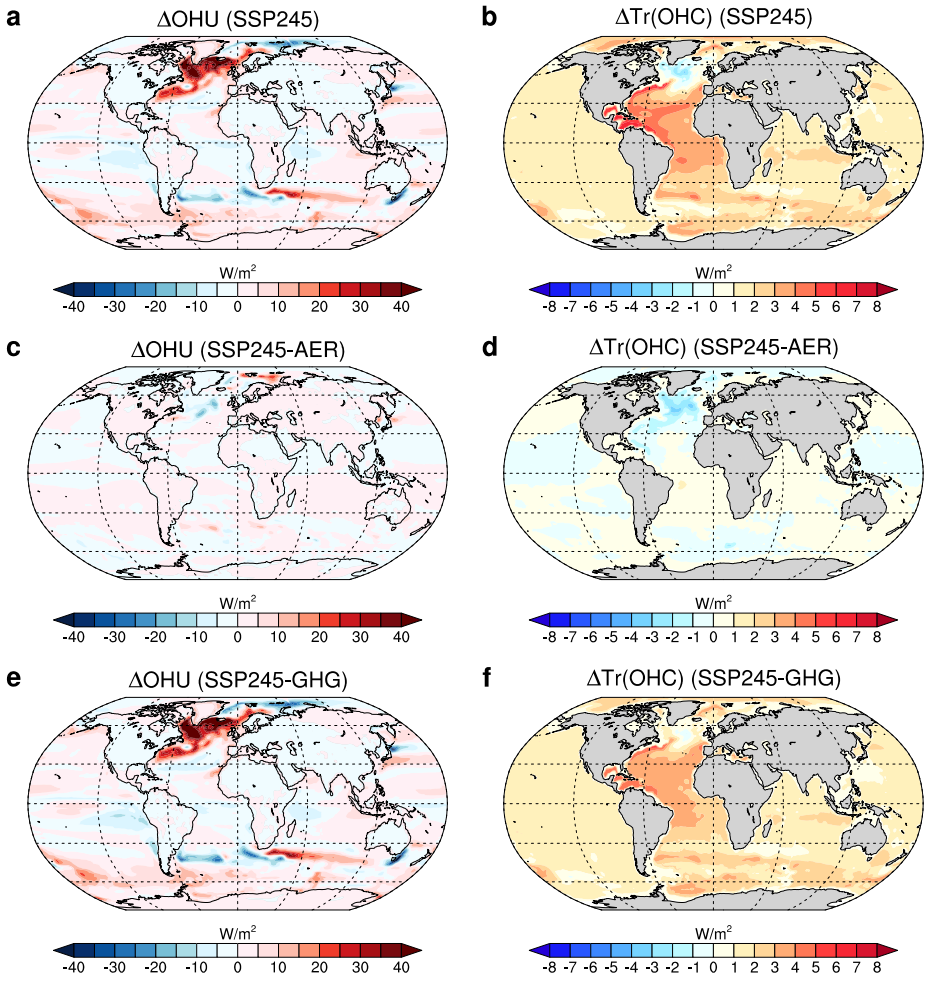

Figure B4: Future aerosol and greenhouse gas driven OHU and OHC trend changes. (a,c,e) Annual mean changes (relative to the preindustrial time) in global OHU during 2021-2100 (color shading in W/m²) for the multi-model mean of the 4-model ensemble (a) SSP245, (c) SSP245-AER and (e) SSP245-GHG simulations. (b,d,f) As in (a,c,e) for the changes in the full-depth integrated annual mean OHC trend during 2021-2100.

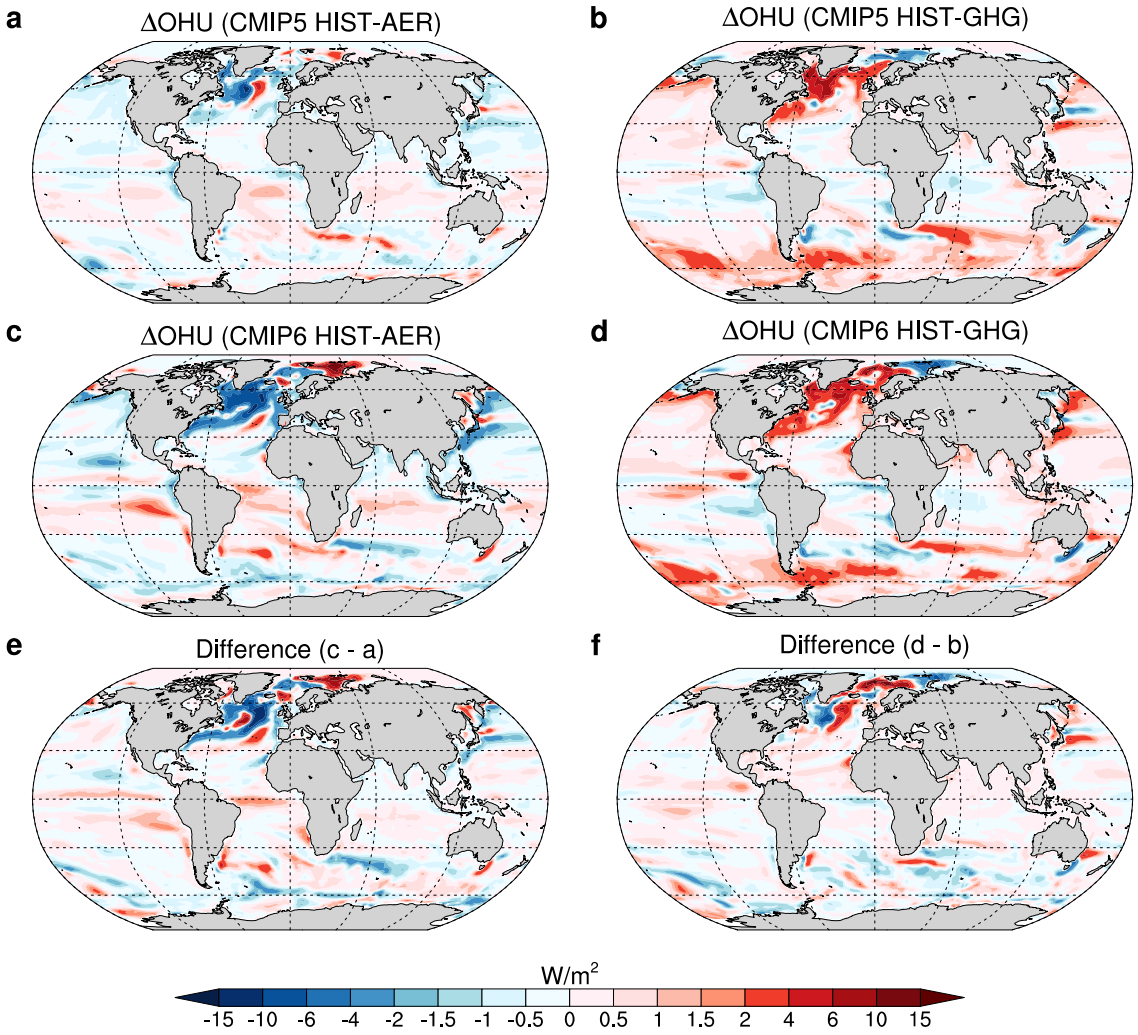

Figure B5: Aerosol and greenhouse gas driven OHU changes in CMIP5 and CMIP6 models. (a,c,e) Changes (relative to the preindustrial time) in annual mean global OHU during 1861-2005 (color shading in W/m^2) for the multi-model means of the HIST-AER simulation with (a) 10 CMIP5 models and (c) 10 CMIP6 models as well as (e) the difference between the two (c-a). (b,d,f) As in (a,c,e) but for the HIST-GHG simulation.

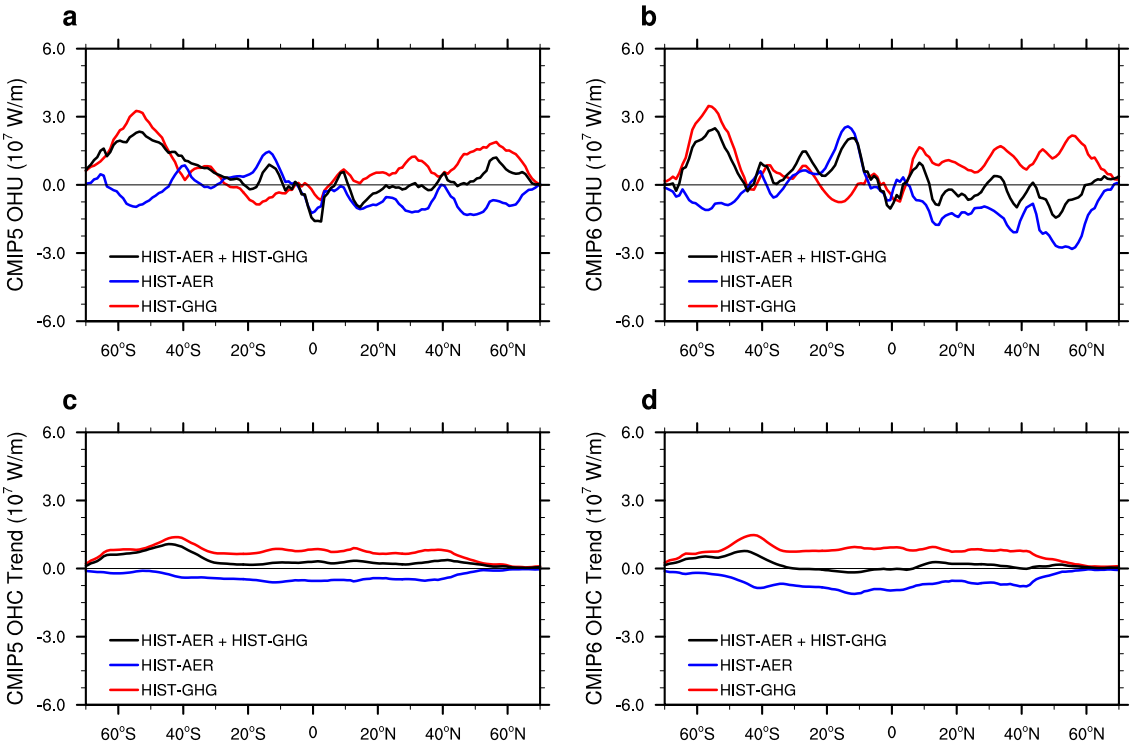

Figure B6: Zonal mean aerosol and greenhouse gas driven OHU and OHC trend changes in CMIP5 and CMIP6 models. (a,b) Changes (relative to the preindustrial time) in annual mean zonally integrated OHU during 1861-2005 in the HIST-AER simulation (multi-model mean, blue) and HIST-GHG simulation (multi-model mean, red) and the sum of both changes (multi-model mean, black) with (a) 10 CMIP5 models and (b) 10 CMIP6 models. (c,d) As in (a,b) but for changes in annual mean zonally integrated full-depth OHC trend.

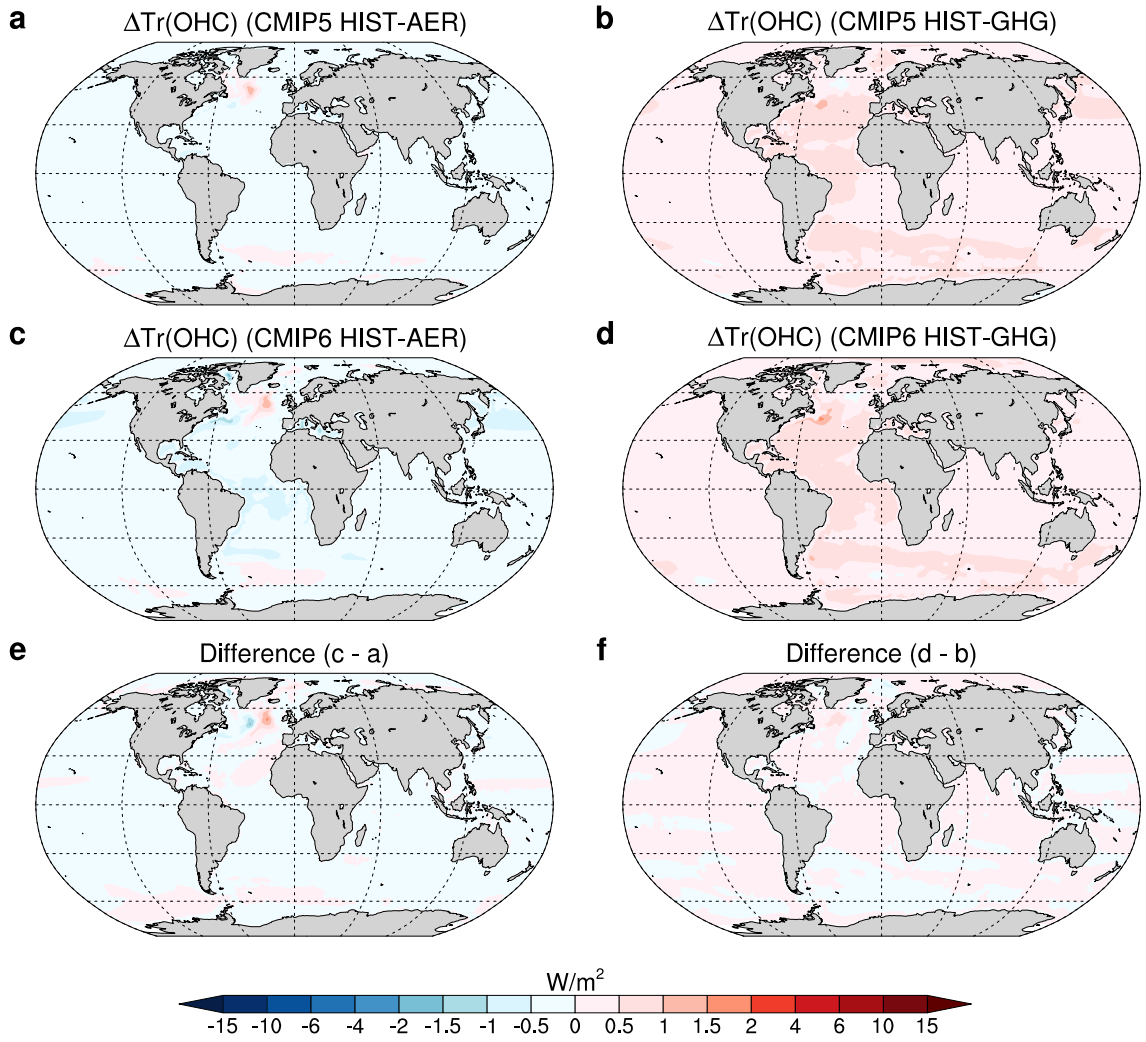

Figure B7: Aerosol and greenhouse gas driven OHC trend changes in CMIP5 and CMIP6 models. As in Figure B5 but for changes in the trend of annual mean full-depth integrated OHC during 1861-2005.

Appendix B Tables

Table B1: Climate models and their preindustrial and historical single and all forcing simulations. The 10 CMIP5 models and 10 CMIP6 models together with their preindustrial and historical single and all forcing simulations and ensemble(s) used in the current study (Methods). Models with * are used to construct the 8-model ensemble.

Model	CMIP 5/CMIP6	pi-Control	HIST-AER	HIST-GHG	HIST
CanESM2	CMIP 5	r1i1p1	r(1-5)i1p4	r(1-5)i1p1	r(1-5)i1p1
CCSM4	CMIP 5	r1i1p1	r(1,4)i1p10	r(1,4,6)i1p1	r(1-6)i1p1
CESM1-CN*	CMIP 5	r1i1p1	r(1-3)i1p1	r(1-3)i1p1	r(1-3)i1p1
CSIRO-Mk3-6-0*	CMIP 5	r1i1p1	r(1-10)i1p4	r(1-10)i1p1	r(1-10)i1p1
FGOALS-g2	CMIP 5	r1i1p1	r2i1p1	r1i1p1	r(1-5)i1p1
GFDL-CM3	CMIP 5	r1i1p1	r(1,5)i1p1	r(1,3,5)i1p1	r(1,3,5)i1p1
GFDL-ESM2M	CMIP 5	r1i1p1	r1i1p5	r1i1p1	r1i1p1
GISS-E2-H	CMIP 5	r1i1p1	r(1-5)i1p107	r(1-5)i1p1	r(1-5)i1p1
GISS-E2-R	CMIP 5	r1i1p1	r(1-5)i1p107	r(1-5)i1p1	r(1-6)i1p1
IPSL-CM5A-LR	CMIP 5	r1i1p1	r1i1p3	r(1-3)1i1p1	r(1-5)1i1p1
ACCESS-ESM1-5	CMIP 6	r1i1p1f1	r(1-3)i1p1f1	r(1-3)i1p1f1	r(1-30)i1p1f1
CanESM5*	CMIP 6	r1i1p1f1	r(1-10)i1p1f1	r(1-10)i1p1f1	r(1-10)i1p1f1

CESM2	CMIP 6	r1i1p 1f1	r(1,3)i1p1f1	r(1-3)i1p1f1	r(1-11)i1p1f1
CNRM-CM6-1*	CMIP 6	r1i1p 1f2	r(1-3)i1p1f2	r(1-3)i1p1f2	r(1-30)i1p1f2
FGOALS-g3	CMIP 6	r1i1p 1f1	r(1-3)i1p1f1	r(1-3)i1p1f1	r(1-5)i1p1f1
GISS-E2-1-G*	CMIP 6	r1i1p 1f2	r(1-5)i1p1f2	r(1-5)i1p1f2	r(1-10)i1p1f2
HadGEM3-GC31-LL*	CMIP 6	r1i1p 1f3	r(1-4)i1p1f3	r(1-4)i1p1f3	r(1-4)i1p1f3
IPSL-CM6A-LR*	CMIP 6	r1i1p 1f1	r(1-10)i1p1f1	r(1-10)i1p1f1	r(1-10)i1p1f1
MIROC6	CMIP 6	r1i1p 1f1	r(1-10)i1p1f1	r(1-10)i1p1f1	r(1-10)i1p1f1
NorESM2-LM*	CMIP 6	r1i1p 1f1	r(1-3)i1p1f1	r(1-3)i1p1f1	r(1-3)i1p1f1

Table B2: Climate models and their SSP245 single and all forcing simulations. The four CMIP6 models and their SSP245 single and all forcing simulations and ensemble(s) used in the current study. For CanESM5 SSP245 simulation, there are 25 ensembles with net surface heat flux and meridional overturning circulation data available in the CMIP6 archive but only 10 ensembles r(1-10)i1p1f1 with ocean temperature data available for the calculation of ocean heat content. So only ensembles r(1-10)i1p1f1 are used.

Model	SSP245-AER	SSP245-GHG	SSP245
CanESM5	r(1-10)i1p1f1	r(1-10)i1p1f1	r(1-10)i1p1f1
GISS-E2-1-G	r(1-10)i1p1f2	r(1-5)i1p1f2	r(1-5)i1p1f2
MIROC6	r(1-10)1i1p1f1	r(1-10)1i1p1f1	r(1-50)i1p1f1
NorESM2-LM	r1i1p1f1	r1i1p1f1	r(1-3)i1p1f1

Appendix C

Appendix to Impacts of Arctic sea ice loss on global ocean circulations and interbasin ocean heat exchanges

Appendix C Figures

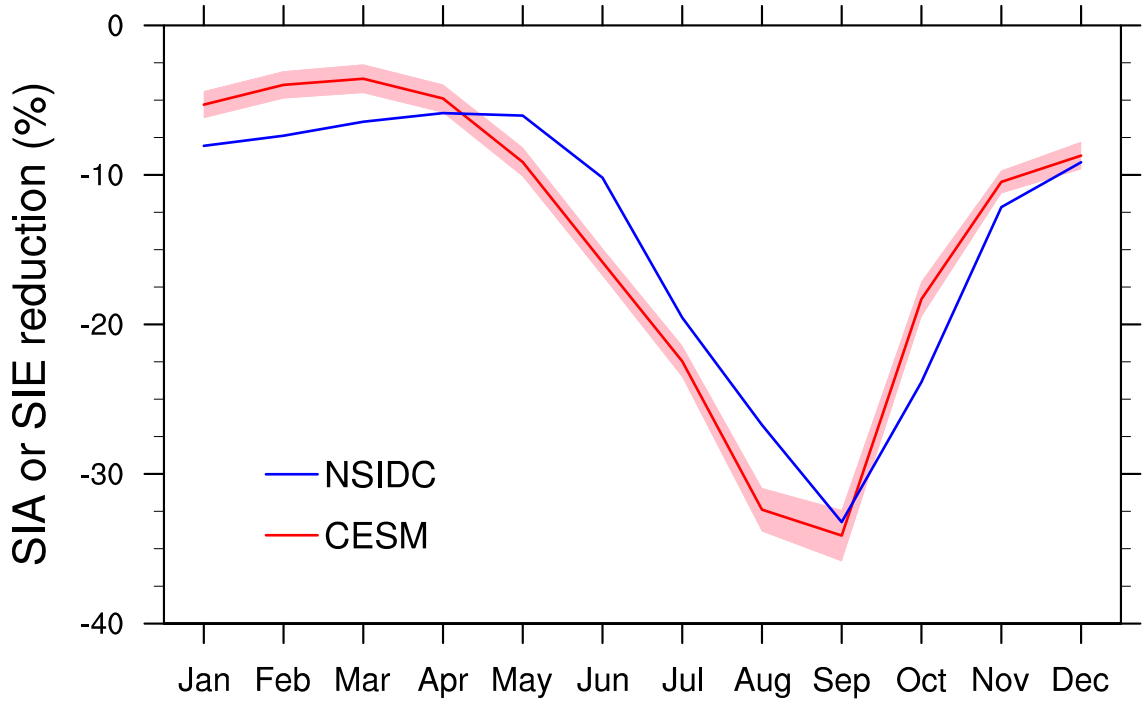

Figure C1: Changes in the Arctic sea ice area (SIA; in percent) for different months of the year in the Arctic sea ice perturbation experiment (ensemble mean: red; ensemble spread: light red) and the sea ice extent (SIE) observations from NSIDC (blue). For the perturbation experiment, the changes are computed relative to the preindustrial control run and are estimated as the ratio between the SIA anomaly during the last 100 years of the perturbation experiment and the control SIA. For the observations, the changes are computed relative to SIE during 1980-1989 and are estimated as the ratio between the SIE anomaly during 2006-2015 and the 1980-1989 SIE.

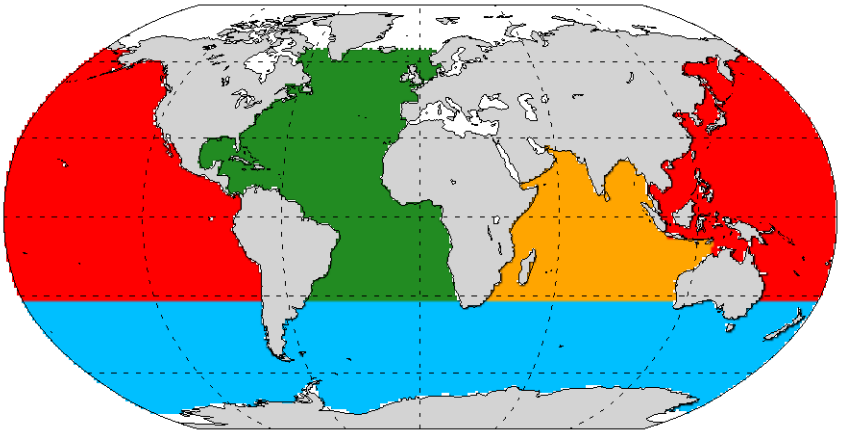

Figure C2: Ocean basins defined in the current study used for the basin integration: the Southern Ocean (blue), the Pacific (red), the Indian Ocean (orange), the Atlantic (green) and the other oceans (white). The boundary between the Southern and Atlantic/Indo-Pacific Oceans is 32°S, the boundary between the Arctic and Pacific/Atlantic Oceans is 65°N.

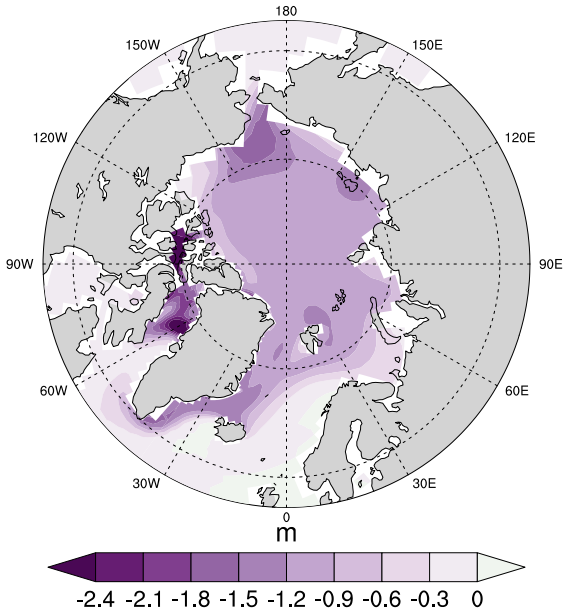

Figure C3: Changes in annual mean of Arctic sea ice thickness in the first 5 years in the Arctic sea ice perturbation simulation.

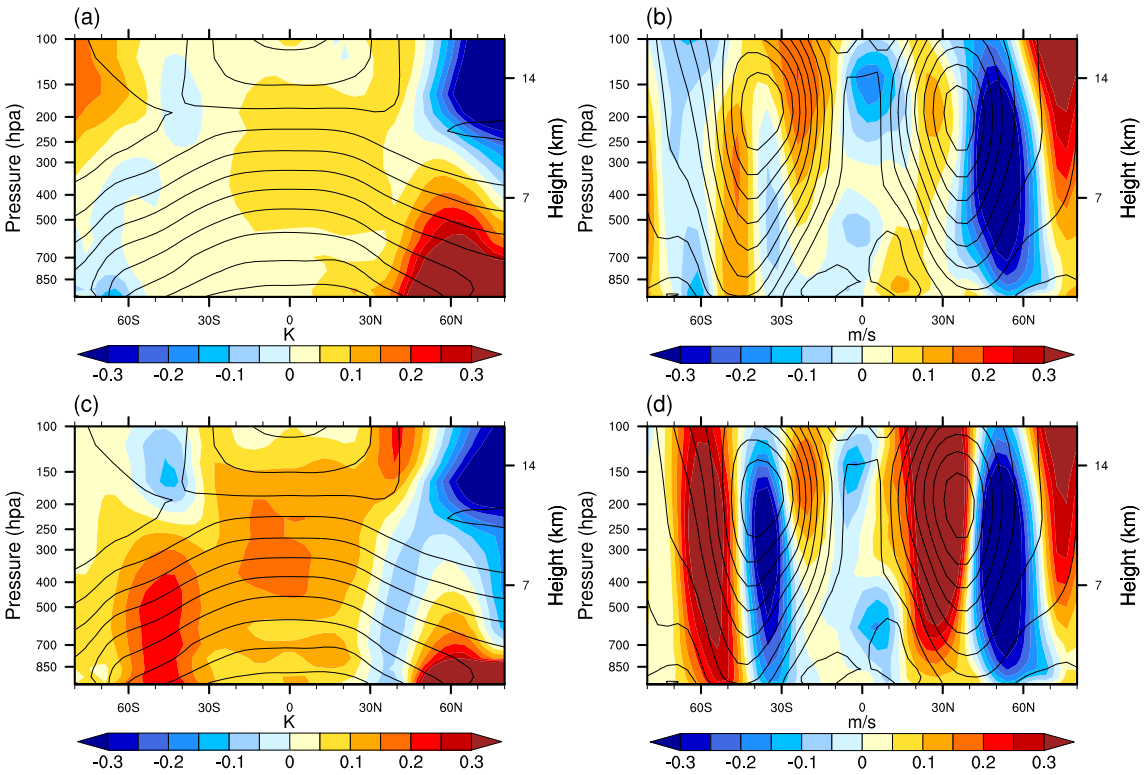

Figure C4: (left column) Arctic sea ice loss induced changes (relative to the control) in annual mean atmospheric temperature over (a) the first 10 years and (c) the later 100 years for the ensemble mean of the Arctic sea ice perturbation simulation. (right column) As in the left column but changes in zonal mean zonal winds. Annual and zonal mean climatological atmospheric temperature and zonal winds are superposed on the left (a,c) and right (b,d) two panels, respectively. The contour interval is 15 K for climatological atmospheric temperature and 10 m/s for climatological zonal winds with zero contours thickened and solid (dashed) contours indicating positive (negative) values.

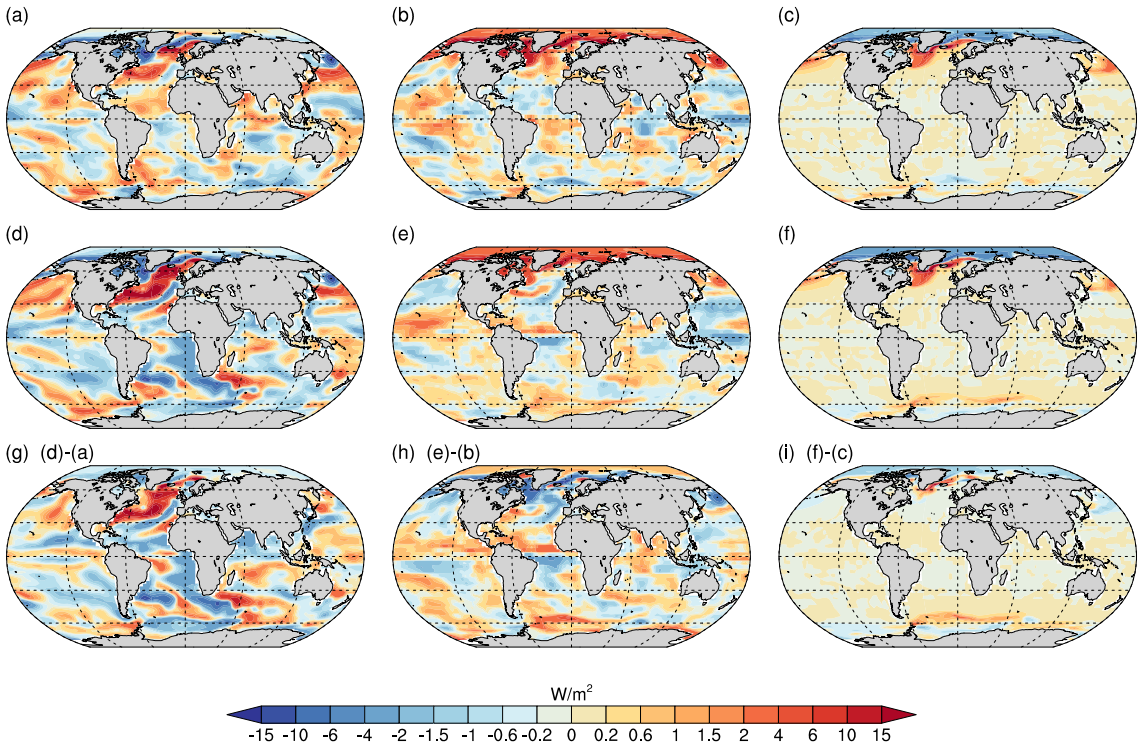

Figure C5: (left column) Arctic sea ice loss induced changes (relative to the control) in annual mean in surface turbulent heat fluxes (sensible plus latent heat fluxes) over (a) the first 10 years, (d) later 101-200 years for the ensemble mean of the Arctic sea ice perturbation simulation as well as the difference between the two given (d)-(a). (middle column) As in the left column but for changes in surface radiative energy fluxes (shortwave plus longwave radiative energy fluxes). (right column) As in the left column but for changes in the surface heat flux due to snow/sea ice formation and melt.

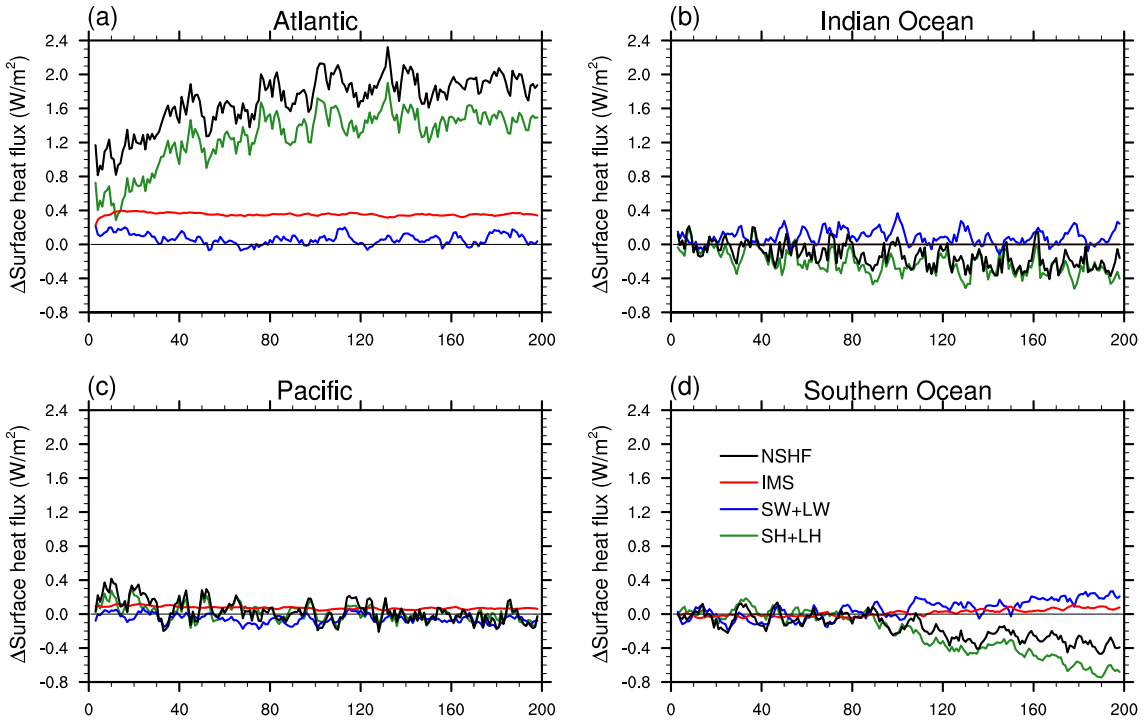

Figure C6: (a) Arctic sea ice loss induced changes (relative to the control) in annual mean area-weighted surface heat fluxes in the Atlantic: the net surface heat flux (NSHF; black), the flux due to snow/sea ice formation and melt (IMS; red), shortwave plus longwave (SW+LW; blue) energy flux and sensible plus latent heat flux (SH + LH; green) for the ensemble mean of the Arctic sea ice perturbation simulation. (b), (c) and (d) as in (a) but for changes in the Indian, Pacific and Southern Oceans, respectively.

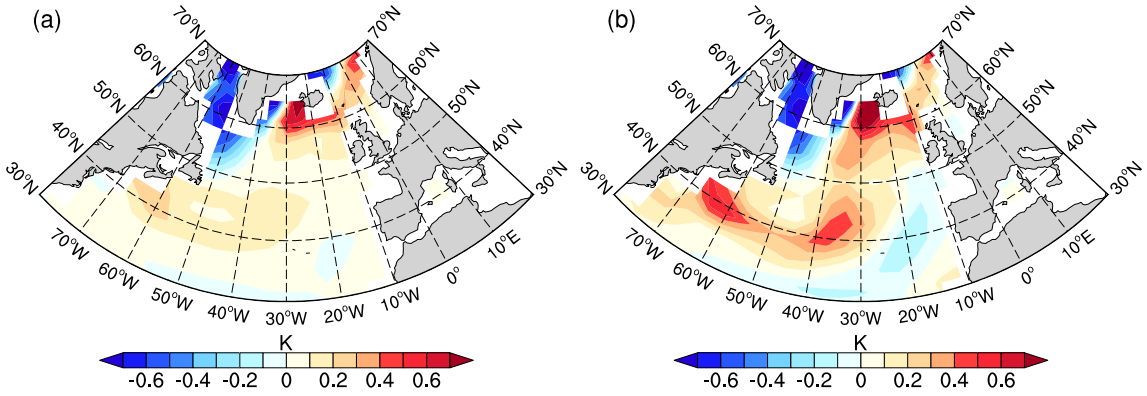

Figure C7: Arctic sea ice loss induced changes (relative to the control) in air-sea temperature contrast during the (a) first 10 years and (b) later 100 years for the ensemble mean of the Arctic sea ice perturbation simulation.